10-10-2014

A Generic Approach for the Synthesis of Nanocrystalline Mesoporous Materials by Inverse Micelle Templating

Altug Suleyman Poyraz
University of Connecticut - Storrs, altugpoyraz@gmail.com

A Generic Approach for the Synthesis of Nanocrystalline Mesoporous Materials by Inverse Micelle Templating

Altug S. Poyraz, PhD

University of Connecticut, 2014

There are 4 chapters in this thesis. Chapter 1 provides background information (synthesis, applications, and limitations) about mesoporous materials. Chapter 2 describes the developed inverse micelle method for the synthesis of mesoporous materials and illustrates the applicability of the method. Chapter 3 discusses mesoporous solid acids prepared by inverse micelle method and their catalytic activity. Chapter 4 suggests a mild transformation of mesoporous manganese oxides into various other crystal structures under mild acidic conditions.

Thermally stable, crystalline wall, thermally controlled monomodal pore size mesoporous materials are discussed in the thesis. Generation of such materials involves use of inverse micelles, elimination of solvent effects, minimization the effect of water content, and controlling the condensation of inorganic framework by NOx decomposition. Nano-size particles are formed in inverse micelles and are randomly packed to a mesoporous structure. The mesopores are created by interconnected intra-particle voids, thus can be tuned from 1.2 nm to 25 nm by controlling the nano-particle size. Such phenomena allow preparation of multiple phases of the same metal and syntheses of materials having compositions throughout much of the periodic table. The method has been demonstrated to work for numerous transition metal oxides like Ti, Zr, Hf, Nb, Ta, Cr, W, Mn, Fe, Co, Ni, Cu, Zn, Zr,; nonmetals

like Al, Si, Sn, lanthanides (La, Ce, Sm. Gd), and mixed metals (YSZ, Alumina Silicate etc). Thermal stabilities can be as high as 800^{o}C. The mesopores are monomodal in distribution and allow unique adsorptive and catalytic properties. Such materials have unique properties that will allow use in adsorption, catalysis, sensors, batteries, optoelectronics, magnetic, and other areas.

A Generic Approach for the Synthesis of Nanocrystalline Mesoporous Materials by Inverse Micelle Templating

Altug S. Poyraz

B.S., Bilkent University, Turkey, 2007

M.S., Bilkent University, Turkey, 2009

A Dissertation

Submitted in Partial Fulfillment of the

Requirements for the Degree of Doctor of Philosophy

At

The University of Connecticut

2014

APPROVAL PAGE

Doctor of Philosophy Dissertation

A Generic Approach for the Synthesis of Nanocrystalline Mesoporous Materials by Inverse Micelle Templating

Presented by

Altug S. Poyraz, M.S.

Major Advisor

_____

Steven L. Suib

Associate Advisor

_____

James F. Rusling

Associate Advisor

_____

Alfredo-Angeles Boza

Associate Advisor

_____

Edward J. Neth

Associate Advisor

_____

Alpay S. Pamir

University of Connecticut

2014

To My Mom and Dad

ACKNOWLEDGEMENTS

I would like to express my deep gratitude to my supervisor Dr. Steven L. Suib, for his guidance and support throughout my graduate studies. I hope that I could be as lively, enthusiastic, and energetic as Dr. Suib and to someday be able to command an audience as well as he can. I am also grateful to my colleagues for their intellectual contributions to my research and for their true friendships. Dr. Cecil King'ondu, Dr. Fabian Garces, Sourav Biswas, Zhu Luo, Sheng-Yu Chen, Curtis Guild, Saiful Islam, Dave Kriz, Lakshitha Pahalagedara, Dr. Saminda Dharmarathna, Wenqiao Song, and Jagadeswara Kona and of course Chung-Hao Kuo.

I especially thank my mom and dad, and brother. My hard-working parents have sacrificed their lives for my brother and myself and provided unconditional love and care. I love them so much, and I would not have made it this far without them. I know I always have my family to count on when times are rough.

Table of Contents

LIST OF FIGURES

LIST OF TABLES

Chapter 1: Introduction

1.1 Overview of Mesoporous Materials:

Twenty years after the seminal introduction of the first mesoporous materials by Mobil Company, the field of mesoporous materials has expanded enormously and almost 40,000 research articles have been published related to mesoporous materials during this period[1,2]. The effort can mainly be classified under two headings: (1) Developing novel synthetic approaches for fine tuning physicochemical properties and (2) their use in various applications. The huge interest in the field of mesoporous materials is due to the control and fine tuning of structural properties such as pore size, pore volume, bi-modal porosity (micro and meso), unique morphologies (i.e. sphere, rods, cubes), different mesostructures (i.e. 2D hexagonal, tetragonal. face centered cubic), and modifications for a wide range of specific applications. The fine tuning and control of the structural parameters has been demonstrated to be very useful in numerous fields such as gas sensors, cathode materials in solar cells and lithium ion batteries, redox supercapacitors, adsorption and separation, catalysis, and magnetic materials [3–10]. The synthesis of mesoporous materials and the fine tuning of the structural parameters are possible by controlling the soft-assembly (micellization of the surfactants), micelle-inorganic precursor interaction, and controlling the condensation of inorganic sols[11,12]. Therefore, significant numbers of studies related to mesoporous materials focus on new synthetic approaches which involve the use of surfactant micelles as soft templates [13–18]. From a thermodynamic point of view, the crucial parameters are Inorganic-Inorganic (G_{I-I}), Inorganic-Surfactant (G_{I-S}) interactions [12,19]. In order to obtain an ordered mesostructured material, controlled condensation of the inorganic component (G_{I-I}) and strong inorganic-surfactant interaction (G_{I-S}) are desired. The former is controlled by the sol-gel

chemistry of the inorganic sols by proper pH adjustment and in alcoholic solutions [20,21]. The latter (inorganic-surfactant) interaction can be Coulombic such as S^+I^-; S^-I^+; $S^+X^-I^+$; $S^-X^+I^-$ where S is the surfactant, I is the inorganic sol and X is the mediator ion or can be a charge transfer interaction between empty d orbitals of transition metal and oxygen lone pair electrons of the surfactant[8,11,14,15,18,21–24].

1.2 Mesoporous Transition Metal Oxides (MTMO)

The developed synthetic approaches have yielded the synthesis of numerous mesoporous materials from different parts of the periodic table. Among them the synthesis of mesoporous transition metal oxides (MTMO) have attracted the much of the interest especially due to their use as heterogeneous catalysts [3,8,9,25–27]. However, the direct synthesis of MTMO is still a challenge to date. Despite the fact that the successful syntheses of numerous thermally stable MTMOs have been achieved, those efforts mostly focused on groups I-IV TMs such as Y, Ti, Hf, Zr, V, Nb, Ta, Cr, Mo, and W[14,15,28–33]. Some of the mesoporous groups I-IV TM oxides and inorganic-surfactant interactions ($G_{I\text{-}S}$) are summarized in **Table 1.1**. Moreover, compared to mesoporous silica materials, these MTMOs are not as well-ordered and not as porous as mesoporous silica and the control of structural parameters are also not an easy task. The difficulty of the synthesis of late MTMOs (groups V-X) arises from the lack of proper sol-gel chemistry, weak $G_{I\text{-}S}$ (due to filled d orbitals), and easily interchangeable oxidation states with multiple different crystal structures. Later MTMOs also suffer from having low thermal stability of the formed mesostructure, due to the low flexibility of the M-O-M bonds of the crystalline phases and therefore they cannot accommodate the curvature of the soft-templates (micelles) and increased ion mobility with

high temperature heat treatments, especially when the temperatures gets close to the Tamman temperature[16,34–36].

Table 1.1: Illustrative examples of some of the mesoporous group I-IV TM oxides, obtained crystal structures and inorganic-surfactant interactions (G_{I-S}).

Transition Metal	Crystal Structure	G_{I-S} (inorganic-surfactant interactions)	Ref.
Yttrium	Amorphous	Coulombic	135
Titanium	TiO_2 (anatase)	Charge Transfer	18
Zirconium	ZrO_2 (tetragonal)	Charge Transfer	18
Hafnium	Amorphous	Charge Transfer	15, 17
Vanadium	Amorphous	Charge Transfer & Hydrogen Bonding	22
Niobium	Nb_2O_5 & Amorphous	Charge Transfer & Coulombic	18, 33
Tantalum	Ta_2O_5 & Amorphous	Charge Transfer & Coulombic	18, 28
Chromium	Cr_2O_3	Charge Transfer	29
Molybdenum	α-MoO_3	Charge Transfer	31
Tungsten	Amorphous	Charge Transfer	32

1.3 General Synthetic Approaches

The surfactant and inorganic self-assembly and true liquid crystal templating approaches are direct synthesis methods and are only applicable to certain transition metal systems. The methods were first developed for silica and then modified and applied to other metal oxide systems. However, only a few of these resulting materials have structural properties comparable to silica. In addition, for the later TMs, the number of successful efforts are very limited and control of neither structural properties nor the crystal structure is possible. Therefore, use of silica as either a hard template for nanocasting or as a support has been the main path for the design of later TM MTMO synthesis for catalytic reactions. Well known mesoporous silica syntheses with easily tunable structural properties, easiness of template removal by chemical etching in basic solutions, and high thermal and structural stabilities have widened the use of mesoporous silica. A different type of nanocasting can also be performed by packing nano-crystals and filling the interstitial voids with inorganic precursors.

1.3.1 Direct synthesis multivalent MTMO by soft templating (surfactant micelles)

Mesoporous materials with ordered mesostructure are typically characterized by low-angle diffraction and a Type IV adsorption isotherm. Although there are numerous claims for mesoporosity in the literature, there are only a few with regular mesoporosity. Chromium oxide is one of the most promising oxidation catalysts due to its mixed valent nature (2+, 3+, 5+, 6+ oxidation states) [37]. The only known micelle templated mesoporous chromium oxide was synthesized by Sinha et al.[29,38]. The material has a cubic mesostructure and a Cr_2O_3 crystal phase which appeared after calcination. The synthesis requires long and multiple aging periods (7-14 days). Use of pluronic F127 surfactant gives thick mesopore walls (13 nm) which are probably the reason behind the thermal stability of the mesostructure. Despite the

material preserving mesostructure during calcination steps, the surface area drastically decreases from 212 m^2/g to 78 m^2/g after calcination at 500°C. Moreover, XPS analyses suggest a multivalent nature of chromium but not a pure 3+ state (Cr_2O_3).

Another multivalent TM with various oxidation states and crystal structures is manganese. Different from the chromium oxides, manganese oxides can also form microporous tunnel structures known as octahedral molecular sieves (OMS)[26,39]. Micelle templated mesoporous manganese oxides were synthesized first in 1997, but since then there has been no major progress for the synthesis of mesoporous manganese oxide[40–43]. The mesoporous materials obtained with the method of Tian et al. loses its mesostructure and mesoporosity mostly after calcination and the obtained surface areas are around ~50 m^2/g. This approach gave different crystal structures in different studies (γ-MnO_2, Mn_2O_3, Mn_5O_8, and Mn_3O_4) depending on heat treatment and post treatment conditions[41,42]. Moreover, the XPS analyses of these materials show impurities in the structure and the preexistence of Mn^{2+}, Mn^{3+} and Mn^{4+} states in the same material [41–43]. In a typical synthesis procedure, manganese nitrate was added to a charged surfactant (CTABr) solution and the pH was adjusted to 8. The columbic interaction between cationic surfactant and negatively charged manganese hydroxide layers is the driving force for the formation of the mesostructure.

Other multivalent transition metals forming multiple crystal structures are vanadium, iron, and cobalt oxides. There are no reported thermally stable mesoporous oxide structures for these TMs so far. Despite this, there are several reports for the synthesis of mesostructured iron oxide, and no thermal stability has been claimed so far[35,44–46]. 2D hexagonal and 3D cubic mesostructured materials can be synthesized by evaporation induced self assembly but retaining porosity after heat treatment still remains as a challenge[35]. Moreover, certain crystal

phases of transition metals are obtained by heating at high temperatures. Thermally unstable mesoporous TM oxides limit the use of these mesoporous materials in catalysis. From a catalytic point of view, heterogeneous catalysts are expected to be recyclable. Generally, to recycle the catalyst a regeneration step involves thermally removing adsorbed species from the surface. Therefore, thermal stability is an essential requirement. Similarly, for a gas phase catalytic reaction, a heterogeneous catalyst is expected to retain its catalytic activity for a substantial amount of time. The mesopore structure collapsed during stability tests due to high reaction temperatures after a period of time.

1.3.2 Thermal Stability by Reinforcement of mesostructures:

Thermally unstable mesostructures can be reinforced before heat treatment to ensure the mesoporosity after crystallization. The structures are reinforced by either carbon or silica. Trimethylsiloxy-methyl silane (BTMS) and hexamethyldisilazane (HMDS) are the most common precursors for silica coating on the internal mesopore wall[8,36,47]. They react with surface hydroxyl groups to form silica coatings and the coatings support the mesostructured material. The silica coating can easily be removed once the crystallization and stability of mesostructured TMs are established. Carbon can also be a good structural support. The surfactant in the as synthesized mesostructured material or a different carbon source introduced into the mesopores of the as synthesized material can be converted to carbon[8,10,36]. The organic compound is converted to carbon by heat treatment in either an inert atmosphere or under vacuum. After the crystallization of the mesostructure the carbon is removed by a second calcination step under air. Despite the fact that there are no reported mesoporous late TM oxides in which the mesostructure is supported by either silica or carbon, the reinforcement of the mesostructure of these TMs is promising.

1.3.3 Nanocasting Approach (The use of a hard template)

The use of a hard template is the most common approach for the synthesis of mesoporous late TM oxides because of the challenges in direct micelle templated syntheses. In this part of the chapter, we will give examples from manganese oxides for the illustration of the methods, since the methods are common to all TM oxides and one can find numerous examples for other TMs. The mesoporous hard template can be used either as a support to accommodate and stabilize the TM nano-particles or as a template for the synthesis of late mesoporous TM oxides by taking the replica of the existing pore structure of the template. The tunable mesostructure and the low bulk density of SiO_2 (~2.2 $g.cm^{-3}$) yield high specific surface area mesoporous silica materials, which makes them good candidates as support materials[25,48–50]. However, homogeneous distribution of the TM oxides on the support is not quite possible and generally oxide clusters exist as scattered nano-particles on the support (Figure 3a) [51,52]. The role of mesoporous silica as a hard template is more complicated and more parameters need to be considered. First, the filling of mesopores of the template is not always efficient and traditional impregnation methods generally result in formation of oxides both inside and outside the pore structure[51,53–55]. Second, the stability of the mesostructure upon template (silica) removal depends on the existence of intraconnecting micro or mesoporous tunnels, efficient filling of these tunnels, and also the TM loading amount is important[8,10,25,50,56]. Therefore, SBA-15, SBA-16, and KIT-6 are the mesoporous templates which have been most commonly used due to the fact that they contain intraconnecting channels which ensure the stability of the mesostructure of TM oxides after template removal. New synthetic approaches such as, *in situ* surfactant oxidation, ion-exchange, two solvent methods, and chemical vapor deposition help in efficient pore filling and contribute to the

stability of the mesostructure upon template removal[49,50,53–55,57]. The materials prepared from these approaches with sufficient TM loading preserved mesoporosity upon template removal.

1.4 References:

1. Kresge, C. T.; Leonowicz, M. E.; Roth, W. J.; Vartuli, J. C.; Beck, J. S. *nature* **1992**, *359*, 710–712.

2. Web of Knowledge http://apps.webofknowledge.com/summary.do?SID=4ETXCXJipj1aPEw9JFy&product=UA&qid=1&search_mode=GeneralSearch (accessed May, 20, **2013**).

3. Debecker, D. P.; Hulea, V.; Mutin, P. H. *Appl. Catal. A: Gen.* **2013**, *451*, 192–206.

4. Walcarius, A. *Chem. Soc. Rev.* **2013**, *42*, 4098.

5. Bibby, A.; Mercier, L. *Green Chem.* **2003**, *5*, 15–19.

6. Wu, Z.; Zhao, D. *Chem. Commun.* **2011**, *47*, 3332–3338.

7. Wagner, T.; Haffer, S.; Weinberger, C.; Klaus, D.; Tiemann, M. *Chem. Soc. Rev.* **2013**, *42*, 4036.

8. Ren, Y.; Ma, Z.; Bruce, P. G. *Chem. Soc. Rev.* **2012**, *41*, 4909.

9. Taguchi, A.; Schüth, F. *Microporous Mesoporous Mater.* **2005**, *77*, 1–45.

10. Vos, D. E. D.; Dams, M.; Sels, B. F.; Jacobs, P. A. *Chem. Rev.* **2002**, *102*, 3615–3640.

11. Grosso, D.; Cagnol, F.; Soler-Illia, G.; Crepaldi, E.; Amenitsch, H.; Brunet-Bruneau, A.; Bourgeois, A.; Sanchez, C. *Adv. Funct. Mater.* **2004**, *14*, 309–322.

12. Huo, Q.; Margolese, D. I.; Ciesla, U.; Demuth, D. G.; Feng, P.; Gier, T. E.; Sieger, P.; Firouz, A.; Chmelka, B. F.; Schüth, F.; Stucky, G. D. *Chem. Mater.* **1994**, *6*, 1176–1191.

13. Tian, B.; Liu, X.; Tu, B.; Yu, C.; Fan, J.; Wang, L.; Xie, S.; Stucky, G. D.; Zhao, D. *Nat. Mater.* **2003**, *2*, 159–163.

14. Boettcher, S. W.; Fan, J.; Tsung, C.-K.; Shi, Q.; Stucky, G. D. *Accounts Chem. Res.* **2007**, *40*, 784–792.

15. Schüth, F. *Chem. Mater.* **2001**, *13*, 3184–3195.

16. Lee, J.; Orilall, M. C.; Warren, S. C.; Kamperman, M.; DiSalvo, F. J.; Wiesner, U. *Nat. Mater.* **2008**, *7*, 222–228.

17. Yang, P.; Zhao, D.; Margolese, D. I.; Chmelka, B. F.; Stucky, G. D. *Nature* **1998**, *396*, 152–155.

18. Fan, J.; Boettcher, S. W.; Stucky, G. D. *Chem. Mater.* **2006**, *18*, 6391–6396.

19. Fan, J.; Boettcher, S. W.; Tsung, C.-K.; Shi, Q.; Schierhorn, M.; Stucky, G. D. *Chem. Mater.* **2008**, *20*, 909–921.

20. Brinker, C. J.; Scherer, G. W. *Sol-gel Science: The Physics and Chemistry of Sol-gel Processing*; Academic Press, 1990.

21. Soler-Illia, G. J. de A. A.; Crepaldi, E. L.; Grosso, D.; Sanchez, C. *Curr. Opin. Colloid & Interface Sci.* **2003**, *8*, 109–126.

22. De AA Soler–Illia, G. J.; Sanchez, C. *New J. Chem.* **2000**, *24*, 493–499.

23. Grosso, D.; Boissière, C.; Smarsly, B.; Brezesinski, T.; Pinna, N.; Albouy, P. A.; Amenitsch, H.; Antonietti, M.; Sanchez, C. *Nat. Mater.* **2004**, *3*, 787–792.

24. Soler-Illia, G. J.; Azzaroni, O. *Chem. Soc. Rev.* **2011**, *40*, 1107–1150.

25. Arends, I. W. C. E.; Sheldon, R. A. *Appl. Catal. A: Gen.* **2001**, *212*, 175–187.

26. Brock, S. L.; Duan, N.; Tian, Z. R.; Giraldo, O.; Zhou, H.; Suib, S. L. *Chem. Mater.* **1998**, *10*, 2619–2628.

27. Choudhary, T. V.; Banerjee, S.; Choudhary, V. R. *Appl. Catal. A: Gen.* **2002**, *234*, 1–23.

28. Antonelli, D. M.; Ying, J. Y. *Chem. Mater.* **1996**, *8*, 874–881.

29. Sinha, A. K.; Suzuki, K. *Angew. Chem.* **2005**, *117*, 275–277.

30. Bruce, D. W.; O'Hare, D.; Walton, R. I. *Porous Materials*; Wiley, 2011.

31. Brezesinski, T.; Wang, J.; Tolbert, S. H.; Dunn, B. *Nat. Mater.* **2010**, *9*, 146–151.

32. Yuan, J.; Zhang, Y.; Le, J.; Song, L.; Hu, X. *Mater. Lett.* **2007**, *61*, 1114–1117.

33. Vettraino, M.; Trudeau, M. L.; Antonelli, D. M. *Adv. Mater.* **2000**, *5*, 337–341.

34. Carreon, M. A.; Guliants, V. V. *Eur. J. Inorg. Chem.* **2005**, *2005*, 27–43.

35. Jiao, F.; Bruce, P. G. *Angew. Chem.* **2004**, *116*, 6084–6087.

36. Kondo, J. N.; Domen, K. *Chem. Mater.* **2008**, *20*, 835–847.

37. Weckhuysen, B. M.; Wachs, I. E.; Schoonheydt, R. A. *Chem. Rev.* **1996**, *96*, 3327–3350.

38. Sinha, A. K.; Suzuki, K. *Appl. Catal. B: Environ.* **2007**, *70*, 417–422.

39. Suib, S. L. *J. Mater. Chem.* **2008**, *18*, 1623–1631.

40. Suib, S. *Chem. Commun.* **1997**, 1031–1032.

41. Tian, Z.; Wang, J.; Duan, N.; Krishnan V. V.; Suib, S. L. *Science* **1997**, *276*, 926–930.

42. Sinha, A. K.; Suzuki, K.; Takahara, M.; Azuma, H.; Nonaka, T.; Fukumoto, K. *Angew. Chem. Int. Ed.* **2007**, *46*, 2891–2894.

43. Torres, J. Q.; Giraudon, J.-M.; Lamonier, J.-F. *Catal. Today* **2011**, *176*, 277–280.

44. Brezesinski, T.; Groenewolt, M.; Antonietti, M.; Smarsly, B. *Angew. Chem. Int. Ed.* **2006**, *45*, 781–784.

45. Jiao, F.; Harrison, A.; Jumas, J.-C.; Chadwick, A. V.; Kockelmann, W.; Bruce, P. G. *J. Am. Chem. Soc.* **2006**, *128*, 5468–5474.

46. Bruce, A. P.; Harrison, A. A.; Chadwick, A. A.; Jumas, A. J.; Jiao, A. F. *J. A. Chem. Soc.* **2008,** 128, 12905-12909.

47. Shirokura, N.; Nakajima, K.; Nakabayashi, A.; Lu, D.; Hara, M.; Domen, K.; Tatsumi, T.; Kondo, J. N. *Chem. Commun.* **2006**, 2188–2190.

48. Lide, D. R. *CRC Handbook of Chemistry and Physics: A Ready-reference Book of*

Chemical and Physical Data; CRC Press, 2004.

49. Gómez, S.; Giraldo, O.; Garcés, L. J.; Villegas, J.; Suib, S. L. *Chem. Mater.* **2004**, *16*, 2411–2417.

50. Poyraz, A. S.; Biswas, S.; Genuino, H. C.; Dharmarathna, S.; Kuo, C.-H.; Suib, S. L. *ChemCatChem* **2012**.

51. Jiao, F.; Frei, H. *Chem. Commun.* **2010**, *46*, 2920.

52. Imperor-Clerc, M.; Bazin, D.; Appay, M.-D.; Beaunier, P.; Davidson, A. *Chem. Mater.* **2004**, *16*, 1813–1821.

53. Dong, X.; Shen, W.; Zhu, Y.; Xiong, L.; Shi, J. *Adv. Funct. Mater.* **2005**, *15*, 955–960.

54. Kumar, G. S.; Palanichamy, M.; Hartmann, M.; Murugesan, V. *Microporous Mesoporous Mater.* **2008**, *112*, 53–60.

55. Jiao, F.; Harrison, A.; Hill, A. H.; Bruce, P. G. *Adv. Mater.* **2007**, *19*, 4063–4066.

56. Ryoo, R.; Joo, S. H.; Kruk, M.; Jaroniec, M. *Adv. Mater.* **2001**, *13*, 677–681.

57. Caps, V.; Tsang, S. C. *Catal. Today* **2000**, *61*, 19–27.

Chapter 2: A Novel Approach to Crystalline and Monomodal Pore Size Mesoporous Materials

2.1 Introduction

The seminal introduction of MCM-41 and M-41S mesoporous materials by Mobil researchers over 20 years ago has led to tens of thousands of research projects [1]. Since this time, variations on the Mobil process have produced various new mesoporous materials, doped materials, different compositions, and unique synthetic modifications such as replicas of various systems [2-4]. These syntheses have focused on use of water, or water plus a base, or water plus an acid or a chemical that varies the pH during the reaction with materials such as urea. Various charged (S^+ or S^-) or neutral surfactants (S^0) or a combination of these surfactants are used. There are either strong Coulombic interactions (S^+I^-; S^-I^+; $S^+X^-I^+$; $S^-X^+I^-$) or strong ligand metal interactions via hydrogen bonding or coordination type interactions and such systems have limited thermal stability and mostly amorphous walls, where I = inorganic species, and X is a mediator [5-10]. Such syntheses are open to air and various aging times and environmental conditions that can influence the porosity of these materials. Most studies of mesoporous transition metal oxide (MTMO) materials have focused on groups I-IV including Y, Ti, Hf, Zr, V, Nb, Ta, Cr, Mo, and W [6,7,11-16]. Sol-gel chemistry of these transition metals (TMs) can be controlled in alcoholic solutions with proper acidity adjustments and such metals interact strongly with polyethylene oxide groups of non-ionic surfactants by accepting electron density to their empty d-orbitals [17]. Such control and interactions do not exist for late TMs. Mesoporous materials synthesized by use of a soft template have low angle X-ray diffraction peaks indicating a meso-order and Type IV N_2 adsorption isotherms indicating a regular mesopore structure.

Water content is a critical parameter with porous transition metal oxide syntheses [18, 19]. Water competes with polyethylene oxide (PEO) groups of non-ionic surfactants and other alkoxy groups (from solvent or precursor) for coordination to the metal center. When excess water is used, these systems suffer from weak surfactant-transition metal (S-I) interactions and uncontrolled hydrolysis and condensation of inorganic sols. Since most syntheses are open to the air, the water content is very difficult to control, unless a humidity chamber is employed. Therefore, when the number of water molecules per metal atom (H) is > 1 phase separation and nonporous oxides are obtained [19]. On the other hand, water is essential for hydrolysis and condensation reactions and is also important for controlling the reaction rates. When H is < 1, ordered mesoporous materials are formed where the metal has empty d-orbitals to interact with solvents and surfactants [19]. These materials obtain water from the environment during synthesis or such an amount is intentionally added in controlled environments. When H is << 1, strong S-I interactions occur with weak surfactant-surfactant (S-S) interactions and resulting materials are either non-porous or do not have a regular mesopore structure [19].

Thermodynamic interactions in such syntheses and factors influencing each term are given in Equation 1, where ΔG_m is the Formation Energy of the mesostructured material; ΔG_{org} is the S-S interaction; ΔG_I is the inorganic-inorganic (I-I) interaction; ΔG_{inter} is the S-I interaction; and ΔG_{sol} is a contribution from solvent involved interactions [19,20]. Poor control of the last 2 terms, ΔG_{inter} and ΔG_{sol}, is the main reason why conventional approaches cannot be used for later TMs. Therefore, filled or half-filled d orbitals such as in systems containing Mn, Fe, Co, and others are difficult to make with other methods since charge transfer reactions do not occur and these metals are known to not have ideal sol-gel chemistry [19].

The objective of our new synthetic strategy concerns minimization of the effect of ΔG_{inter} and ΔG_{sol} parameters by carrying the entire reactants into inverse micelles in order to make well-ordered MTMO materials. Hydrolysis and condensation of the oxo-clusters (ΔG_I) in the inverse micelles are controlled by unique NOx chemistry formed *in-situ* by the thermal decomposition of nitrate ions. The resulting materials are monodispersed nano-particle aggregates and the mesopores are the connected intra particle voids. The structural parameters (unit cell, pore size, and pore volume) and crystallinity of the resulting mesoporous materials can be tuned by heat treatment cycles. The method is generic and allows one to synthesize mesoporous oxide materials from different parts of the periodic table such as late TMs (Mn, Co, Fe, Ni), early TMs (Ti, Zr), lanthanides (Ce), metalloids (Si), and non-metals (C).

$$\Delta G_m = \Delta G_{org} + \Delta G_I + \Delta G_{inter} + \Delta G_{sol} \quad (1)$$

2.2 Experimental Section

2.2.1 Materials Synthesis

2.2.1.1 Mesoporous first row TM oxides:

The Inorganic source (0.01-0.02 mol) was dissolved in a solution containing 0.188-0.27 mol of 1-butanol, 0.032-0.038 mol of HNO_3 and 2.04 - 4.08*10^{-4} mol of P123 surfactant in a 150 mL beaker at room temperature and under magnetic stirring. The obtained clear gel is placed in an oven at 95^0 - 120^0 C for 2 – 6 h. The obtained powder is washed several times with ethanol and then the powder is centrifuged. Finally, the powder is dried in a vacuum oven over night. The dried powders are subjected to heating cycles to achieve desired crystal structure and mesopore size. Supplementary **Table 2-1** shows the concentrations and reaction conditions used for each different metal system studied as well as the heating cycles applied. Heating cycles are needed to apply starting from the lowest temperature. For example, in order to heat a sample to 550^0C, first the material is heated to 150^0C for 12 h + 250^0C for 3-4 h +350^0C for 2-3 h+ 450^0C for 1-2 h. The powder is naturally cooled down to RT after each heating step. All heat treatments were done under air.

Table 2-1. Experimental parameters for various mesoporous transition metal oxides

***** We recommend performing all reactions in ovens with proper ventilation due to toxic NOx release from the gel during the reaction.

† Iron reaction should be done with caution since the reaction gel might splash towards to end of the reaction. We recommend placement of the beaker containing gel into a bigger beaker and partially coverage of the bigger beaker with a cover.

	Metal	Metal Amount (mol)	1-butanol (mol)	HNO_3 (mol)	P123 (mol)	Reaction Temperature & time (T ^oC & h)	Heating Cycles*
UCT 1 &2	Manganese	0.02	0.188	0.032	$3.4*10^{-4}$	120 ^{o} (4h)	150^o C (12h) 250^{o}C (4h) 350^{o}C (3h) 450^{o}C (2h) 550^{o}C (1h)
UCT 5&6	Iron†	0.01	0.12	0.019	$2.04*10^{-4}$	95 ^{o} (2-3h)	150^o C (12h) 250^{o}C (4h) 350^{o}C (3h) 450^{o}C (2h) 550^{o}C (1h)
UCT 7 &8	Cobalt	0.02	0.23	0.038	$4.08*10^{-4}$	120 ^{o} (4-6h)	150^o C (12h) 250^{o}C (4h) 350^{o}C (3h) 450^{o}C (2h) 550^{o}C (1h)
UCT 9 &10	Nickel	0.02	0.27	0.038	$4.08*10^{-4}$	120 ^{o} (4h)	150^o C (12h) 250^{o}C (4h) 350^{o}C (3h) 450^{o}C (2h) 550^{o}C (1h)

2.2.1.2 Mesoporous silica (UCT-14)

Tetraethylorthosilicate (TEOS) (0.02 mol) was diluted in a solution containing 0.188 mol (14 g) of 1-butanol, 0.032 mol (2 g) of HNO_3 and $3.4*10^{-4}$ mol (2 g) of P123 surfactant in a 150 mL beaker at room temperature and under magnetic stirring. The obtained clear gel was placed in an oven at 120^{o}C for 4- 6 h. The obtained transparent yellow film was placed in a calcination cuvette and calcined directly under air at 450^{o}C for 4 h (1^{o}C/min heating rate).

2.2.1.3 Mesoporous carbon (UCT-33)

As synthesized mesoporous silica sample (UCT-14) was placed in a tubular furnace and heated to 900^{0}C for 2 h under an Ar atmosphere. Resulting black material was put and stirred in a 0.5 M warm NaOH solution for etching out the silica to form mesoporous carbon. The formed black powder was washed several times with water and ethanol and dried in a vacuum oven over night.

2.2.1.4 Mesoporous zirconium oxide (UCT-17)

Zirconium (IV) butoxide (0.02 mol) was diluted in a solution containing 0.188 mol (14 g) of 1-butanol, 0.032 mol (2 g) of HNO_3 and $3.4*10^{-4}$ mol (2 g) of P123 surfactant in a 150 mL beaker at room temperature and under magnetic stirring. The obtained clear gel was placed in an oven at 120^{o}C for 4- 6 h. The obtained transparent greenish film was placed in a calcination cuvette and calcined directly under air at 450^{o}C for 4 h or 500^{o}C for 3 h or 600^{o}C for 1 h (2^{o}C/min heating rate).

2.2.1.5 Mesoporous cerium oxide (UCT-16)

Cerium (III) nitrate hexahydrate (0.02 mol) was dissolved in a solution containing 0.188 mol (14 g) of 1-butanol, 0.032 mol (2 g) of HNO_3 and $5.1*10^{-4}$ mol (3 g) of P123 surfactant in a 150 mL beaker at room temperature and under magnetic stirring. The obtained clear gel was placed in an oven at 120^0 C for 5 h. The obtained powder was washed several times with ethanol and then the powder was centrifuged. Finally, the powder was dried in a vacuum oven over night. The dried powders were subjected to heating cycles to achieve desired crystal structure and mesopore size. Heating cycles are needed to apply starting from the lowest temperature. For example, in order to heat a sample to 550^0C, first the material is heated to 150^0C for 12 h + 250^0C for 4 h +350^0C for 3 h+ 450^0C for 1 h + 550^0C for 1 h +600^0C for 1-2 h. The powder is naturally cooled down to RT after each heating step. All heat treatments were done under air.

2.2.1.6 Mesoporous tin oxide (UCT-31)

Tin (IV) tert-butoxide (0.012 mol) was diluted in a solution containing 0.134 mol (10 g) of 1-butanol and $2.6*10^{-4}$ mol (1.5 g) of P123 surfactant in a 150 mL beaker at room temperature and under magnetic stirring. To above gel, diluted nitric acid solution (1 g of (0.016 mol) HNO_3 + 5 g of 1-butanol) was added. The formed opaque white gel was stirred at RT for 1 h and then placed in an oven at 120^{o}C for 4 h. The obtained white material was placed in a calcination cuvette and calcined directly under air at 450^{o}C for 3 h (1^{o}C/min heating rate).

2.2.1.7 Mesoporous niobium oxide (UCT-35)

Niobium (V) chloride (0.01 mol) was dissolved in a solution containing 0.201 mol (15 g) of 1-butanol, 0.032 mol (2 g) of HNO_3 and $3.4*10^{-4}$ mol (2 g) of P123 surfactant in a 150 mL beaker at room temperature and under magnetic stirring. The obtained clear gel was placed in an oven at 120^oC for 4- 5 h. The obtained thick gel was placed in a calcination cuvette and calcined directly under air at 500^oC for 1 h (2^oC/min heating rate).

2.2.1.8 Mesoporous yttria stabilized zirconia (YSZ) (UCT-53)

Zirconium (IV) butoxide (0.02 mol) was diluted in a solution containing 0.188 mol (14 g) of 1-butanol, 0.032 mol (2 g) of HNO_3 and $3.4*10^{-4}$ mol (2 g) of P123 surfactant in a 150 mL beaker at room temperature and under magnetic stirring. To the above clear gel, 0.001 mol yttrium (III) nitrate hexahydrate was added and dissolved under magnetic stirring. The obtained clear gel was placed in an oven at 120^oC for 4- 6 h. The white material was placed in a calcination cuvette and calcined directly under air at 700^oC for 1 h (2^oC/min heating rate).

2.2.1.9 Mesoporous Cs promoted mesoporous manganese oxide (UCT-18-Cs)

Manganese (II) nitrate tetrahydrate (0.02 mol) was dissolved in a 1-butanol solution containing 0.188 mol (14 g) 1-Butanol, 0.032 mol (2 g) of HNO_3 and $3.4*10^{-4}$ mol (2 g) of P123 surfactant in a 150 mL beaker at room temperature and under magnetic stirring.. To this clear aqueous solution 100 µL of 2.0M $CsNO_3$ was added maintaining the Mn:X ratio 100:1. The resulting clear solution was then kept in an oven at 120^OC for 3 h under air. The resulting black powder was washed with excess ethanol, centrifuged and dried in vacuum oven overnight. The dried black powder was then heated to 150^OC for 12 h and 250^OC for 3 h under air.

2.2.2 Materials Characterization

Powder X-Ray diffraction analyses were performed on a Rigaku Ultima IV diffractometer (Cu Kα radiation, λ=1.5406 A) with an operating voltage of 40 kV and a current of 44 mA. FTIR spectra of powder samples were collected using a Thermoscientific Nicolet 8700 spectrometer. Sixty four scans were collected with a 4 cm^{-1} spectral resolution in the absorbance mode. Powder samples were diluted with KBr and pellets were pressed from the powder mixture. UV-Vis spectra of reaction gels at different time intervals were recorded by Shimadzu UV-2450 UV-Vis spectrophotometer. Diffuse Reflectance UV-Vis spectra of the powder samples were collected with a DR apparatus attached on Shimadzu UV-2450 UV-Vis spectrophotometer. The powder samples were diluted in barium sulfate and pressed into sample holder. ATR-FTIR spectra of reaction gels were collected by Thermoscientific Nicolet iS5 FT-IR spectrometer equipped with iD3 ATR accessory (ZnSe). For time dependent COO- and NOx desorption studies, the samples are diluted with KBr and pelletized (133 mm diameter). FTIR spectra of the pellets were collected using a Thermoscientific Nicolet 8700 spectrometer equipped with MCT/A detector. Sixty four scans were collected with a 4 cm^{-1} spectral resolution in the absorbance mode. Temperature programmed desorption mass spectrometry (TPD-MS) analyses were performed with a homemade setup and an MKS-UT1 PPT quadrupole mass spectrometer. 100 mg of as synthesized mesoporous material was packed in a quartz tube and the tube was placed into a horizontal tubular furnace. The loaded sample was heated from RT to 300^{o}C with a 5^{o}C/min heating rate under 50 sccm air flow (or He). The tracked masses (m/z) are 28 (CO), 30 (NO), 32 (O_2), 44 (CO_2), and 46 (NO_2). Morphological characterization was done using a Zeiss DSM 982 Gemini field emission scanning electron microscope (FESEM) with a Schottky emitter at an accelerating voltage of

2.0 kV and a beam current of 1.0 mA. Nitrogen sorption experiments were conducted on a Quantachrome Autosorb-1-1C automated adsorption system. The powders were degassed for 6 h prior to measurement. High-resolution transmission electron microscopy (HRTEM) images of synthesized mesoporous materials were recorded on a JEOL 2010 FasTEM microscope operating at 200 kV.

2.2.3 Catalytic Studies (Double oxidation and in-situ esterification)

1-Decanol (1mmol), catalyst (100mg) and toluene (15ml) were taken in a 50 ml two necked round bottom flask equipped with a condenser. The flask was immersed in a silicon oil bath preheated to 110^{O}C. The reaction mixture were refluxed and stirred for 15 h under air flow. The mixture was cooled after the reaction, the catalyst was removed by filtration, and Gas chromatography/ Mass spectrometry (GC/MS) was used to analyze the filtrate. The conversion was measured by comparing the peak areas of reactant and products. The selectivity was measured as follows: (peak area of particular product/ peak area of all products) * 100.

2.3 Results

2.3.1 General Synthetic Approach and Characterization of Reaction Gel:

Our novel sol-gel based inverse micelle method (**Figure 2.1**) uses HNO_3 at low pH to hinder condensation; metal oxo-clusters are stabilized; and the clusters are confined in hydrated inverse micelles and interact with surfactant via hydrogen bonding. The surfactant species is P123, inverse micelles formed by surfactant species serve as nano-reactors, and individual surfactant molecules in inverse micelles also form a physical barrier between the oxo-clusters preventing uncontrolled aggregation. An interface modifier like 1-butanol (for both PEO and PPO) compensates for the decrease of the aggregation number (AN), hinders the condensation by forming a physical barrier between the oxo-clusters, and limits oxidation of surfactant molecules (by TM clusters) present in the micelle. The hydrotropic nitrate ion increases solubility of P123, penetrates into the micelle and decreases the AN, pulls the positively charged metal oxide clusters into the micelle and hydrates the core [21]. The existence of NO_3^- ion in the developed method is essential and has multiple roles. Another and a more important role arises from the unique chemistry of nitrate ions. Thermal decomposition of nitrate ions forms a wide range of chemicals referred to as NO_x [22, 23]. Formation of NO_x changes the color of the gel to yellow (~60 min). The formed NO_x species coordinate to oxo-clusters which can be realized from the five sharp absorption bands in region of 320 – 400 nm (**Figure 2.2a**). The disappearance of color in the next 30 min is followed by a quick increase in pH and formation of mesoporous oxides, since decomposition of NO_x quickly consumes H^+ in this environment. In order to validate the role of NO_x chemistry, a set of control experiments were conducted. For these experiments, two reaction gels prepared by leaving surfactant or metal source out. In lack of metal source, NOx formation (yellow gel) did not

form five sharp absorption band in 320-400 nm region, instead it only created a broad absorption peak (**Figure 2.3a**). On the other hand, the five absorption bands were observed for surfactant free gel, despite resulting final material was non-porous. Formation and disappearance of the yellow color and also formation of the mesoporous oxides upon decolorization of the gel are observed in other studied systems. **Figure 2.3b** and **c** show the UV-Vis spectra of the reaction gels of mesoporous cobalt and nickel respectively. The reaction gels show the characteristic sharp absorption bands origination from NO_x adsorption on metal oxo-clusters. The formation of coordinated nitrate species upon coordination of NO_x on oxo-clusters is also confirmed by Attenuated Total Reflectance Fourier Transform Infrared ATR-FTIR spectroscopy (**Figure 2.3d**) [22].

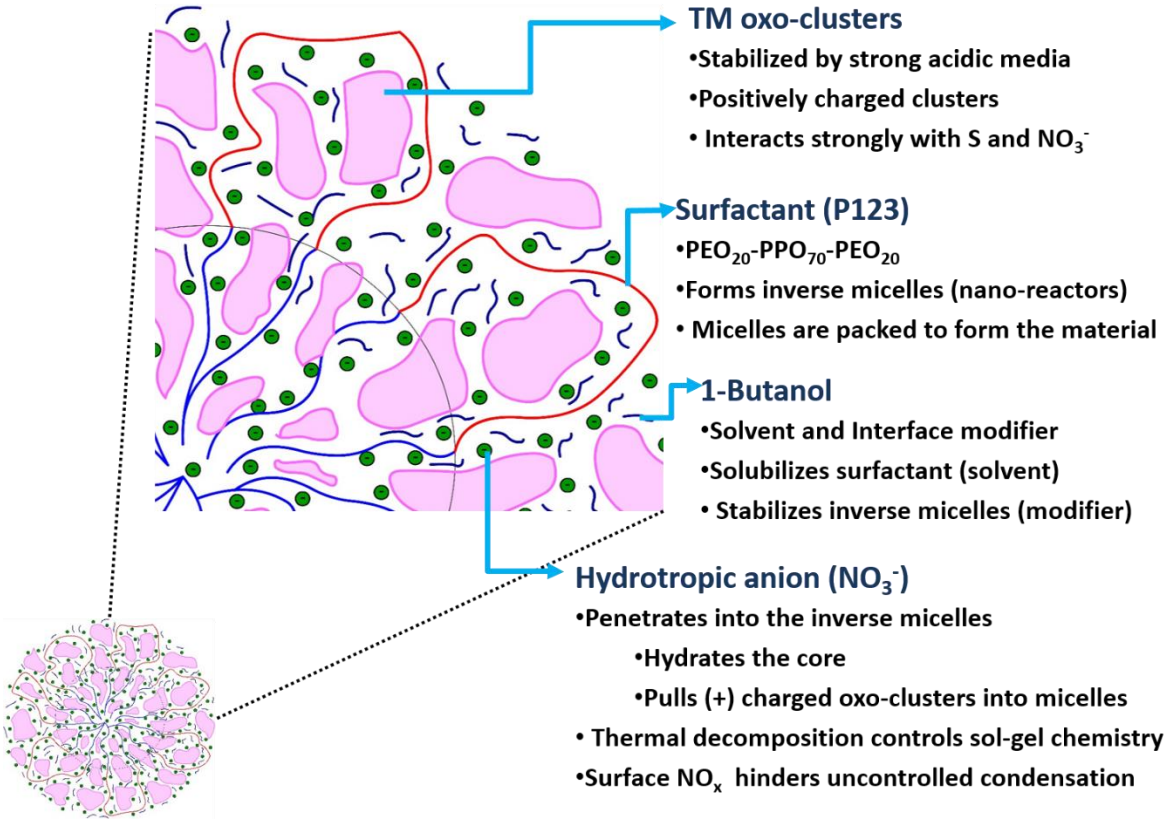

Figure 2.1: Inverse micelle sol-gel method and roles of components: **TM oxo-clusters:** positively charged oxo-clusters interact with surfactant via hydrogen bonding and the charge is balanced by negatively charged nitrate ions (NO_3^-). **Surfactant (P123)**: inverse micelles are formed by P123 (PEO_{20}–PPO_{70}–PEO_{20}) surfactant. Later, the inverse micelles are packed to form the material. **1-Butanol:** solubilizes the surfactant (solvent) and stabilizes inverse micelles (modifier). **Nitrate ion (NO_3^-):** hydrotropic nitrate anion penetrates into the core of inverse micelles to hydrate it and pulls positively charged oxo-clusters into the micelles. Thermal decomposition of nitrate ions form nitric oxides (NOx) to control the sol-gel chemistry. Formed NOx is adsorbed on oxo-clusters to hinder uncontrolled condensation.

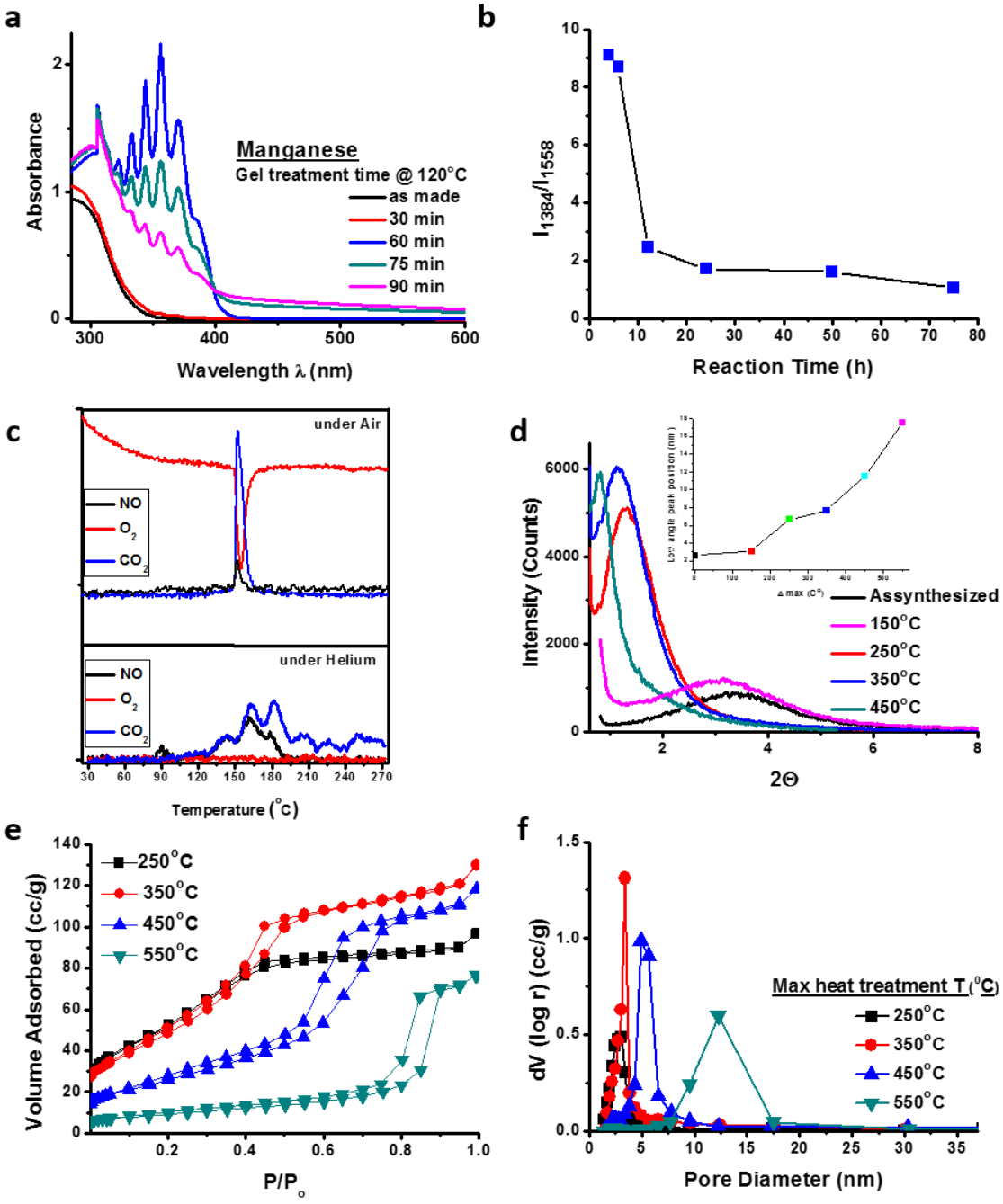

Figure 2.2: Characterization of the reaction gel and materials. **(a)** UV-Vis spectra of mesoporous manganese oxide reaction gel heated at 120 °C for 0–90 min. **(b)** Normalized FTIR intensity ratio of I_{v1} of NO_3^- (at 1,384 cm^-1) and I_{vas} of R-COO^- (at 1558cm^-1) of solvent-extracted samples synthesized at different reaction times. **(c)** TPD of as-synthesized mesoporous manganese oxide under air and helium flow (50 cc min^-1) in 30– 275 °C region. **(d)** Low-angle PXRD and low-angle peak positions (nm), **(e)** N_2 sorption isotherms and **(f)** BJH desorption pore-size distributions of mesoporous manganese oxide (Meso-Mn-X) samples heat treated at different final temperatures.

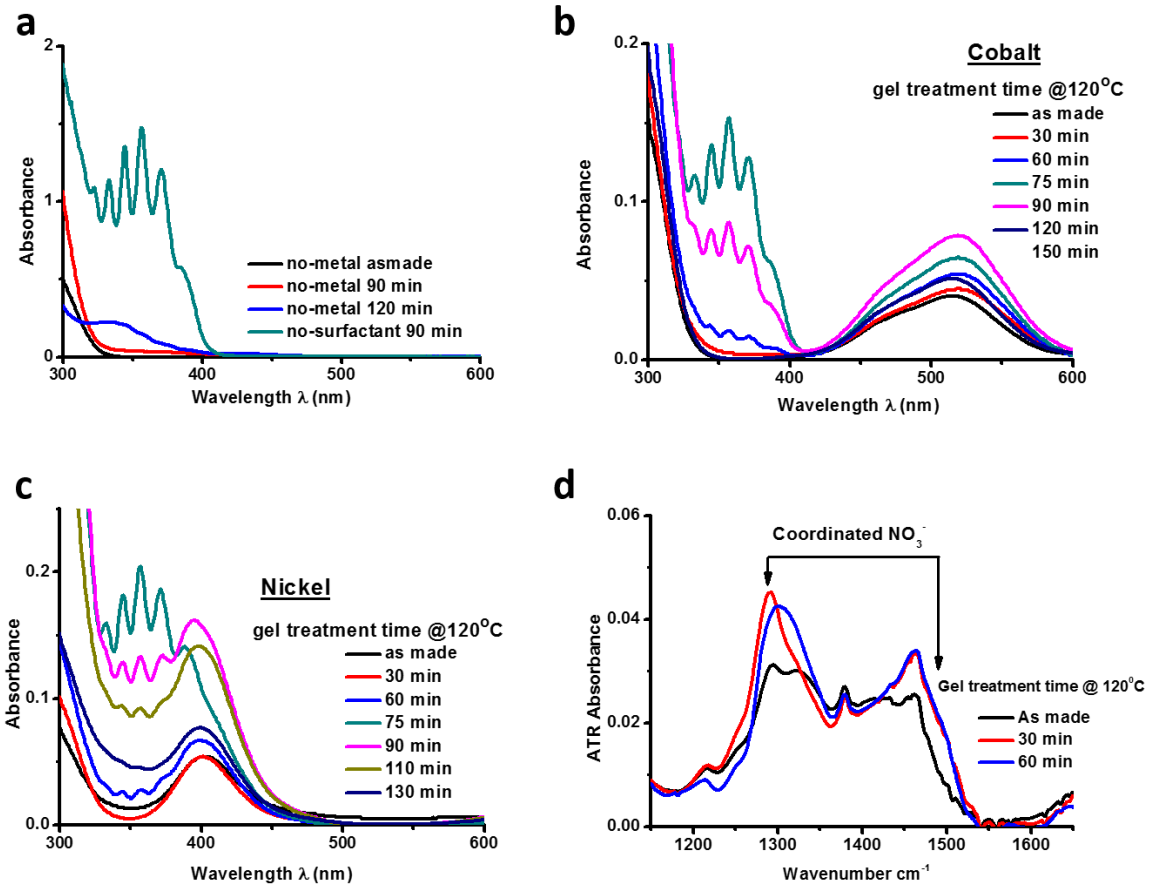

Figure 2.3 Reaction gel characterization: UV-Vis spectra of **(a)** reaction gel without metal (manganese) or surfactant (P123), **(b)** mesoporous cobalt oxide reaction gel, **(c)** mesoporous nickel oxide reaction gel heated at 120^{0}C for 0-130 min, and **(d)** ATR-FTIR spectra of reaction gel of mesoporous manganese oxide.

During this process, surfactant species are oxidized at long reaction times and form carboxyl groups coordinated to metal oxygen clusters and compete with nitrate to exist in the micelles. Therefore, during the synthesis, carboxylate bands increase while nitrate related bands decrease. The relative ratio of spectra [normalized with respect to the Mn-O stretching band (584 cm^{-1})] confirms that reaction times longer than 6 h (t > 6 h) result in oxidation of surfactant to form carboxyl groups (**Figure 2.2b** and **Figure 2.4a**) here for manganese based systems. These samples (t > 6 h) show thermal stabilities up to 250^{o}C, whereas samples at t

< 6 h have a thermal stability up to 550^{o}C (based on the disappearance of the low-angle diffraction line). The carboxyl groups and nitrates formed on as synthesized manganese oxide samples are oxidized and removed at 150^{o}C (**Figure 2.4b**). Nitrate ions do not fully disappear until 250^{o}C. The carboxyl and nitrate removal was also monitored by temperature programmed desorption (TPD) studies under air and He flows (**Figure 2.2c**). The carboxyl groups leave the surface as CO_2 and nitrate groups leave the surface as NO in temperature range of 150-170^{o}C under air flow. However, under helium flow desorption of CO_2 and NO are slower and occur at higher temperatures. Moreover, PXRD pattern of used material (under He flow) shows Mn_3O_4 phase suggesting reduction of Mn species by carboxyl and nitrate removal (**Figure 2.4c**). The mesostructured manganese materials with Mn_3O_4 phase does not show thermal stability and low-angle diffraction line disappears at temperatures above 250^{o}C. Therefore, the carboxyl and nitrate removal should be done under air atmosphere.

The process of carboxyl and nitrate removal was also monitored for other metal systems mentioned in the manuscript (Fe, Co, and Ni) (**Figure 2.5a**). TPD and FTIR data show very similar desorption profiles and for all metal systems carboxyl and nitrate species are removed in the 150-190^{o}C temperature range. The carboxyl groups are mostly removed by heating the as synthesized materials at 150^{o}C for 12 h and followed by heating at 250^{o}C for 1-4 h. The removal process was also followed by recording FTIR spectra of the powders at different time intervals during the heating process (**Figure 2.5b, c, and d**). The carboxyl groups and nitrate ions need to be mostly removed before proceeding with further heat treatment to preserve the mesoporous structure (for the synthesis of mesoporous materials from late transition metals, see text). Failure to remove the carboxylate groups and nitrate ions leads to thermally unstable mesoporous materials. All directly heated samples show no or very

weak low-angle diffraction lines and all show non-porous features in N_2 analyses along with very low BET surface areas.

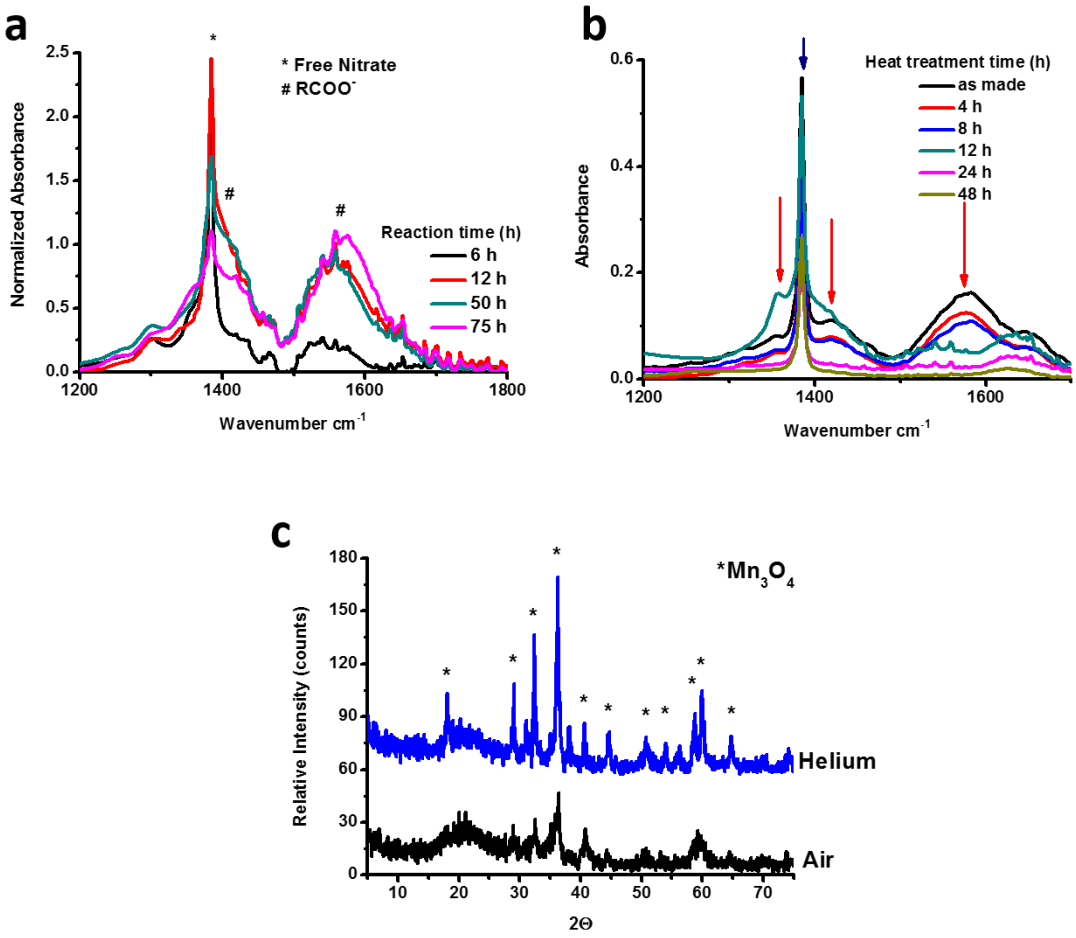

Figure 2.4 Characterization of as synthesized mesostructured manganese oxide: FTIR spectra of **(a)** as synthesized mesoporous manganese oxide at different reaction times and **(b)** heat treatment of as synthesized (12 h) mesoporous manganese oxide at 150^0C for 0-48 h. **(c)** Wide-angle PXRD patterns of mesoporous manganese oxide samples after TPD analyses.

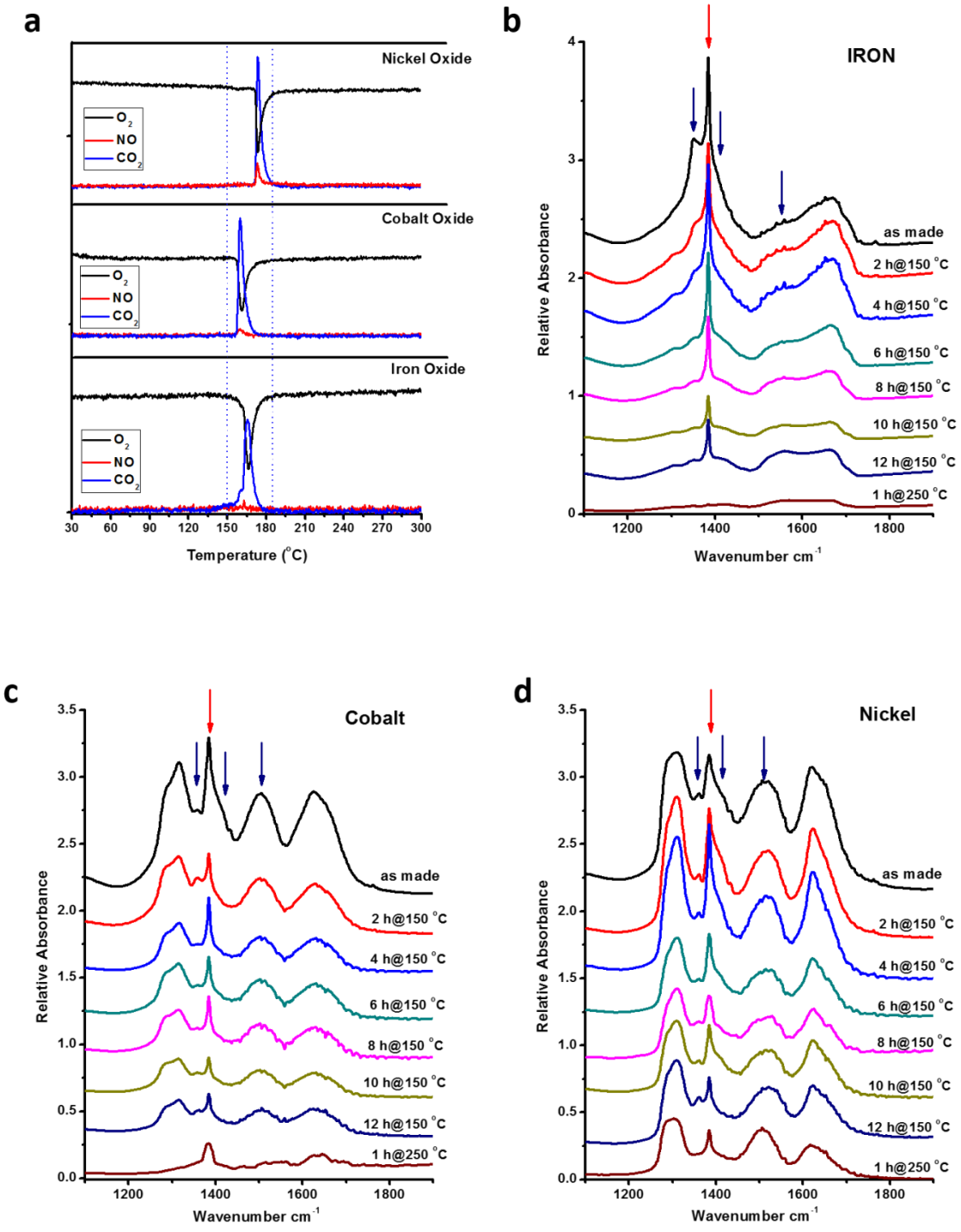

Figure 2.5 NOx and COO^- removal: (a) Temperature Programmed Desorption (TPD) of as synthesized mesoporous iron, cobalt, and nickel oxide samples under air flow (50 cc/min) in 30-275^{o}C region. The FTIR spectra of heat treatment of as synthesized mesoporous **(b)** Iron, **(c)** Cobalt, and **(d)** Nickel oxides at 150^{0}C for 0-12 h and at 250^{0}C for 1 h.

2.3.2 Physicochemical Properties of Mesoporous TM Oxides

A typical ordered mesoporous material is characterized by a low-angle diffraction line(s) indicating existence of a mesostructure and a Type IV adsorption isotherm indicating a regular nano-sized pore structure. In addition, both mesopore size and unit cell contradict upon template removal (by calcination) or heat treatment due to further condensation of the inorganic wall. A remarkable observation is that during thermal treatment both the d-spacings and the pore sizes increase for inverse micelle templated UCT mesoporous materials. **Figure 2.2d** shows the low angle diffraction lines for mesoporous manganese oxide samples heated to different final temperatures. The low-angle diffraction line position gradually shifts from 3.1 nm to 17.5 nm (unit cell expansion) by increasing the final heat treatment temperature from 150^{o}C to 450^{o}C (**Table 2.2**). Similarly, BJH desorption pore diameters increase (from 2.0 to 12.5 nm) with the heat treatment and regardless of the heat treatment temperature the materials show characteristic Type IV adsorption isotherms suggesting the materials preserve the mesoporous structure (**Figure 2.2e** and **f**).

Corresponding BET surface area (100-260 m^2/g), pore size distributions, and pore volumes (up to 0.22 cc/g) (**Figure 2.2c, d,** and **e** and **Table 2.2**) show that these University of Connecticut (UCT) mesoporous materials are produced with excellent control of pore size distributions. Such control of pore size distribution, enhanced pore volumes, and thermal stabilities are unprecedented with transition metal oxide mesoporous materials [25]. Wide-angle PXRD patterns of the mesoporous manganese oxide samples heated to different final temperatures are given in **Figure 2.6** and **Table 2.2**. The materials are amorphous at low temperatures (150^{o}C- 350^{o}C) and become crystalline with Bixbyite (Mn_2O_3) phase at high temperatures (450^{o}C & 550^{o}C).

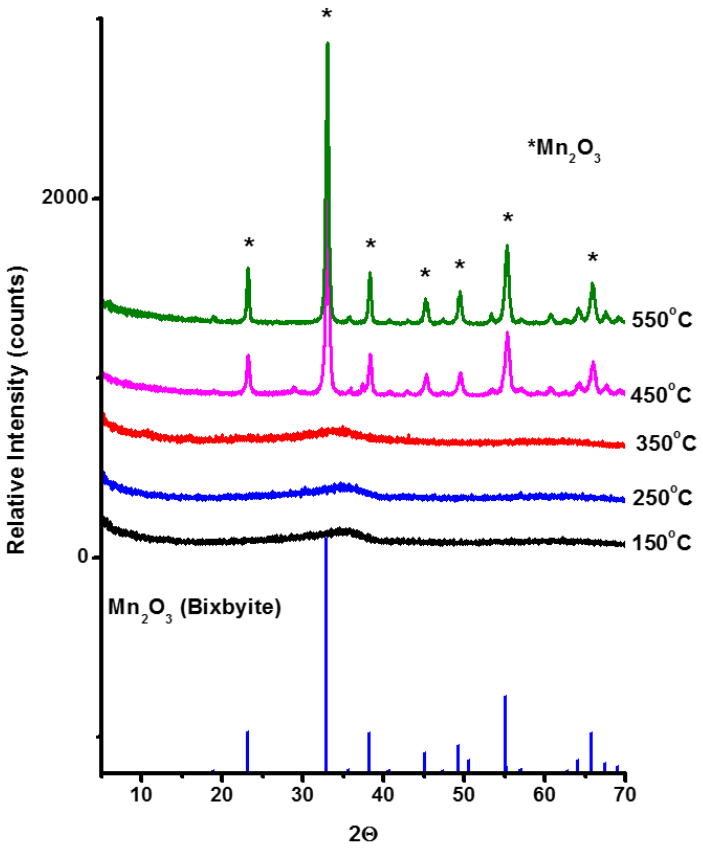

Figure 2.6 High angle PXRD patterns of mesoporous manganese oxide samples heated treated at different final temperatures.

Table 2.2 Structural parameters of mesoporous materials discussed in the thesis.

Metal	Title (Meso-M-X[#])	Naming	Max Heat Treatment T (ºC)	Surface Area (m^2/g)	BJH Des. Pore Diameter (nm)	Low-Angle XRD peak position (nm)	Crystal Structure
Manganese	Meso-Mn-X	UCT-1	150	255	2.0*	3.1	Amorphous
			250	200	2.8	6.7	Amorphous
			350	191	3.7	7.7	Amorphous
		UCT-2	450	100	5.3	11.5	Mn_2O_3
			550	35	12.3	17.5	Mn_2O_3
Iron	Meso-Fe-X	UCT-5	150	124	1.54*	4.2	Amorphous
			250	225	2.2	5.0	Amorphous
		UCT-6	350	167	3.4	7.9	Fe_2O_3
			450	46	9.6	24.5	Fe_2O_3
Cobalt	Meso-Co-X	UCT-7	150	9	Non-porous	9.3	Co_3O_4 & $Co_3O_4.4H_2O$
		UCT-8	250	129	5.7	12.2	Co_3O_4
			350	110	7.8	14.5	Co_3O_4
Nickel	Meso-Ni-X	UCT-9	150	20	Non-porous	6.6	NiOOH & $Ni(OH)_2.0.75H_2O$
		UCT-10	250	195	5.5	7.4	$Ni_{15}O_{16}$
			350	81	9.7	9.6	$Ni_{15}O_{16}$
			450	60	9.7	9.8	$Ni_{15}O_{16}$
Silica	Meso-Si	UCT-14	450[ǂ]	435	1.4*	4.6	Amorphous
Carbon	Meso-C	UCT-33	900ºC (Ar) for 2 h	290	3.7	10.3	NA
Ceria	Meso-Ce-X	UCT-16	150	98	NA	2.9	CeO_2
			250	152	1.1*	3.2	CeO_2
			350	173	1.1*	3.4	CeO_2
			450	156	1.3*	3.7	CeO_2
			550	127	1.6	5.1	CeO_2
			600	72	1.9	7.1	CeO_2
zirconia	Meso-Zr	UCT-17	450[ǂ]	132	3.4	7.8	ZrO_2 (tetragonal)
			500[ǂ]	117	3.5	9.1	ZrO_2 (tetragonal)
			600[ǂ]	80	3.8	13.6	ZrO_2 (monoclinic & tetragonal)

Cs promoted manganese	**Meso-Cs[Mn**	**UCT-18**	250	152	3.4	7.6	Amorphous
Cadmium (sulfide)	**Meso-CdS**	**UCT-29**	NA	66	3.8	6.2	CdS (Hawleyite)
Tin	**Meso-Sn**	**UCT-31**	450[ǂ]	94	8.5	9.9	SnO
Niobium	**Meso-Nb**	**UCT-35**	500[ǂ]	117	6.1	8.3	Amorphous
Yttria stabilized zirconia	**Meso-YSZ**	**UCT-53**	700[ǂ]	82	3.4	12.6	ZrO_2 (tetragonal)

[ǂ] As synthesized samples are directly calcined at indicated temperature.
* DFT pore size distributions
# X is the final heating temperature for the step wise heated samples.

Figure 2.7a shows FESEM images for mesoporous manganese oxides at various stages of thermal treatment in the synthesis showing development of pores. At 450^{o}C, one can see uniform pores in these FESEM images all over the material. The TEM data of mesoporous manganese oxide and nickel oxide (**Figure 2.7b** and **c**, respectively) are also typical of all these materials and show that these systems are made of small crystalline nano-size particles that are organized and that remain stable even with thermal treatments at elevated temperature

(550°C for manganese). The nano-particle size and pore size increased were also monitored for mesoporous manganese systems heated to different final temperatures with TEM. **Figure 2.8** shows the TEM images of mesoporous manganese oxide from the same experimental batch and heated to different final temperatures. All TEM images are collected with same magnifications, so one can easily realize the progressive growth of both the pore size and nano-particles with temperature increase.

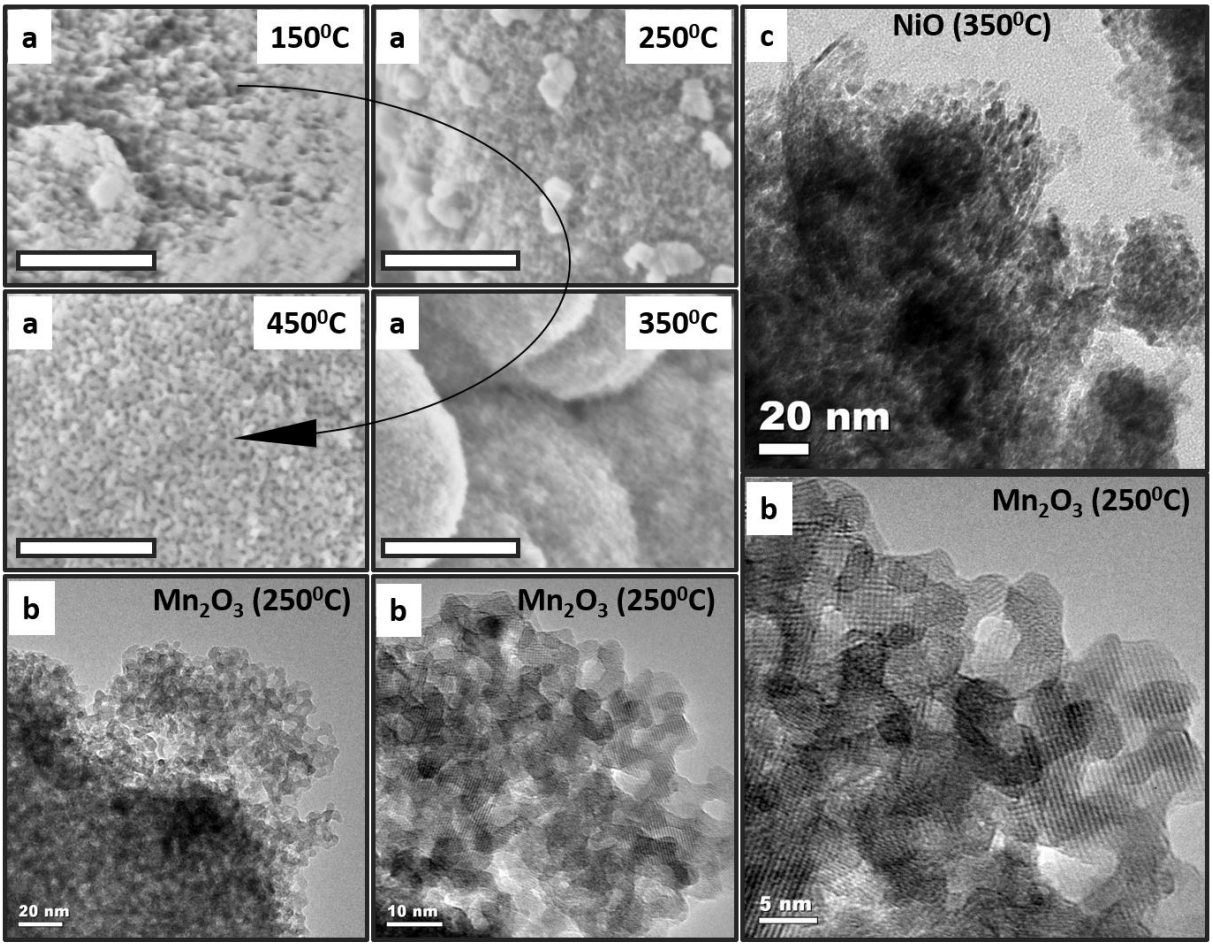

Figure 2.7 Electron Microscopy images (a) FESEM images of mesoporous Mn_2O_3 after heat treatments at different temperatures (scale bar, 200 nm). HRTEM images of **(b)** mesoporous Mn_2O_3 (250⁰C) (scale bars, 20 nm, 10 nm, and 5 nm from left to right) and **(c)** mesoporous NiO (350⁰C) (scale bar, 20 nm).

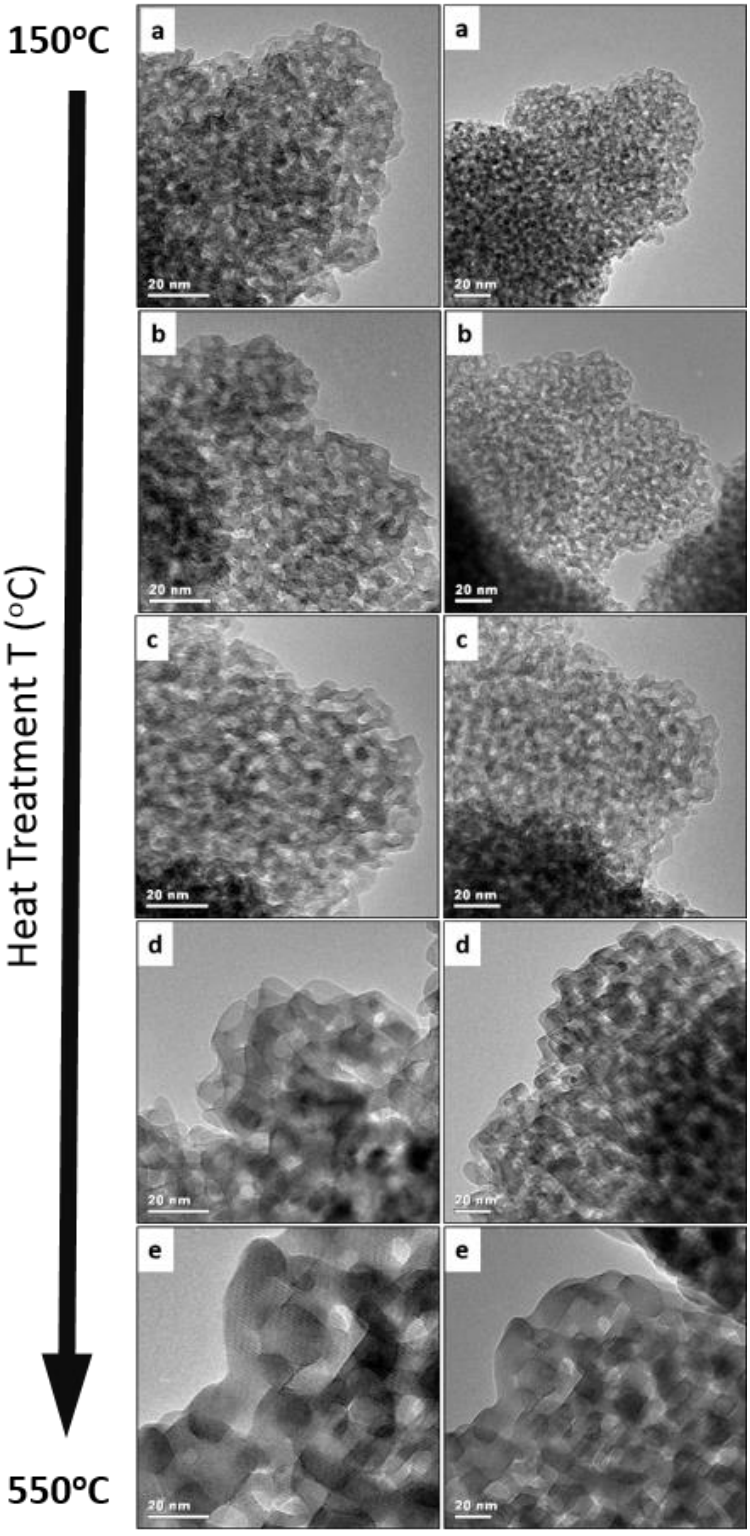

Figure 2.8 HR-TEM images of mesoporous manganese oxide at different final heat treatment temperatures: (a) 150, (b) 150, (c) 250, (d) 250, (e) 350, (f) 350, (g) 450, (h) 450, (i) 550 and (j) 550 _C (scale bars, 20 nm).

Pore expansion and d-spacing increase with thermal treatment were also observed in other TM systems (iron, cobalt, and nickel) studied. Low- and wide angle PXRD patterns, N_2 sorption isotherms, BJH desorption pore size distributions, FESEM, and TEM images of mesoporous iron (UCT-5 &6), cobalt (UCT-7 & 8), and nickel (UCT-9 & 10) are demonstrated in supplementary **Figure 2.9**, **Figure 2.10**, and **Figure 2.11** respectively. The temperature (heat treatment) dependent unit cell increase (a decrease at low-angle diffraction line position) and pore expansion were also observed for these materials. As in the manganese system (UCT-1), HR-TEM images for other mesoporous materials also demonstrate the nano-particle aggregate nature of the UCT materials. The thermal stability of these materials are similar to manganese system and mesostructure (low-angle diffraction line) disappears at 500^{o}C, 400^{o}C, and 500^{o}C for iron, cobalt, and nickel systems respectively. The heat treatment temperatures reported in **Table 2.2** are final and any further temperature increase results in disappearance of the mesostructure.

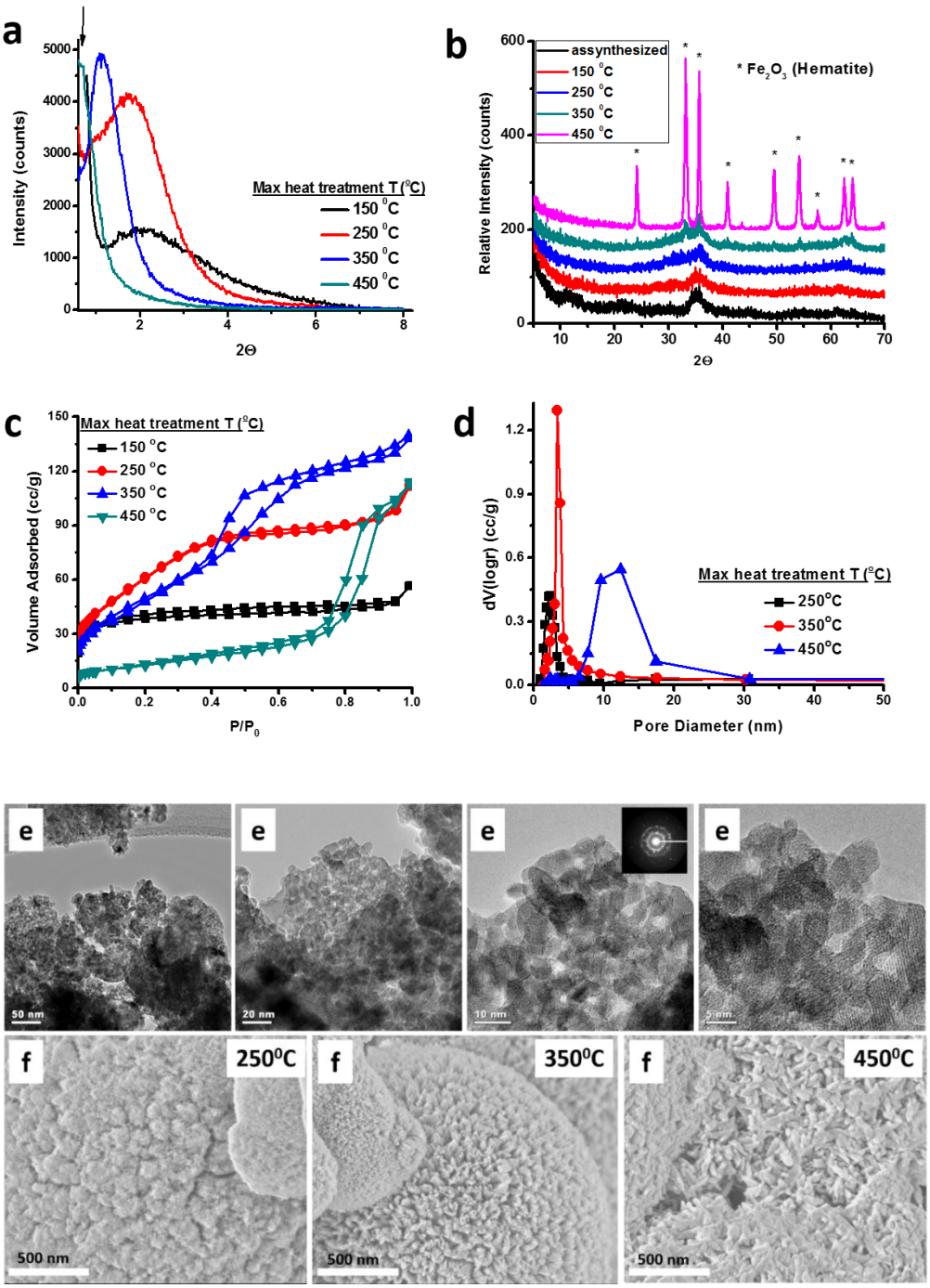

Figure 2.09 Characterization of mesoporous iron oxide. (a) Low and **(b)** High angle PXRD patterns **(c)** N_2 sorption isotherms and **(d)** BJH desorption pore size distributions of mesoporous iron oxide (UCT-5 and UCT-6) samples heated treated at different final temperatures. **(e)** HR-TEM images of UCT-6 (350^{o}C) **(**scale bar, 50, 20, 10, and 5 nm, from left to right respectively**)** and **(f)** FESEM images of UCT-5 (250^{o}C) and UCT-6 (350^{o}C and 450^{o}C) (scale bar, 500 nm).

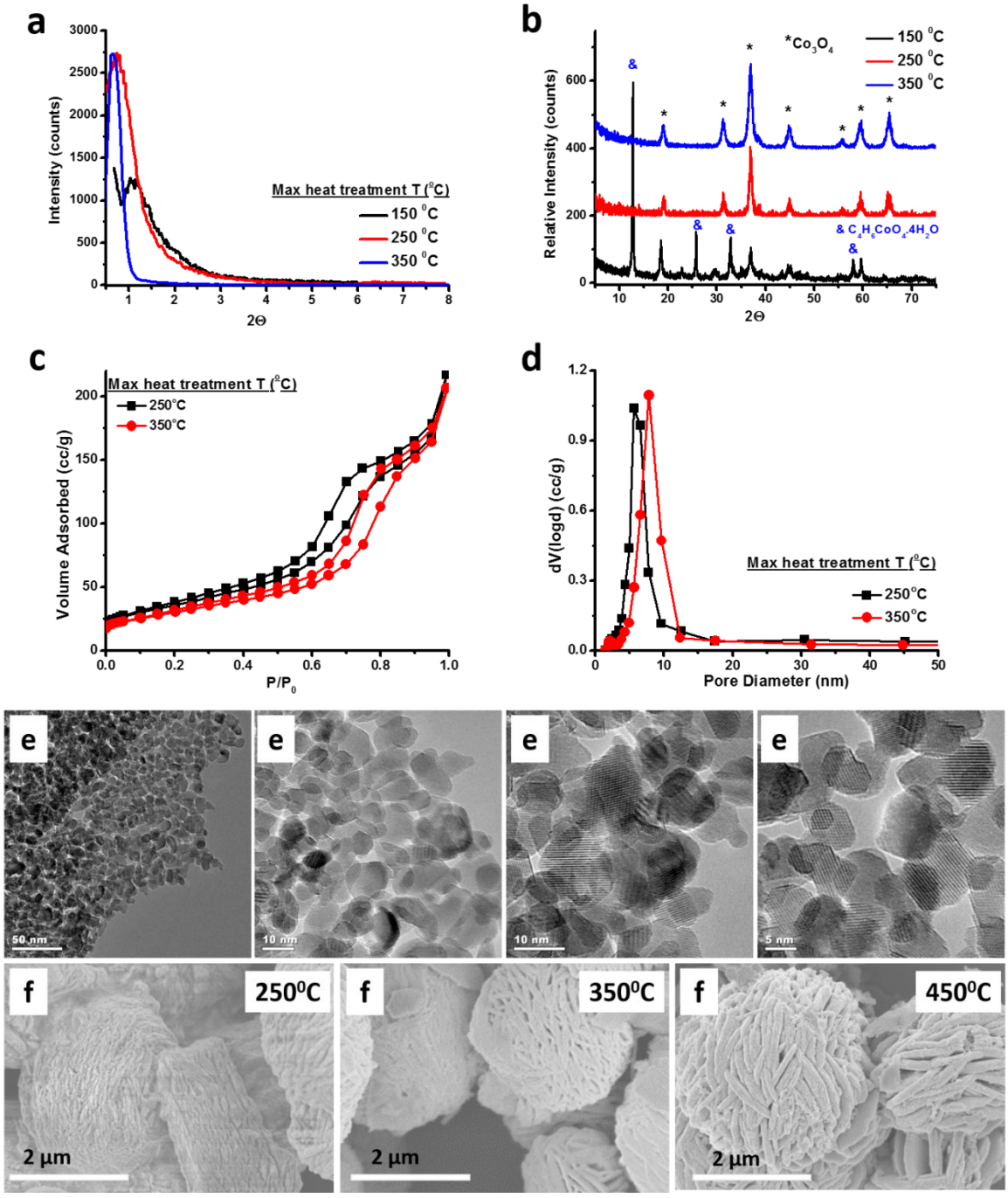

Figure 2.10 Characterization of mesoporous cobalt oxide. (a) Low and **(b)** High angle PXRD patterns **(c)** N_2 sorption isotherms and **(d)** BJH desorption pore size distributions of mesoporous cobalt oxide (UCT-7 and UCT-8) samples heated treated at different final temperatures. **(e)** HR-TEM images of UCT-7 (250^{o}C) **(**scale bar, 50, 10, 10, and 5 nm, from left to right respectively**)** and **(f)** FESEM images of UCT-7 (250^{o}C) and UCT-8 (350^{o}C and 450^{o}C) (scale bar, 2µm).

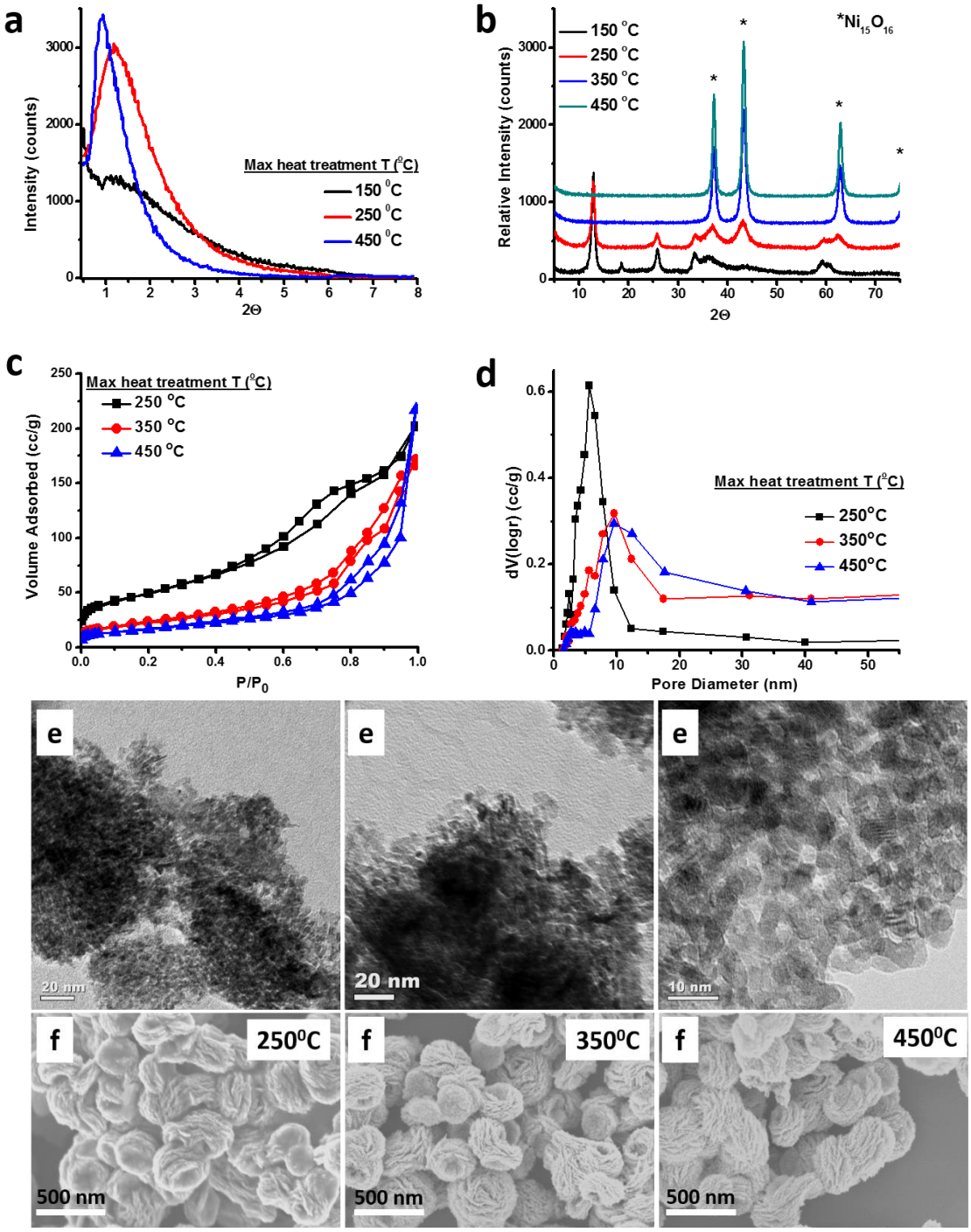

Figure 2.11 Characterization of mesoporous nickel oxide. (a) Low and **(b)** High angle PXRD patterns **(c)** N_2 sorption isotherms and **(d)** BJH desorption pore size distributions of mesoporous nickel oxide (UCT-9 and UCT-10) samples heated treated at different final temperatures. **(e)** HR-TEM images of UCT-10 (350°C) **(**scale bar, 50, 20, and 10 nm, from left to right respectively**)** and **(f)** FESEM images of UCT-10 (250°C, 350°C and 450°C) (scale bar, 500 nm).

There are several advantages of this method including control of the crystal structure of the wall during heating, there is precise control of pore size, and most importantly the method has been demonstrated to work for synthesizing numerous mesoporous oxides. The generality of the approach is illustrated for various oxide materials from different parts of the periodic table which are shown in **Figure 2.12** to **17** and **Table 2.2**. One TM from group IV (Zr (UCT-17)), one TM from group V (Nb (UCT-35)), one post-TM (Sn (UCT-31)), one lanthanide (Ce (UCT-16)), and one mixed metal (yttria stabilized zirconia (YSZ (UCT-53)) are used to demonstrate the generality of the approach. For the syntheses of mesoporous Si and Zr alkoxide sources were used and chloride source was used in the Nb system. These data suggest that the method is not limited only to nitrate sources. However, a sulfate source results in cloudy gels or surfactant precipitation out of the gel. Since the main nitrate source is nitric acid, enough nitrate is still present in the reaction gel when non-nitrate sources are used. Different from the late transition metals (Mn, Fe and Co), the adsorbed NO_x and carboxyl species on the surface of as synthesized materials are not a concern for these systems, since they do not have the possibility of forming multiple oxidation states. Therefore, these materials were directly calcined at a target temperature for a certain time (see methods part). All materials show characteristic one low-angle diffraction line, and the position of the line shifts to lower angles with increased heat treatment temperature (**Figure 2.12-17a** and **Table 2.2**). Most samples show characteristic Type IV adsorption isotherms indicating the existence of a mesoporous structure (**Figure 2.12-17c**). The obtained pore size distributions for these materials are given in **Table 2.2**. Electron microscopy images suggest that the materials are in the form of crystalline nano-particle aggregates, see supplementary **Figure 2.12f** (UCT-17), **Figure 2.14e** (UCT-31), and **Figure 2.15e** (UCT-16).

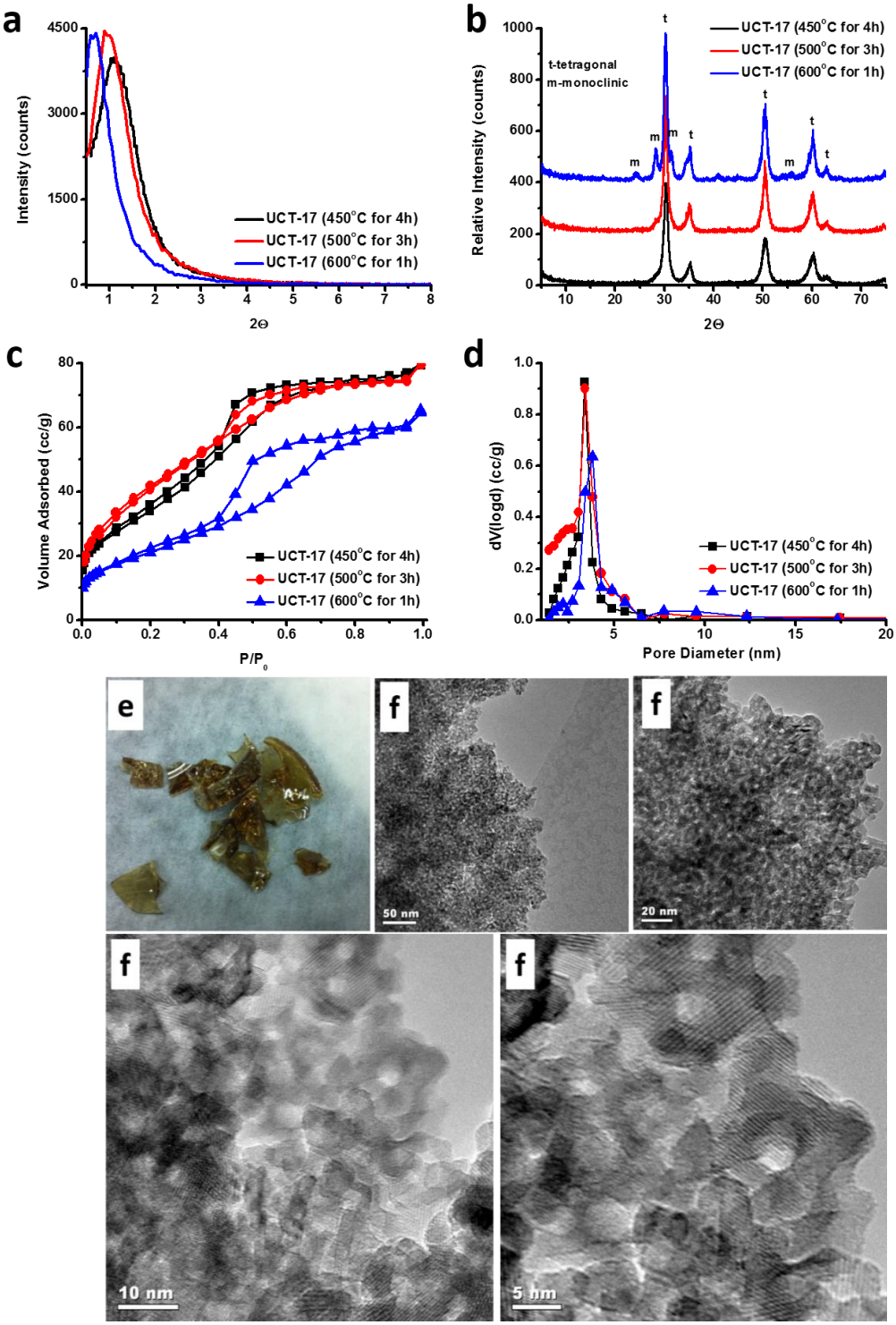

Figure 2.12 Characterization of mesoporous zirconium oxide. (a) Low and **(b)** High angle PXRD patterns **(c)** N_2 sorption isotherms and **(d)** BJH desorption pore size distributions of mesoporous zirconium oxide (UCT-17) samples calcined at different temperatures (450, 500, and 600°C). **(e)** Picture of assynthesized mesoporous zirconium oxide sample (before calcination)**. (f)** HR-TEM images of UCT-17 (600°C) sample **(**scale bar, 50, 20, 10, and 5 nm from top left to bottom right respectively**)**.

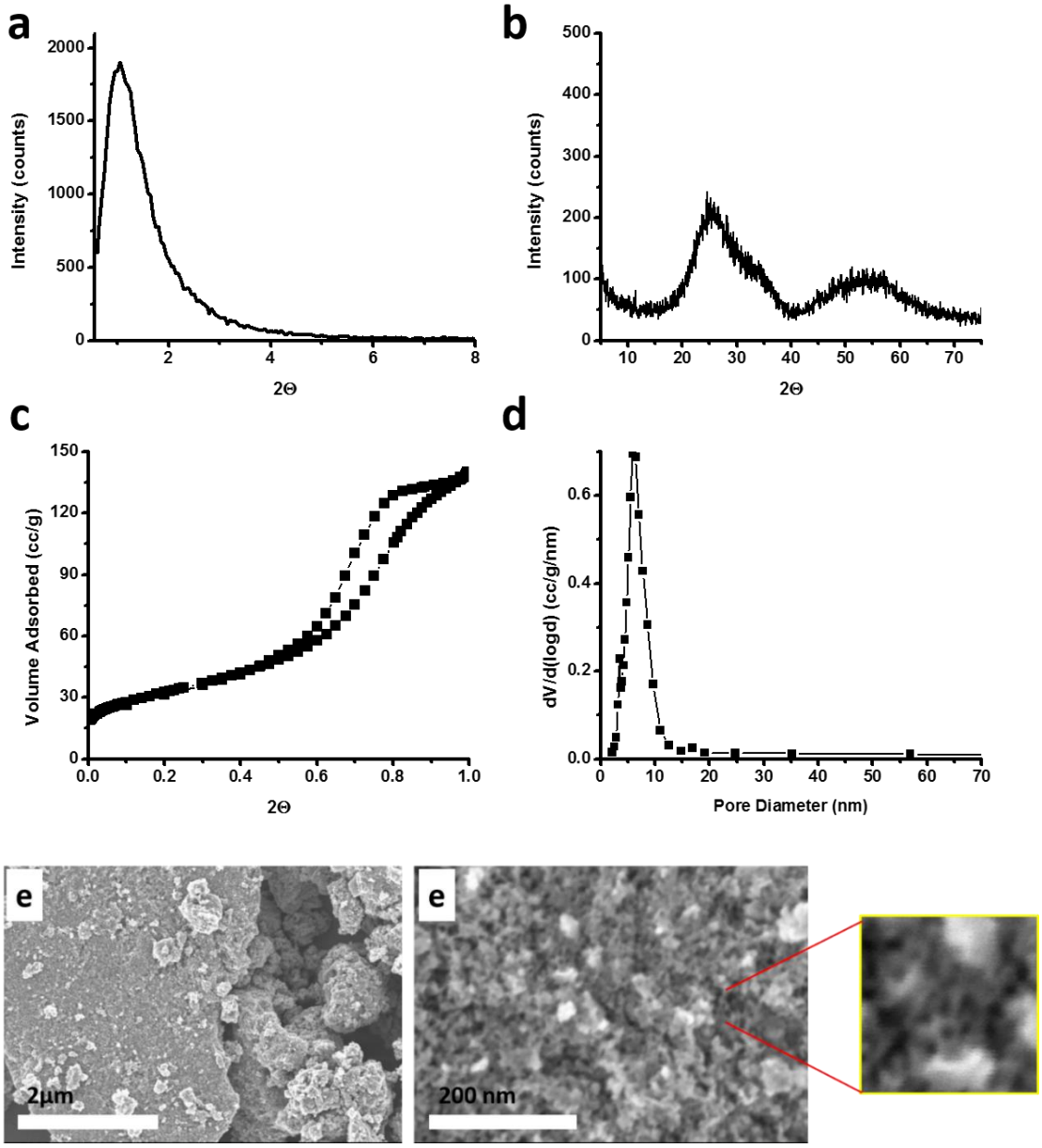

Figure 2.13 Characterization of mesoporous niobium oxide. (a) Low and **(b)** High angle PXRD patterns **(c)** N_2 sorption isotherms, **(d)** BJH desorption pore size distribution, and **(e)** FESEM images of mesoporous niobium oxide (UCT-35) sample calcined at 500ºC (scale bar, 2µm and 200 nm, from left to right respectively).

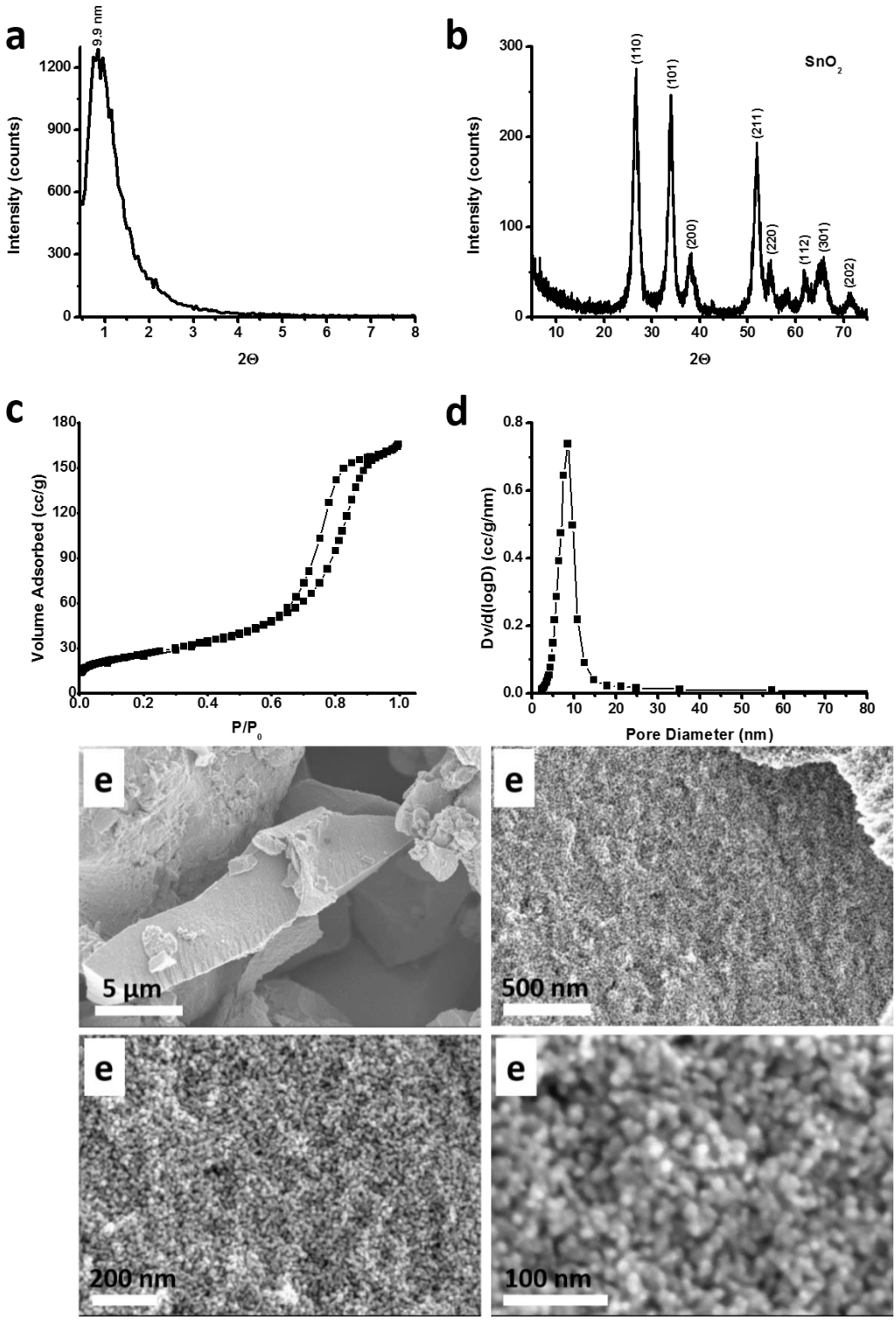

Figure 2.14 Characterization of mesoporous tin oxide. (a) Low and **(b)** High angle PXRD patterns **(c)** N_2 sorption isotherms, **(d)** BJH desorption pore size distribution, and **(e)** FESEM images of mesoporous tin oxide (UCT-31) sample calcined at 450^{o}C for 3h (scale bar, 5µm, 500 nm, 200 nm, 100 nm, from top left to bottom right respectively.

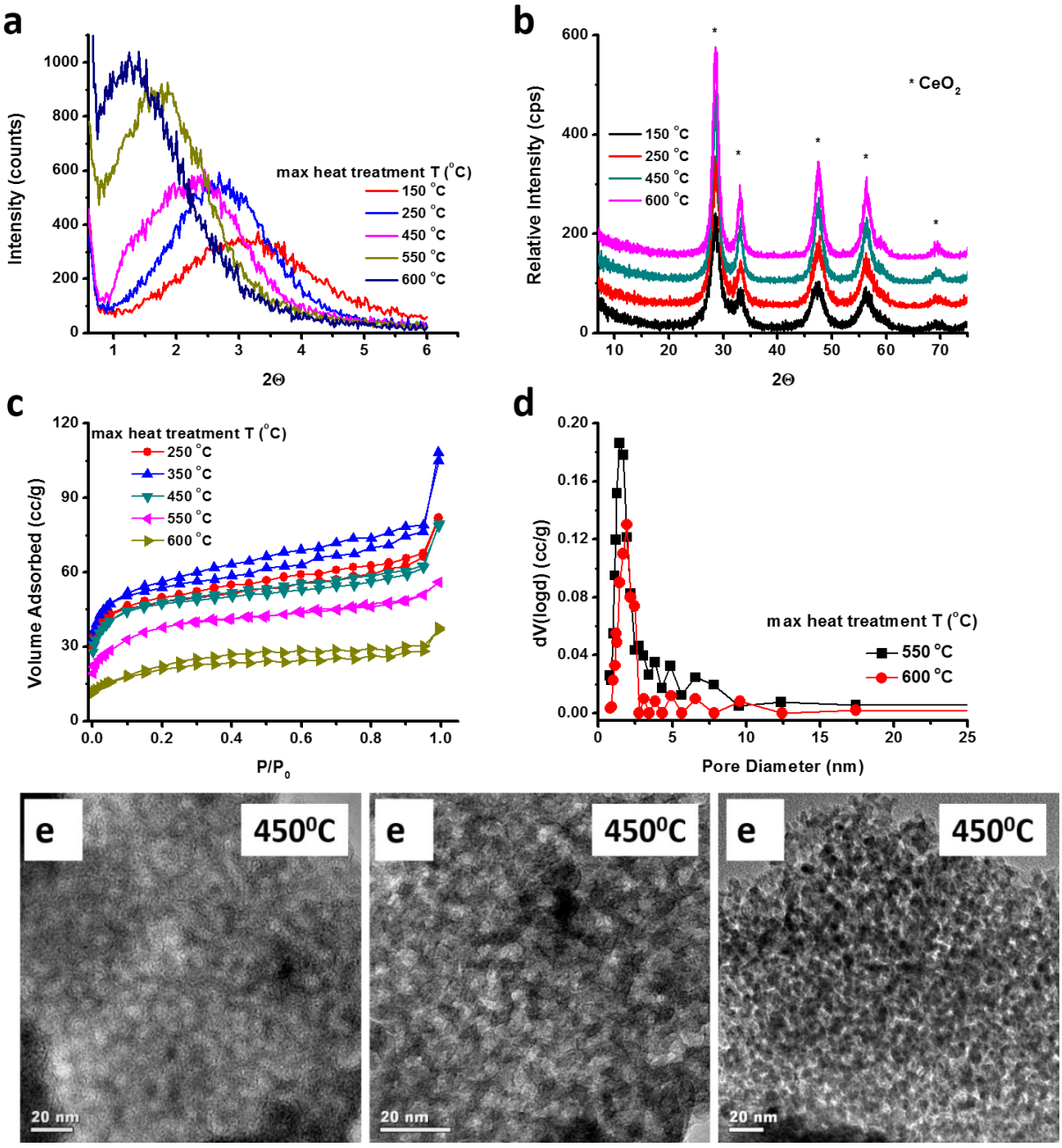

Figure 2.15 Characterization of mesoporous cerium oxide. (a) Low and **(b)** High angle PXRD patterns **(c)** N_2 sorption isotherms and **(d)** BJH desorption pore size distributions of mesoporous cerium oxide (UCT-16) samples heated at different final temperatures. **(e)** HR-TEM images of UCT-16 (450°C) sample (scale bar, 20 nm).

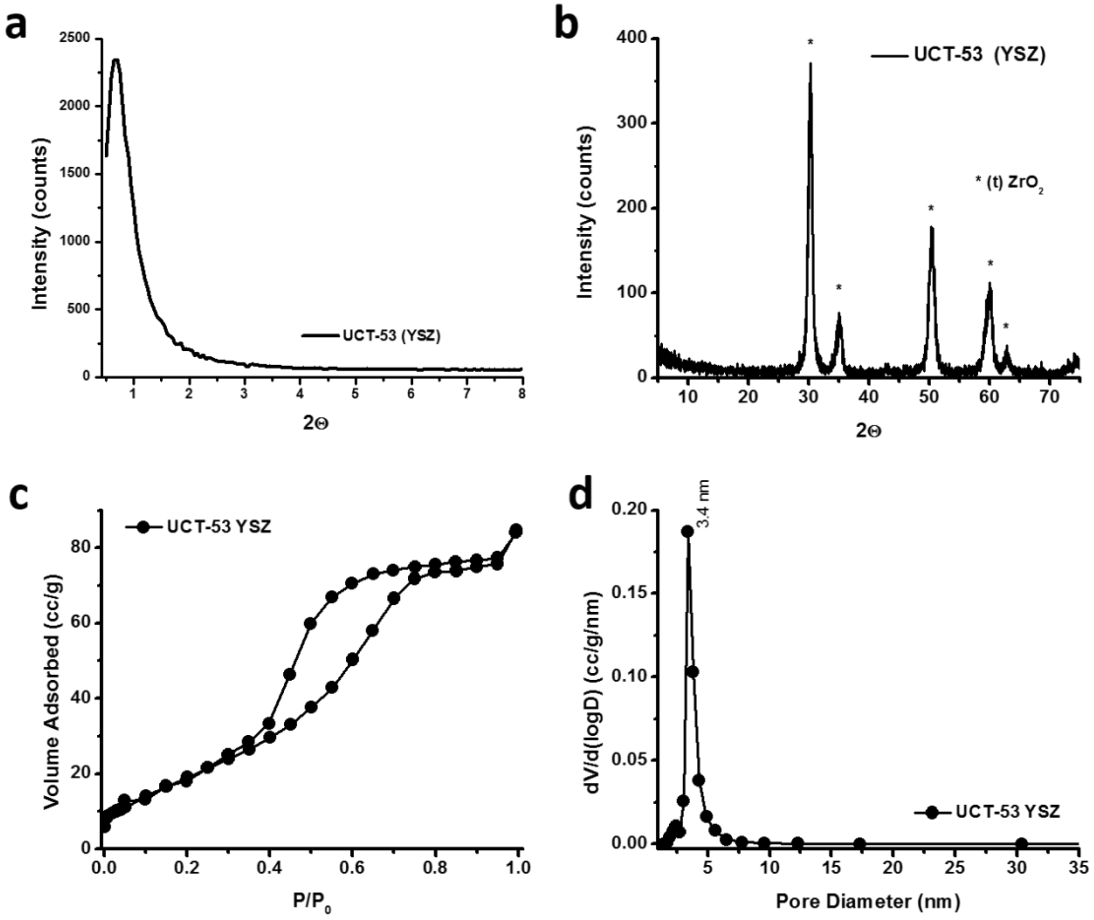

Figure 2.17 Characterization of mesoporous yttria stabilized zirconia (YSZ). (a) Low and **(b)** High angle PXRD patterns **(c)** N_2 sorption isotherm and **(d)** BJH desorption pore size distribution of mesoporous yttria stabilized zirconi (UCT-53) sample calcined at 700^{o}C.

2.3.3 Nanocasting

One of the important applications of mesoporous materials with different mesostructure and mesoporosity is their use as a hard template (nano-casting) for the synthesis of mesoporous carbon materials [27-29]. Porous carbon materials have been used in a variety of fields such as electrode materials, fuel cell electrodes, capacitors, separation, and catalysis [28, 29]. Moreover, the entire process also gives vital information about the nature of the mesoporous template [28]. For example, preserving the mesoporosity of the synthesized carbon materials by nano-casting depends on the existence of interconnecting channels in the templated porous material [28]. **Figure 2.18** shows the schematic description of the nanocasting approach along with the low angle PXRD diffractions and pore size distributions of the mesoporous silica template (UCT-14) and carbon material (UCT-33). The formed carbon materials preserve the mesoporosity and mesostructure indicating the existence of interconnecting channels in synthesized UCT mesoporous materials.

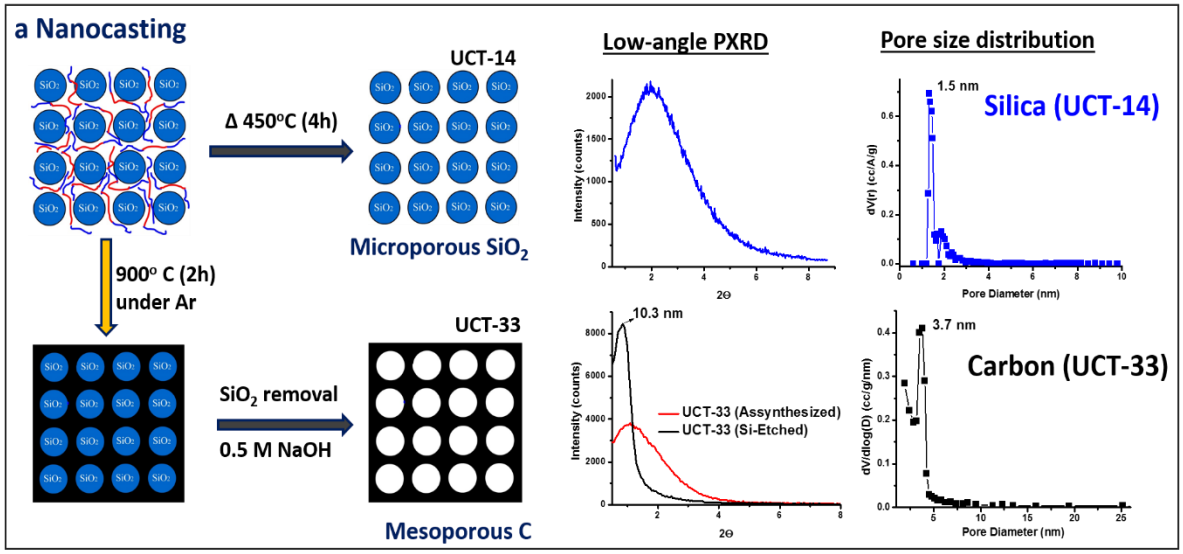

Figure 2.18 Illustration of the formation mechanism of mesoporous carbon (Meso-C) by nanocasting microporous silica (Meso-Si) along with low-angle PXRD and pore-size distribution graphs.

2.3.4 Bi-functional catalysis (oxidation of 1-decanol & esterification)

UCT materials also show excellent catalytic activities and stabilities in various reactions and Fig. 5b illustrate one of these. Mesoporous manganese oxide (UCT-1) and Cs promoted mesoporous manganese oxide (UCT-18-Cs) were used to oxidize an aliphatic alcohol (1-decanol) twice (first to 1-decanal and then to decanoic acid) and then to decanoic acid ester (decyl decanoate) by esterification reactions under mild reaction conditions (under Air reflux). The first two reactions show the oxidation power of the catalyst. Oxidation of aliphatic alcohols to carboxylic acids can only be done in the presence of strong oxidants (peroxide or molecular O_2 under high pressure) and mostly with noble metal catalysts [30, 31]. The second reaction shows the basic nature of the catalyst [30, 32]. To date such a set of reactions have not been observed with TM oxide catalysts and with these mild conditions (air as oxidant, and under ambient pressure). **Table 3.3** shows the conversions and selectivities to three products. The mesoporous manganese oxide (UCT-1) shows a relatively high conversion (as

high as 22%) and selectivity towards 1-decanal (100%), however its non-porous counterpart (commercial Mn_2O_3) shows no activity for 1-decanol oxidation. When compared to ion promoted state of art manganese oxides catalysts (OMS-2 and amorphous manganese oxide), UCT-1 still is more active for 1-decanol oxidation (**Figure 2.19**). Ion (Cs) promoted mesoporous manganese oxide (UCT-18-Cs) showed the best activity among the catalysts tested and conversion reached 53% with a decyl decanoate selectivity of 23 % (and 76 % decanoic acid). The other ion promoted manganese oxide catalysts (OMS-2 and amorphous manganese oxide) can only do a one step oxidation to aldehyde however UCT-18-Cs can oxidize 1-decanol first to 1-decanal and then to decanoic acid. Then, decanoic acid converts to decyl decanoate by esterification reactions between decanoic acid and 1-decanol.

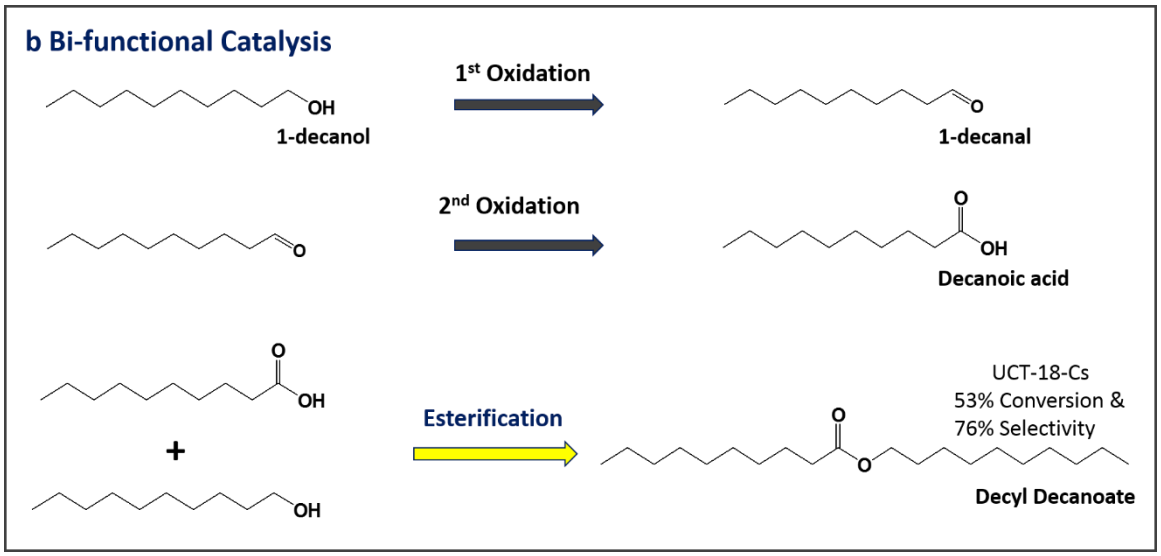

Figure 2.19 Reaction pathway of double oxidation of 1-decanol to decanoic acid, and then followed by an esterification reaction between 1-decanol and in-situ-formed decanoic acid to form decyl decanoate with mesoporous manganese oxide samples (Meso-Mn-250 and Meso-Cs[Mn-250]), OMS-2, amorphous manganese oxide and commercial Mn_2O_3.

Table 2.3 1-decanol conversion and selectivity for double oxidation and esterification reaction.

Catalyst	Conversion (%)	Selectivity (%)		
		1-Decanal	Decanoic Acid	Decyl Decanoate
UCT-18-Cs	53	1	76	23
UCT-1	22	100	-	-
K-OMS-2	10	100	-	-
Amorphous Manganese Oxide	19	100	-	-
Commercial Mn_2O_3	0	-	-	-

2.4 Discussion

2.4.1 Control of Thermodynamic Parameters

The hypothesis is that careful control of the reaction medium and reagents allows preparation of well-ordered crystalline transition metal oxide materials that are markedly different from the traditional silica based synthetic routes and original mechanisms ($(S^+,I^-$; S^-I^+; $S^+X^-I^+$; $S^-X^+I^-$) proposed in the literature [6-9]. Silica has limited structures under normal mesoporous synthetic conditions whereas transition metal oxides are well known to have multiple structures in the temperature range of 25ºC to 800ºC [10]. There should be other general synthetic mechanisms to prepare mesoporous transition metal oxide materials than traditional routes. In these syntheses, the effect of key thermodynamic parameters ΔG_{inter} (everything is in the micelle) and ΔG_{sol} (no solvent effects in the inverse micelle) are minimized. In addition, ΔG_I is controlled by carrying out the entire reaction in inverse micelles and unique NOx chemistry and ΔG_{org} is adjusted with NO_3^- and 1-butanol. The materials synthesized with the approach results in mesoporous materials that have markedly different structural properties than the materials prepared by traditional approaches. According to our model the low-angle peak position correspond to the average sizes of the building blocks (nano particles) and the mesopores are formed by connected intra particle voids. Therefore, unit cell expansion during heat treatment means an increase in nano particle size (probably, nano particles sinter to form bigger ones) so as the size of intra particle voids (mesopores). We are not aware of this phenomenon previously being observed for reported mesoporous materials. Unlike UCT materials, mesopores contract upon heat treatment (calcination) in conventional mesoporous materials due to further condensation of mesopore walls. The exact position of the low-angle peak depends on the heating temperature and time and material being studied.

2.4.2 The Formation Mechanism of Mesoporous Materials

A proposed formation mechanism of the ordered mesopores is shown in **Figure 2.20** First, metal precursor loaded inverse micelles are packed on solvent removal; packing is followed by oxidation and condensation of the metal precursors in the micelles. Finally, the surfactants are washed off and surface NO_x and carboxyl species are removed at 150^{o}C for 12 h followed by a second heating step at 250^{o}C for 1-4 h. Mesopores merge to form larger ordered mesoporous materials during the heating cycles. The crystalline walls are made up of nanoparticles of metal oxides that order as observed by PXRD, HR-TEM, and electron diffraction (ED) methods. Meso-order (low angle PXRD) and mesoporosity (Type IV adsorption isotherms) are both formed by packing of nano oxide particles. The mesopores are the intra-connecting voids formed in between randomly packed nano-crystals. Formation of microporosity and mesoporosity by aggregation of colloidal nano particles or using these materials for nano-casting has previously been observed [26].

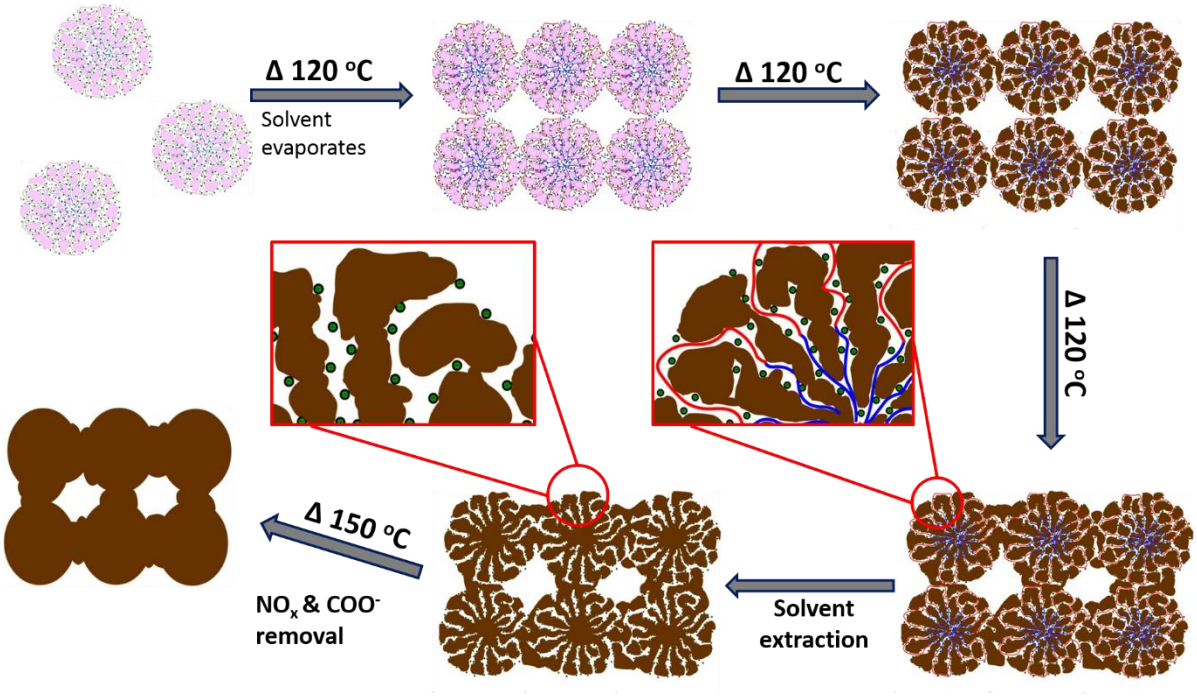

Figure 2.20 Proposed formation mechanism of inverse micelle-templated mesoporous materials. Formed inverse micelles are packed and then inorganic component is condensed and oxidized. Surfactants are removed by ethanol washing (solvent extraction) and adsorbed species (NOx and COO_) are removed by a heat treatment at 150 _C (12 h).

2.5 Conclusion

In summary, a novel approach for the synthesis of mesoporous metal oxides has been introduced first time. The approach allow one to synthesize mesoporous materials from different parts of the periodic table. There are several advantages of the approach over traditional methods which are: H is not a concern, in principle the method is applicable to all TMs, gel aging is not required, various crystal structures can be formed, thickness of walls can be controlled (by controlling the size of nano particles), and this is the first time pore expansion on heat treatment of MTMO materials has been observed. Over 60 new University of Connecticut (UCT) mesoporous materials with tunable porosity and crystallinity have been synthesized with the current approach. These UCT mesoporous materials have unique stability, structural, and porous properties that can readily be tailored for different applications.

2.6 References

1. Kresge, C. T., Leonowicz, M. E., Roth, W. J., Vartuli, J. C., Beck, J. S. *Nature* **359,** 710-712 (1992).
2. Hoffmann, F., Cornelius, M., Morell, J., Fröba, M. *Angew. Chem. Int. Ed.* **45,** 3216-3251 (2006).
3. Zhao, D., Huo, Q., Melosh, N., Fredrickson, G. H., Chmelka, B. F., Stucky, G. D. *Science* **279,** 548-552 (1998).
4. Ryoo, R., Joo, S. H., Kruk, M., Jaroniec, M. *Adv. Mater.* **13,** 677-681 (2001).
5. Tian, B., Liu, X., Tu, B., Yu, C., Fan, J., Wang, L., Xie, S., Stucky, G. D., Zhao, D. *Nature Materials* **2,** 159-163 (2003).
6. Boettcher, S. W., Fan, J., Tsung, C., Shi, Q., Stucky, G. D. *Acc. Chem. Res.* **40,** 784-792 (2007).
7. Schüth, F. *Chem. Mater.* **13,** 3184-3195 (2001).
8. Lee, J., Orilall, M. C., Warren, S. C., Kamperman, M., DiSalvo, F. J., Wiesner, U. *Nature Materials* **7,** 222-228 (2008).
9. Banerjee, S., Santhanam, A., Dhathathreyan, A., Rao, P. M. *Langmuir* **19,** 5522-5525 (2003).
10. Suib, S. L. et al., *Science* **276,** 926-930 (1997).
11. Jiao, F., Bruce, P. G. T. *Angew. Chem. Int. Ed.* **43,** 5958-5961 (2004).
12. Sinha, A. K., Suzuki, K. *Angew. Chem. Int. Ed.* **44,** 271-273 (2005).
13. Brezesinski, T., Wang, J., Tolbert, S. H., Dunn, B. *Nature Materials* **9,** 146-151 (2010).

14. Sadakane, M., Ueda, W. *Ordered Porous Crystalline Transition Metal Oxides, in Porous Materials*, Bruce, D. W., O'Hare, D., Walton, R. I. Eds. (Wiley, Chichester, UK, 2010), pp. 147-215.

15. Antonelli, D. M., Ying, J. Y. *Chem. Mater.* **8**, 874-881 (1996).

16. Vettraino, M., Trudeau, M. L., Antonelli, D. M. *Adv. Mater.* **12**, 337-341 (2000).

17. Soler-Illia, G. J. A. A., Crepaldi, E. L., Grosso, D., Sanchez, C. *Curr. Opin. Colloid Interface Sci.* **8,** 109-126 (2003).

18. Soler-Illia, G. J. A. A., Sanchez, C. *New J. Chem.* **24,** 493-499 (2000).

19. Grosso, D., Cagno, F., Soler-Illia, G. J. A. A., Crepaldi, E. L., Amenitsch, H., Brunet-Bruneau, A., Bourgeois, A. Sanchez, C. *Adv. Funct. Mater.* **14,** 309-322 (2004).

20. Huo, Q., Margolese, D. I., Ciesla, U., Demuth, D. G., Feng, P., Gier, T. E., Sieger, P., Firouzi, A., Chmelka, B. F., Schüth, F., Stucky, G. D. *Chem. Mater.* **6,** 1176-1191 (1994).

21. Poyraz, A. S., Dag, O. *J. Phys. Chem. C* **113,** 18596-18607 (2009).

22. Garin, F. *Appl. Catal., A* **222,** 183-219 (2001).

23. Mudiyanselage, K., Weaver, J. F., Szanyi, J. *J. Phys. Chem. C* **115,** 5903-5909 (2011).

24. Dag, O., Alayoglu, S., Uysal, I. *J. Phys. Chem. B* **108,** 8439-8446 (2004).

25. Lee, J., Orilall, M. C., Warren, S. C., Kamperman, M., Disalvo, F. J., Wiesner, U. *Nature Materials* **7,** 222-228 (2008).

26. Fan, W., Snyder, M. A., Kumar, S., Lee, P., Yoo, W. C., McCormick, A. V., Penn, R. L., Stein, A., Tsapatsis, M. *Nature Materials* **7,** 984-991 (2008).

27. Ryoo, R., Joo, S. H., Kruk, M., Jaroniec, M. *Adv. Mater.* **13,** 677-681 (2001).

28. Liang, C., Li, Z., Dai, S. *Angew. Chem. Int. Ed.* **47,** 3696-3717 (2008).

29. Lee, J., Joo, S. H., Ryoo, R. *J. Am. Chem. Soc.* **7,** 1156-1157 (2002).

30. Ishida, T., Ogihara, Y., Oshashi, H., Akita, T., Honma, T., Oji, H., Haruta, M. *Chemsuschem* **5**, 2243-2248 (2012).

31. Mallat, T. Baiker, A. *Chem. Rev.* **104**, 3037-3058 (2004).

32. López, D. E., Goodwin Jr., J. G., Bruce, D. A., Lotero, E. *Applied Catalysis A: General* **295**, 97-105 (2005).

33. DeGuzman, R. N., Shen, Y., Neth, E. J., Suib, S. L., O'Young, C., Levine, S., Newsam, J. M. *Chem. Mater.* **6**, 815-821 (1994)

34. Iyer, A., Del-Pillar, J., King'ondu, C. K., Kisse, I. E., Garces, H. F., Huang, H., El-Sawy, A. M., Dutta, P. K., Suib, S. L. *J. Phys. Chem. C.* **116**, 6474-6483 (2012).

Chapter 3: Tungsten Promoted Mesoporous Group 4 (Ti, Zr, & Hf) Transition Metal Oxides for Room Temperature, Solvent Free Acetalization and Ketalization Reactions

3.1 Introduction

High surface area, open framework materials with tunable and monomodal mesoporosity are known to be very promising in catalysis. They have been shown to perform better than their non-porous counterparts as heterogeneous catalysts in many reactions due to their nano-crystalline nature, high surface area and pore volume[1–6]. More specifically, their use as solid acid catalysts has recently attracted significant attention due to potential use in industrial biomass conversion, biodiesel production, and value added platform chemical synthesis from renewable resources[7–12]. Current homogeneous mineral acids (i.e. H_2SO_4, HCl, $TiCl_4$) have known corrosion, recycling, and separation problems. Therefore, an environmentally friendly heterogeneous acid catalyst design is a prospective emerging field[13,14]. The designed mesoporous solid acid catalysts are desired for their structural stability and tunable acidic parameters such as number, type (Brønsted or Lewis), and strength of acid sites[7,8,14–16].

The generic approach for the design is promoting and forming acid sites on the internal mesopore surface by either creating a charge imbalance in the structure or grafting acidic groups on the internal mesopore surface[5,6,14–18]. The promoter can be an organic group such as carboxyl, sulfate, and phosphate or an inorganic atom as dopant or an oxide cluster planted on the surface such as oxides of tungsten, aluminum, and tin [7,14–16,18–22]. The acid sites are either the electron deficient metal centers (Lewis acid sites) or the hydroxyl groups attached to the metal center (Bronsted acid sites). The most studied and promising oxides for the

synthesis of mesoporous solid acid catalysts are those based on silicon, titanium, zirconium, or tin.

Acetalization of aldehydes to acetals and ketalization of ketones to ketals from alcohols or diols are two important acid catalyzed reactions. These reactions are widely used in organic chemistry for protecting carbonyl groups, since formed acetals and ketals show high stability under basic conditions, Grignard reagents, metal hydrides, oxidants, bromination, and esterification[23]. Ketals and acetals are also used in the fragrance, cosmetics, food, and beverage industries [24–27]. These reactions are generally performed by homogeneous mineral acids such as HCl, H_3PO_4, and H_2SO_4[28]. In addition, the reactions are predicted to have potential use in the synthesis of glycerol based direct fuel additives[29–32]. Since glycerol is a side product of biodiesel production, this material should be available in large amounts in the near future. Therefore, there is a growing interest in the use of glycerol in acetalization reactions to produce value added chemicals and fuel additives [29–32]. Various heterogeneous acid catalysts have been tested for these reactions and they have shown good activities under water free conditions, some of which are bismuth subnitrate, functionalized mesoporous silica, zeolites, aluminum triflate, promoted oxides (i.e. sulfate, tungsten, molybdenum), ionic liquids, and metal (IV) phosphates [17,22,25–27,29–36].

In this chapter of the thesis we discuss synthesis of novel tungsten promoted mesoporous titania, hafnia, and zirconia catalysts and their catalytic performance in solvent free, room temperature (RT) acetalization and ketalization reactions. These mesoporous catalysts are members of the recently discovered University of Connecticut (UCT) mesoporous materials family[37]. Syntheses of mesoporous tungsten promoted titania (UCT-

55), zirconia (UCT-50), and hafnia (UCT-56) and their catalytic performances are discussed for the first time in this thesis.

3.2 Experimental Section

3.2.1 Chemicals

Titanium (IV) Isopropoxide (97+ %) was purchased from Alfa Aesar. Benazaldehyde (98 %) was purchased from Baker and Adamson. Ammonium Metatungstate Hydrate (≥99.0 %) and Acetophenone (≥ 99.0 %) were purchased from Fluka. Methyl Alcohol Anhydrous (98.8 %) was purchased from Acros. Phenylacetaldehyde (≥ 90 %) and Phenylacetaldehyde Dimethyl Acetal (98+ %) were purchased from SACF. Zirconium (IV) Butoxide (80% wt in 1-butanol), Hafnium (IV) Chloride (98 %), Poly (ethylene glycol)- block- Poly(propylene glycol)-block-Poly(ethylene glycol) PEO_{20}-PPO_{70}-PEO_{20} (Pluronic P123), Cyclohexanone (≥ 99.5 %), (1,1-Dimethoxy-ethyl) Benzene (97 %), Benzaldehyde Dimethyl Acetal (99 %), Cyclohexanone Dimethyl Ketal (99 %), Nitric acid (70 %), and Trans-Cinnamonaldehyde (≥ 99 %) were purchased from Sigma-Aldrich.

3.2.2 Materials Synthesis

Tungsten promoted University of Connecticut (UCT) mesoporous materials were synthesized by the following procedure: 0.02 mol of the transition metal source (0.01 mol for $HfCl_4$) was dissolved in 14 g (0.19 mol) of n-butanol. To this solution 2.5 g ($4.3x10^{-4}$ mol) of Pluronic P123 and 2.5 g of Nitric acid were added and stirred at room temperature to obtain a transparent gel (in a 150 mL beaker). For the titania system, nitric acid was diluted first in n-butanol (3-5 mL) before being adding to the gel. In another container, ammonium metatungstate solution was prepared by dissolving a certain amount of metatungstate salt in a

2.5 g ethanol+ 2.5 g (DDI) water solution (3 g +3 g for W loadings higher than 10%) to form a clear solution. The tungsten amounts are 0, 5, 10, 20, and 30 mol % (W mol amount with respect to TM, $mol_W/mol_{TM}*100$). The formed solution was then added to the above-mentioned transparent gels under vigorous magnetic stirring at RT. Upon addition of tungsten solution, the gels immediately turned opaque and became viscous. The formed opaque gel was further stirred for another 30 min and then placed in an oven running at 120 ^{0}C for 5-6 h. The obtained white material was calcined in an oven at 600^{0}C for 1 h with a heating rate of 2^{0}C/min. The formed brittle material was ground and labeled as **X%W-Y**, where X is 5, 10, 20, or 30 depending on the percent of tungsten loaded and Y is Ti, Zr, or Hf depending on the TM used. In addition, well known solid acid sulfated-zirconia (**S-Zr**) and sulfated-titania (**S-Ti**) catalysts were synthesized following the procedure of Corma et al[19].

3.2.3 Materials Characterization

Low-angle and wide-angle Powder X-Ray diffraction (PXRD) analyses were performed on a Rigaku Ultima IV diffractometer (Cu Kα radiation, λ=1.5406 A) with an operating voltage of 40 kV and a current of 44 mA. N_2 sorption experiments were conducted on a Quantachrome Autosorb-1-1C automated adsorption system. The powders were degassed for 4 h at 250^{o}C prior to measurement. High-resolution transmission electron microscopy (HRTEM) images of the mesoporous materials were recorded on a JEOL 2010 FasTEM microscope equipped with an EDS detector operating at 200 kV. X-ray photoelectron spectroscopy (XPS) studies were performed on a PHI model 590 spectrometer using Al Kα (λ=1486.6eV) radiation operating with an accelerating voltage of 12.5 kV. The powder samples were pressed onto a carbon tape and mounted on a sample rod. Charging effects were corrected by adjusting the binding energy of C 1s to 284.6 eV. Pyridine adsorption studies

were performed with 13 mm diameter self-supporting pellets. The powders were hydrated overnight prior to pellet preparation. The pellets were cleaned in a tubular furnace at 250 ^{0}C for 2 h under dry air flow. 1 M pyridine solution in methanol was dropped on pellets and physisorbed pyridine was removed in a tubular furnace running at 200 ^{0}C for 90 min under dry air flow. FTIR spectra of the pellets were collected using a Thermoscientific Nicolet 8700 spectrometer equipped with an MCT/A detector. Sixty four scans were collected with a 4 cm^{-1} spectral resolution in the absorbance mode. The number of Brønsted acid sites was determined via a titration experiment, which involved ion-exchange between H^{+} and Na^{+} followed by titration to pH 7 with an NaOH solution [38]. Raman spectra of powder samples were collected with a Thermoscientific NXR FT-Raman Module with a semiconductor laser operating at 976 nm (1.002 W) and equipped with an InGAs detector.

3.2.4 Catalytic Activity Measurements

The catalytic activity of the tungsten promoted solid acids was tested for acetalization (of aldehydes) and ketalization (of ketones) with methanol. All reactions were performed under solvent free conditions and in the dark. Reactants, catalysts and a magnetic stirring bar were put in a sealed vial. Then, the vial was placed in the reactor. The temperature of the reactor was measured with a thermometer placed in oil with the vial also being covered in oil to ensure the homogeneous temperature distribution throughout the reaction. In a typical reaction procedure, 5 mL (0.123 mol) of anhydrous methanol, 0.05-0.1 mmol substrate (aldehyde or ketone), and 25 mg of catalyst were put in a glass vial. The vial was then placed into the reaction setup and stirred throughout the reaction. The products were confirmed with a GC (HP 5890 series II) equipped with a DB-17MS capillary column (20.0 m x 180 µm x 0.18 µm) and mass selective detector (5971 series). For the quantitative analysis (yield and

conversion) an HP 5890 series II GC system equipped with a MTX-biodiesel TG w/Integra-Gap capillary column (14.0 m x 530 µm x 0.16 µm) and FID detector was used.

3.3 Results

3.3.1 Physicochemical properties of 10% Tungsten promoted mesoporous group 4 metal oxides:

Tungsten promoted oxides are well known active, green, and strong acid catalysts[38–43]. The acidic power originates from well dispersed nano-WOx clusters[7,41–43]. In short, the nano-WOx clusters pull the electron density from the support and create electron deficient Lewis sites (on the M^{4+} center) and hydroxyl groups on the support behave as Brønsted acid sites. Tungsten promoted solid acids are generally prepared by co-precipitation or impregnation on oxides or hydroxides [7,18,40–44]. The maximum catalytic activity is generally obtained after a high temperature heat treatment (600- 800^{o}C). Since traditional mesoporous materials generally do not have high thermal stabilities, the synthesis of mesoporous solid acids with thermally stable mesoporosity has been a challenge until now. Recently discovered University of Connecticut (UCT) mesoporous materials have overcome this problem and one can synthesize thermally stable regular mesoporous mixed oxides with a simple one step synthesis[37]. UCT materials are formed by the packing of monodispersed nano-particles in a random fashion. The formed mesopores are a network of connected intraparticle voids. Therefore, a typical UCT material can be characterized by one low-angle PXRD diffraction indicating the size of the building blocks (nano-particles) and a Type IV adsorption isotherm indicating a regular mesoporous structure.

Figure 3.1A shows the low angle PXRD patterns of 10%W promoted mesoporous Ti, Zr, and Hf samples. All samples show a characteristic one low angle diffraction line indicating a regular mesostructure. The positions of the low-angle diffraction lines are given in **Table 3.1** (column L), the peak position is 12.6 nm for both 10%W-Ti and 10%W-Zr; and 10.3 nm

for 10%W-Hf. The wide-angle PXRD patterns of these samples show no tungsten related diffraction lines suggesting a well dispersed, nano-crystalline nature of the formed tungsten oxide clusters (WOx) (**Figure 3.2**). The crystal structures of the supports (group 4 TMs) are given in **Table 3.1**; titania has anatase, zirconia has a mixture of monoclinic (m) and tetragonal (t), and hafnia has monoclinic phases. The diffraction lines of the TM supports are broad and have low intensities suggesting that the TM supports have nano-crystalline domains. Calculated Scherrer crystallite sizes are very small which correlate with the nano-crystalline nature of these materials (**Table 3.1**). All samples also have a Type IV N_2 adsorption isotherm along with a Type I hysteresis loop indicating a regular cylindrical mesoporous structure (**Figure 3.1B**). BJH desorption pore size distributions are 5.6 nm for the 10%W-Ti & 10%W-Zr and 3.8 nm for the 10%W-Hf sample (**Figure 3.1C** and **Table 3.1**). The 10%W-Ti sample has a bigger N_2 uptake in the 0.4-0.8 (P/P_0) region than other samples which indicates a higher mesopore volume than other tungsten promoted TMs (**Figure 3.1B**). The mesopore volume for the 10%W-Ti sample is 23 cc/g, whereas the pore volumes of the 10%W-Zr and 10%W-Hf samples are 0.15 cc/g and 0.09 cc/g respectively. The types and relative ratios of acid sites on the tungsten promoted mesoporous samples were determined by pyridine adsorption experiments, which are widely used methods for the characterization of acid sites on heterogeneous solid acid catalysts[22,30,45]. **Figure 3.1D** shows FTIR spectra of pyridine adsorbed tungsten promoted mesoporous samples at room temperature. In the figure, pyridine adsorbed on Brønsted acid sites (1536 cm^{-1} and 1640 cm^{-1}) is labeled as (B) , pyridine adsorbed on Lewis acid sites (1445 cm^{-1} and 1608 cm^{-1}) is labeled as (L) and the absorbance at 1488 cm^{-1} is assigned to pyridine on both Brønsted and Lewis acid sites (B+L) [22,30]. All tungsten promoted mesoporous materials contain both Brønsted and Lewis acid sites together,

however the 10%W-Ti sample contains relatively more Brønsted acid sites. The assumption of the change of the relative ratio of acid types is based on the fact that the extinction coefficients of pyridine adsorbed on Lewis or Brønsted acid sites are surface independent and intrinsic to pyridine[45].

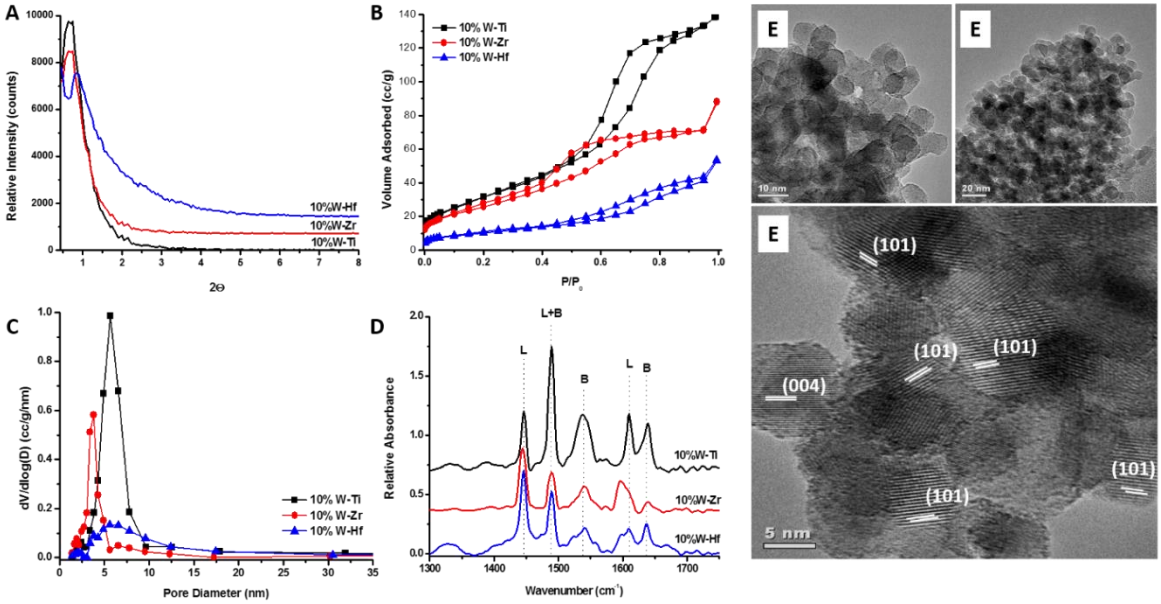

Figure 3.1 (A) Low-angle PXRD, (B) N_2 sorption isotherms, (C) BJH Desorption pore size distributions, (D) FTIR spectra of adsorbed pyridine on 10%W-Ti, 10%W-Zr, and 10%W-Hf samples (Lewis acid sites indicated by L and Brønsted acid sites indicated by B), and (E) HR-TEM images of 10%W-Ti.

Table 3.1 Surface area (S_{BET}), BJH desorption pore size distribution (P), BJH desorption pore volume (V), low-angle PXRD peak position (L), Scherrer crystallite size (D), and crystal structure of the mesoporous support.

Catalysts	S_{BET} (m^2/g)	P (nm)	V (cc/g)	L (nm)	D (nm)	Crystal Structure
Ti	77	5.9	0.17	NA	8.5	TiO_2 (Anatase)
5%W-Ti	116	6.1	0.24	12.6	6.2	TiO_2 (Anatase)
10%W-Ti	121	5.7	0.23	12.6	5.7	TiO_2 (Anatase)
20%W-Ti	118	5.7	0.24	12.6	4.4	TiO_2 (Anatase)
30%W-Ti	122	5.5	0.20	12.4	2.5	TiO_2 (Anatase)
10%W-Hf	39	5.6	0.09	10.3	1.0	HfO_2 (Monoclinic)
10%W-Zr	98	3.8	0.15	12.6	2.7	ZrO_2 (Tetragonal & Monoclinic)

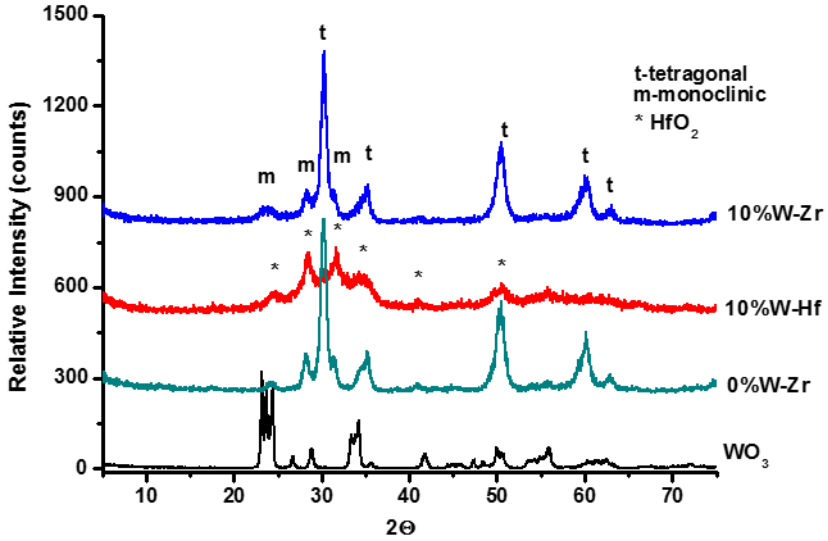

Figure 3.2 Wide-angle PXRD patterns of 0% W-Zr, 10% W-Zr, 10% W-Hf, and WO_3.

High resolution TEM (HR-TEM) images of the tungsten promoted oxides are given in **Figure 3.1E** (10%W-Ti) and **Figure 3.3** (10%W-Zr and 10%W-Hf). Low magnification images show typical characteristics of UCT materials, i.e., aggregates of monodispersed particles. High magnification images suggest a particle size around ~ 11 nm, which is very close to the positions of the low-angle PXRD diffraction lines. No crystalline tungsten oxide is observed with TEM analyses. However, EDAX mapping analyses suggest a homogeneous distribution of tungsten over the entire sample. The difficulty of imaging tungsten nano-clusters (WO_x) on zirconia supports due to a lack of contrast between the atomic tungsten species and the oxide support was discussed previously by several researchers [40,42,46]. In these studies, high-angle annular dark-field imaging (HADDF-STEM) and energy filtered TEM (EF-TEM) techniques were used for the detection of WO_x clusters [42,46]. Black spots (<1 nm) on the titania nano-particles (**Figure 3.1E**) need to be discussed. The spots are believed to be nano-WOx clusters (see section 3.2.1 Physicochemical Characterization). 10%W-Zr and 10%W-Hf do not show these types of spots and the investigated lattice fringes can be indexed to diffraction lines of the supports (**Figure 3.3**).

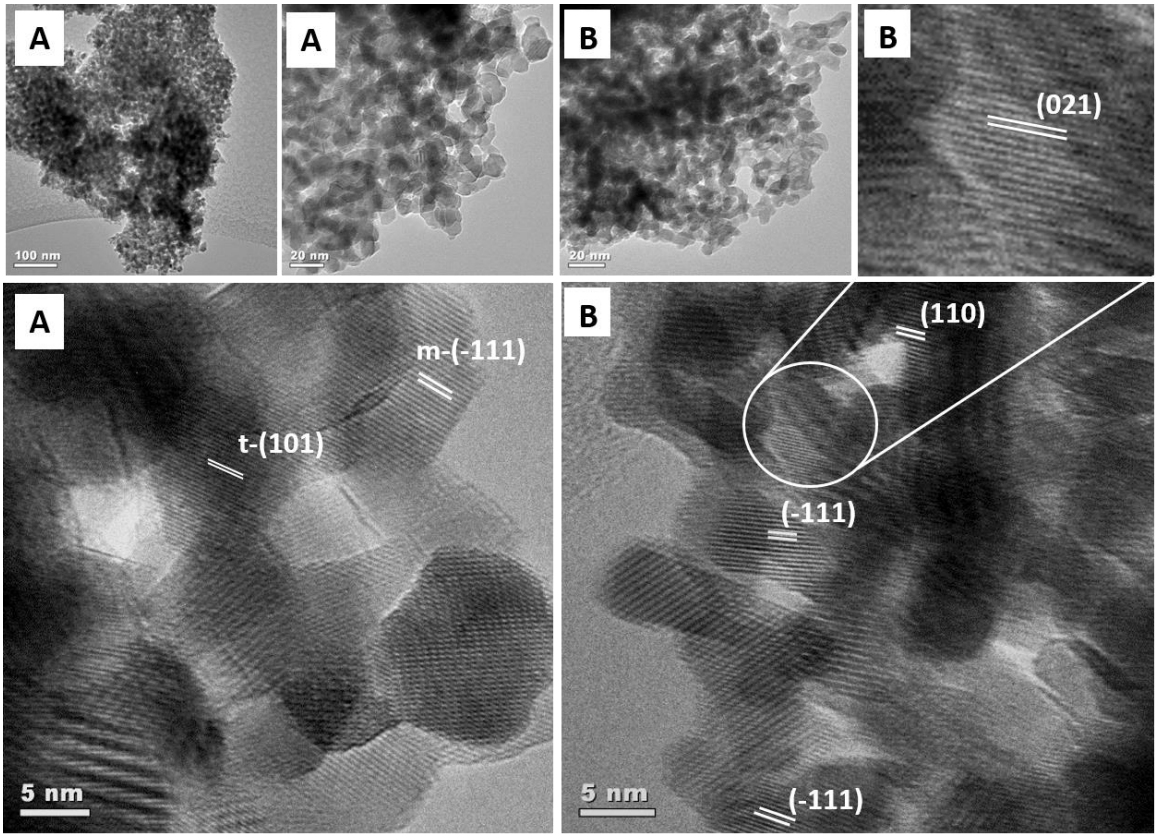

Figure 3.3 HR-TEM images of (A) 10% W-Zr (m stands for monoclinic phase and t stands for tetragonal phase) and (B) 10% W-Hf.

3.3.2 Initial catalytic results:

Initial catalytic performances of 10% tungsten promoted mesoporous group 4 TMs were evaluated for cinnamaldehyde acetalization with methanol at RT (**Figure 3.4**). Among the tungsten promoted mesoporous samples, 10%W-Ti shows the best performance with the conversion reaching as high as 92 % in as short as 15 min at room temperature. 10%W-Hf also shows a high activity and the conversion reaches 90% in 4 hours. 10%W-Zr shows relatively lower activity and the conversion barely reaches ~60 % in 8 h. All reaction mixtures were additionally analyzed by GC-MS and no other products were found other than cinnamaldehyde and cinnamaldehyde dimethyl acetal, indicating the high selectivity of tungsten promoted mesoporous samples.

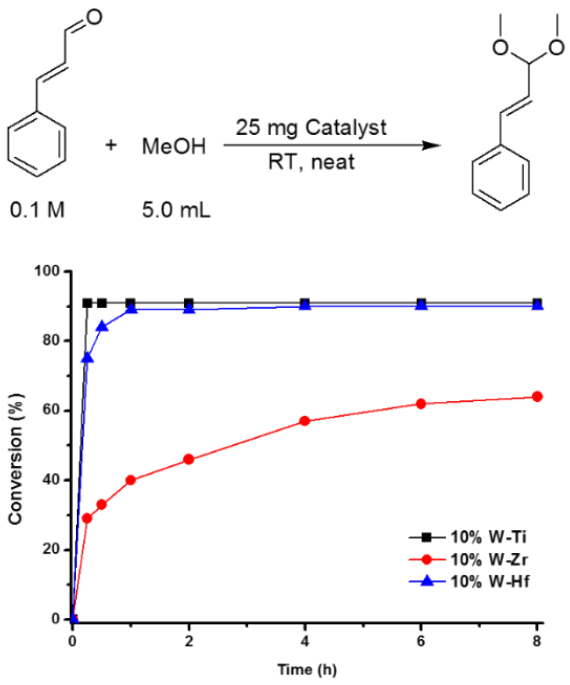

Figure 3.4 Conversions of 10%W-Ti, 10%W-Zr, and 10%W-Hf catalyzed cinnamaldehyde acetelization with methanol at RT.

3.3.3 Physicochemical Properties of Tungsten promoted mesoporous titania

Superior catalytic performance of tungsten promoted mesoporous titania (10%W-Ti) over other tungsten promoted group 4 TMs (10%W-Zr and 10%W-Hf) for acetalization of cinnamaldehyde encouraged us to focus more on the preparation of tungsten promoted titania with various tungsten loadings. Therefore, X%W-Ti samples were prepared, where X is 0, 5, 10, 20, and 30. All titania samples except the bare titania sample (0%W-Ti) show one low angle diffraction line, suggesting an ordered mesostructure (**Figure 3.5A**) with the peak position being around ~12.6 nm for all diffracting samples. In the absence of tungsten promotion (0%W-Ti), the bare titania does not preserve the mesostructure after a calcination at 600^0C. Therefore, a control experiment was conducted by calcining the 0%W-Ti sample at lower temperatures (450^0C for 4 h). The 0%W-Ti sample, calcined at 450^0C, has a low angle diffraction line of 8.8 nm and mesopore size of 3.4 nm.

The unit cell expansion with heat treatment temperature and duration are unique structural properties of UCT materials. Most likely, nano-WOx clusters prevent further sintering of titania nano-particles and preserve the mesostructure at elevated temperatures (600^oC). All tungsten promoted titania samples have the anatase crystal structure regardless of tungsten loading. However, PXRD lines get broader and lose intensity with increased tungsten loading (**Figure 3.5B**). The crystal growth hindering property of WOx clusters on titania has been reported several times in different tungsten promoted titania systems[44,47–49]. Existence of tungsten can hinder the crystal growth by either framework substitution due to almost identical ionic sizes or accumulation at grain boundaries [47,49]. The Scherrer crystallite size constantly decreases upon increasing tungsten amounts (**Table 3.1**). The crystallite size drops from 8.5

nm (0%W-Ti) to 2.5 nm (30%W-Ti). There are no distinct tungsten oxide related diffraction lines observed during PXRD analyses, however at high tungsten loadings (20% and 30% loadings) a broad peak merges as a shoulder on the anatase (101) diffraction line. The broad peak is believed to be WO_3, since tungsten oxide has its three most intense diffraction lines ((002), (020), and (200)) in this region. All tungsten promoted titania samples exhibit typical mesoporous features in N_2 sorption experiments (**Figure 3.5C**). All samples have a Type IV adsorption isotherm indicating a regular mesoporous structure, followed by a Type I hysteresis loop suggesting a regular cylindrical mesopore structure. BJH desorption pore sizes are 4.0, 6.1, 5.7, 5.7, and 5.5 nm for X%W-Ti samples with increasing X (from 0 to 30) (**Figure 3.5D** and **Table 3.1**). The pore size first increased to 6.1 nm and then gradually decreased to 5.5 nm with increased tungsten loading. Despite the bare titania sample (0%W-Ti) showing an average pore size distribution of 4.0 nm, the overall intensity (pore volume) is very low compared to the tungsten promoted samples. The low porosity of 0%W-Ti sample also yields a relatively low BET surface area (77 m^2/g) as compared to the tungsten promoted titania samples (> 116 m^2/g) (**Table 3.1**).

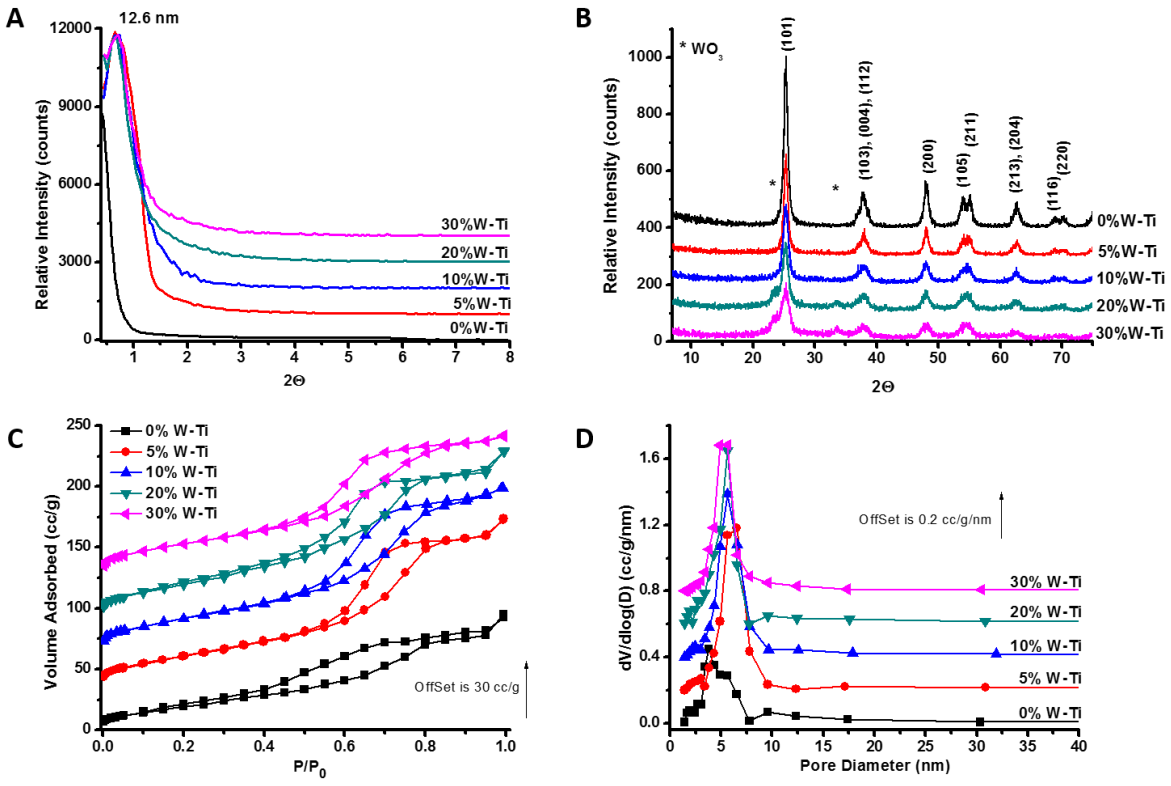

Figure 3.5 (A) Low-angle PXRD, (B) Wide-angle PXRD, (C) N_2 sorption isotherms, and (D) BJH Desorption pore size distributions of X%W-Ti samples (X= 0 , 5, 10, 20, 20), * indicates the positions of the standard diffraction lines of WO_3.

3.3.4 Spectroscopic Characterization of Tungsten promoted mesoporous titania

Vibrational spectroscopy is a vital technique for understanding the nature of tungsten oxide clusters growing on oxide materials, since tungsten can form many different structures on the template (such as polytungstate species, non-stoichiometric tungsten oxides, Td and Oh coordination, multiple oxidation states etc.) depending on the preparation method, calcination time and temperature[49–52]. All tungsten promoted mesoporous titania samples show titania related vibrations at 146, 196, 396, 516, and 638 cm^{-1}, which can be assigned to the anatase crystal phase [50,53] (**Figure 3.6A**). The anatase peaks get broader and lose intensity

with increasing tungsten loading which supports the previous argument about the crystal growth hindrance property of nano-WOx clusters on titania. Decreased intensity and peak broadening can be related to the decrease in crystallite sizes and (or) more amorphous nature of titania in tungsten promoted samples. No distinct tungsten oxide peaks are encountered during the analyses suggesting the existence of well dispersed nano-WOx clusters. However, a new peak shows up at 984 cm^{-1} and gradually becomes more intense with increasing tungsten loading. Therefore, we assigned this peak to well dispersed nano-WOx clusters sintered on titania. An absorbance band at 984 cm^{-1} for tungsten oxide was not observed, but nano tungsten clusters show absorbance bands in the 800- 1000 cm^{-1} region[42,51].

At very high tungsten loadings (20% and 30%), another absorbance peak (785 cm^{-1}) emerges adjacent to the tail of the broad anatase absorbance peaks, which is assigned to a WO_3 absorbance mode. The most intense absorbance band of WO_3 at 804 cm^{-1} shifts to lower wavenumbers by getting a contribution from the tail of the anatase absorbance band at 638 cm^{-1}. Nano tungsten oxide clusters growing on the titania or zirconia supports create Brønsted acid sites on these surfaces[48,52]. Therefore, pyridine adsorption experiments were conducted to see the changes in the relative amounts of Lewis and Brønsted acid sites by varying the tungsten loading (**Figure 3.6B**). The pure titania sample (0%W-Ti) shows only Lewis acid sites. After tungsten loading, the Brønsted acid related absorbance bands increase up to 10% tungsten loading and show only slight changes for higher tungsten loadings. The number of total Brønsted acid sites was also determined by titration experiments to confirm the increase of the number of Brønsted acid sites. As in the pyridine adsorption studies, titration experiments also show a large increase in the number of Brønsted acid sites up to 10% tungsten loading and show minor changes with higher tungsten loadings.

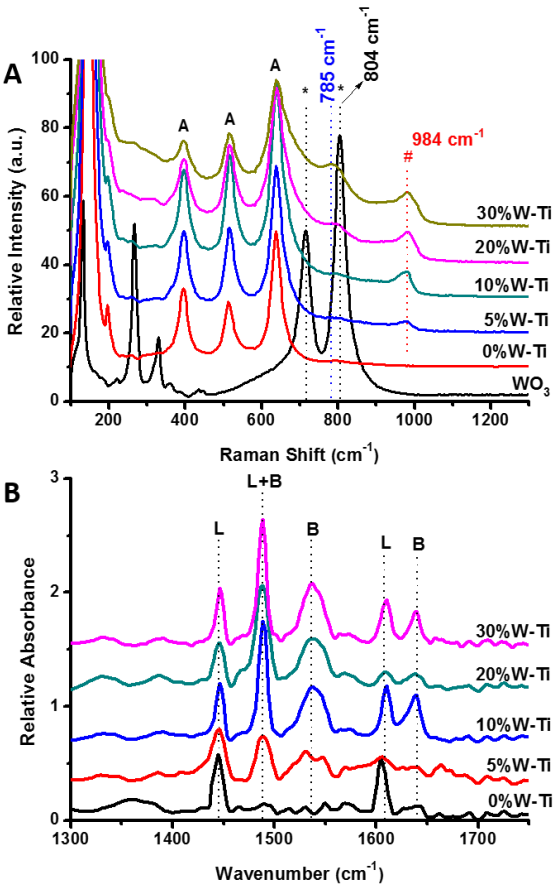

Figure 3.6 (A) Raman Spectra of X%W-Ti samples and (B) FTIR spectra of adsorbed pyridine on X%W-Ti samples (Lewis acid sites indicated by L and Brønsted acid sites indicated by B). (X= 0 , 5, 10, 20, 20).

For a deeper understanding of surface characteristics, XPS spectra were collected for tungsten promoted titania samples and tungsten oxide (WO_3) for comparison. **Figure 3.7** shows the XPS spectra of Ti 2p (**A**), O 1s (**B**), and W 4f (**C**) regions. The Ti 2p region shows a decrease in binding energy with increased tungsten loading from 0% to 10%, The Ti $2p_{3/2}$ binding energy decreases from 459.07 eV to 458.44 eV (**Table 3.2**). However, further tungsten loadings shift the Ti $2p_{3/2}$ signal first to 458.61 eV (20%W-Ti) and then to 458.67 eV (30%W-Ti) (**Table 3.2**). Furthermore, at high tungsten loadings (20% and 30%) the Ti 2p

doublet signals become broader, suggesting a different chemical environment for Ti (**Figure 3.7A**). The increase and broadening can be attributed to either a strong interaction between the tungsten clusters and the titania support or a framework replacement of Ti with W [42,44,50]. However, the replacement of Ti with W is unlikely, because replacing Ti with W creates a charge imbalance yielding formation of oxygen vacancies, so one could expect an increase of both O 1s and Ti 2p binding energies (BE) [48,50]. Nevertheless, the O 1s signal moves to lower BE upon tungsten loading (**Figure 3.7B**). The tungsten source is negatively charged metatungstate ($W_{12}O_{40}^{8-}$) anion rather than a tungsten cation and incorporation of an individual tungsten atom in the titania network is unlikely.

The O 1s signals for TiO_2 (0%W-Ti) and WO_3 are at 530.72 eV and 530.75 eV, respectively (**Table 3.2**), which are in a good agreement with literature values[54]. Tungsten promoted titania samples show broader O 1s signals and the signal gradually shifts to lower BEs (529.85 eV for 10%W-Ti) and remains mostly the same for higher tungsten loadings (**Table 3.2**). XPS signal broadening generally indicates that atoms are in more than one chemical environment [50,51,55]. The shift of the O 1s signal to a lower BE is due to an increase of electron density on O. In the O 1s binding energy scale, the 527.7- 530.5 eV region corresponds to a 2^- formal charge on O[54]. Therefore, the decrease of the O 1s BE can be attributed to the formation of Brønsted acid sites upon tungsten loading, since acidic protons (H^+) on the surface create a polarization and charge accumulation (to balance the surface charge) on the surface oxygens. **Figure 3.7C** shows the W 4f BE region, an asymmetry can be seen at low tungsten loadings due to the presence of the interfering Ti 3p signal in the same region. Therefore, the spectra were deconvoluted for better evaluation of the W 4f BE region. The overall line shape resembles WO_3 with increasing tungsten loadings which suggests an

increase of the surface concentration of tungsten. The BE of the W $4f_{7/2}$ signal is lower than WO_3 (35.84 eV) for all tungsten promoted samples. The W $4f_{7/2}$ BE decreases gradually from 35.84 eV to 35.4 eV while the tungsten loading increases from 0% to 30%. The decrease in tungsten binding energy in supported systems is generally attributed to the partial reduction of W^{6+} to W^{5+} or W-O-Ti bond formation (grafted tungsten clusters)[51,52,56]. Considering the stronger acidic character of W^{6+}, we assigned the shift to nano-WOx clusters well sintered on the titania support. However, self-reduction under high vacuum by desorbing OH^- or O_2 should not be ruled out [57,58].

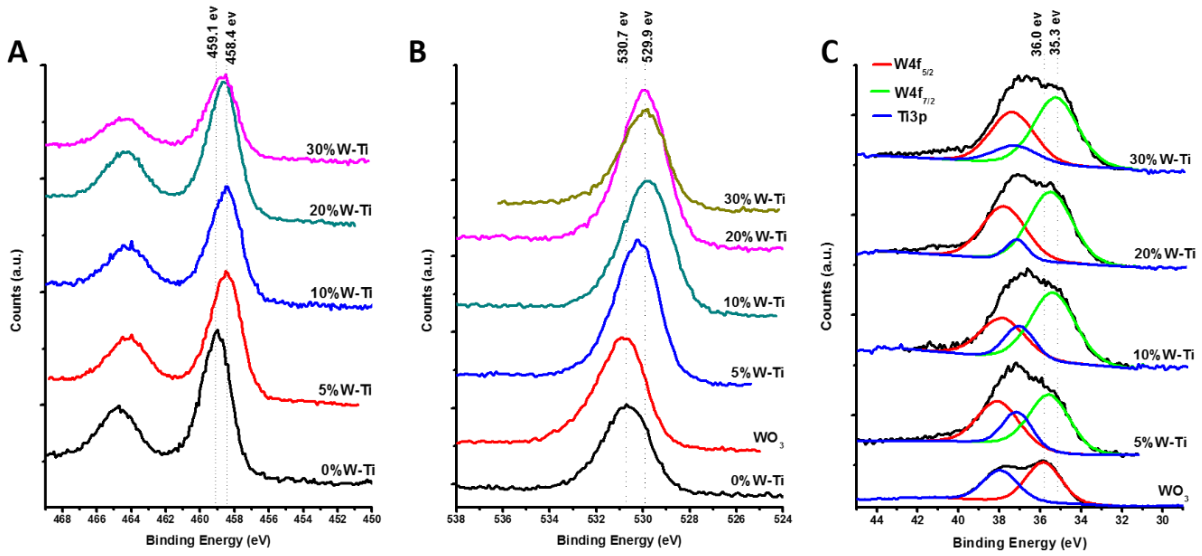

Figure 3.7 XPS spectra of (A) Ti 2p, (B) O 1s, and (C) W 4f binding energy regions for X%W-Ti samples, where X= 0, 5, 10, 20, and 30.

Table 3.2 Ti $2p_{3/2}$, O 1s, and W $4f_{7/2}$ XPS binding energies (BE) of X% W-Ti (X=0, 5, 10, 20, 30) and WO_3.

	Ti $2p_{3/2}$	O 1s	W $4f_{7/2}$
Catalyst	**BE (eV)**	**BE (eV)**	**BE (eV)**
WO_3	-	530.79	35.84
0%W-Ti	459.07	530.72	-
5%W-Ti	458.44	530.23	35.71
10%W-Ti	458.44	529.85	35.64
20%W-Ti	458.61	529.93	35.58
30%W-Ti	458.67	529.91	35.40

3.3.5 TEM Characterization of Tungsten promoted mesoporous titania

Formed WOx clusters on titania support were further investigated by HR-TEM (**Figure 3.8**). The 0%W-Ti sample consists of crystalline and micron sized particles, rather than a nano-particle aggregate (**Figure 3.8A**). The observed micron sized crystalline domains are also in good agreement with the absence of a low angle diffraction line and low porosity of the 0%W-Ti sample (**Figure 3.5A**, **B**, and **C**). HR-TEM images of tungsten promoted samples show aggregated crystalline titania nano-particles (**Figure 3.8B** to **D**). No crystalline tungsten oxide clusters are encountered throughout the analyses of all tungsten promoted samples. During the HR-TEM analyses of X%W-Ti samples, black spots have been observed on the titania support. In addition, the number and size of these black spots increase with increased tungsten loading (**Figure 3.8A** to **D**). Some of the spots are shown by a white arrow and white circles (for multiple spots in close proximity) in **Figure 3.8**.

Despite the lack of direct evidence, the black spots are believed to be nano-WOx clusters. Another observed change with increasing tungsten amount on the titania nano-particles is the observation of defects on the surface (**Figure 3.8A** to **D**). At high tungsten loadings (10-30%) the surfaces of titania nano-particles are more rough as compared to the 0%W-Ti sample which has a fairly smooth surface morphology.

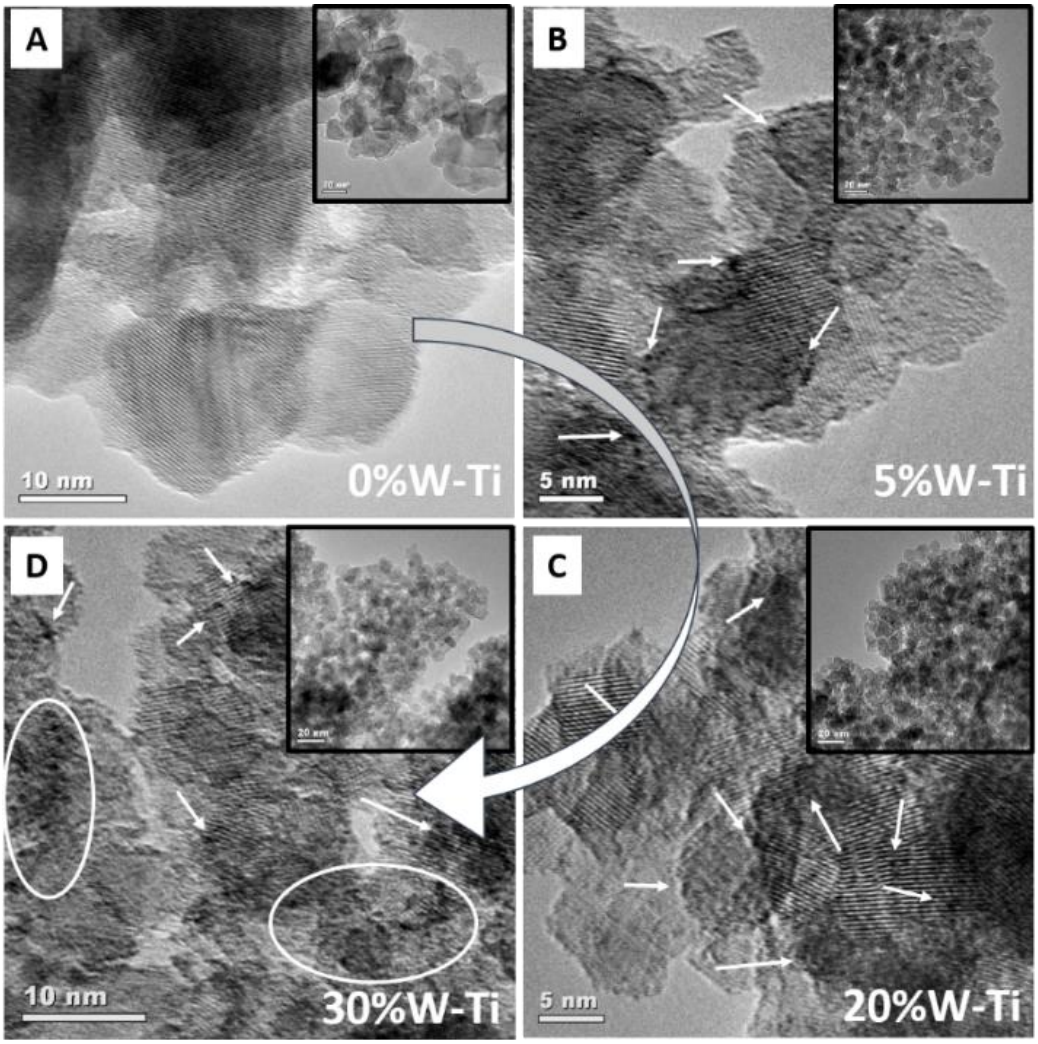

Figure 3.8 HR-TEM images of (A) 0%W-Ti, (B) 5%W-Ti, (C) 20%W-Ti, and (D) 30%W-Ti (The white curved arrow indicates the direction of increasing tungsten loading). White arrows point to some of the nano-WO_x clusters and white circles highlight the regions with high numbers of nano-WO_x clusters.

3.3.6 Catalytic Studies:

3.3.6.1 Acetalization and Ketalization with tungsten promoted mesoporous oxides

Acetalization and ketalization of several aldehydes and ketones with MeOH at room temperature (RT) were conducted by the tungsten promoted mesoporous oxides (**Table 3.3**). Acetalization is known to be easier than ketalization due to double hydrogen bonding activation[25,59]. Therefore, all tungsten promoted samples were first tested for acetalization of aldehydes. All tungsten promoted mesoporous oxides show very high activity for acetalization of benzaldehyde (**Table 3.3**, entry 1). The conversion of benzaldehyde reaches as high as 99% with yields of >93%. Tungsten promoted titania (10, 20, 30%W-Ti) and hafnia (10%W-Hf) were found to be more active than zirconia (10%W-Zr) for the reaction. The samples were then tested for phenylacetaldehyde acetalization (entry 2). Acetalization of aliphatic aldehydes is known to be more difficult than with aromatic or conjugated aldehydes. The most active catalysts for the reaction are 20% and 30%W-Ti. The highest conversion obtained is 55% (30%W-Ti) and the highest yield is 50% (20%W-Ti).Tungsten promoted zirconia (10%W-Zr) and hafnia (10%W-Hf) showed no activity for the reactions (**Table 3.3**, entry 2). Cyclohexanone and acetophenone were used as substrates for the ketalization reactions with methanol. Tungsten promoted zirconia (10%W-Zr) and hafnia (10%W-Hf) samples showed no activity. The reactions were also conducted at higher temperatures (50 and 70^0C) with these two catalysts, however no activity is observed for all temperatures studied. On the other hand, all tungsten promoted titania (X%W-Ti) samples were found to be very active for cyclohexanone ketalization, with > 96% conversions and > 90% yields (entry 3). For acetophenone ketalization, the 20%W-Ti sample was found to be the most active catalyst showing 37% conversion with 33% yield (entry 4). Tungsten promoted titania samples

showed higher activity in all conducted acetalization and ketalization reactions. The 20% tungsten loading is found to be the optimum tungsten amount for the mesoporous titania support. Solvent free ketalization of ketones by methanol was previously studied by several other researchers[22,26,32,34]. Water tolerant metal triflates ($Al(OTf)_3$ and $In(OTF)_3$), rare earth-exchanged Mg-Y zeolites, and sulfated zirconia (S-Zr) were the catalysts in these studies. For ketalization of cyclohexanone with methanol, Bradley *et al.* obtained an 80% yield with $Al(OTf)_3$ and Smith *et al.* obtained an 84% cyclohexanone dimethyl ketal yield with $In(OTf)_3$ (both reactions at RT and 1 h)[32,34]. Sinhamahapatra *et al.* used S-Zr for ketalization of several ketones with methanol at RT.[22] Conversions of 97% and 85% were obtained for ketalization of cyclohexanone and acetophenone, respectively. Thomas *et al.* tried several rare earth-exchanged Mg-Y zeolites for ketalization of acetophenone with methanol. The highest catalytic activity was obtained for Ce-Mg-Y (Ceria-exchanged zeolite) catalysts; 75% conversion was obtained at 80^{o}C after 10 h[26].

Table 3.3. Acetalization and Ketalization of various substrates with methanol over tungsten promoted mesoporous catalysts.

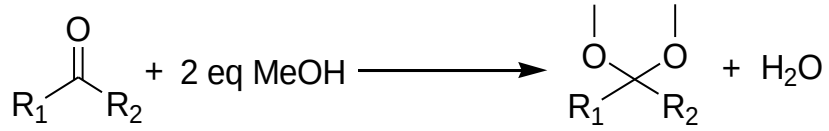

Entry	Substrate	Product	Catalyst	Time (h)	Conversion[a] (%)	Yield[a] (%)
1	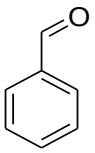	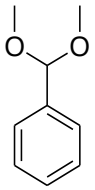	0%W-Ti	2	70	66
			5%W-Ti	2	81	74
			10%W-Ti	2	99	91
			20%W-Ti	2	99	93
			30%W-Ti	2	99	94
			10%W-Zr	2	75	62
			10%W-Hf	2	97	95
2	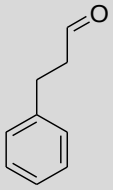	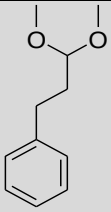	0%W-Ti	4	0	0
			5%W-Ti	4	3	<1
			10%W-Ti	4	14	11
			20%W-Ti	4	52	50
			30%W-Ti	4	55	46
			10%W-Zr	4	0	0
			10%W-Hf	4	0	0
3	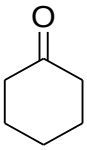	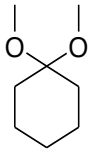	0%W-Ti	2	27	25
			5%W-Ti	2	96	90
			10%W-Ti	2	97	93
			20%W-Ti	2	96	94
			30%W-Ti	2	96	93
			10%W-Zr	2	0	0
			10%W-Hf	2	0	0
4	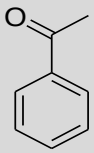	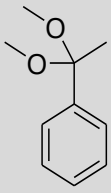	0%W-Ti	4	0	0
			5%W-Ti	4	<1	0
			10%W-Ti	4	29	28
			20%W-Ti	4	37	33
			30%W-Ti	4	14	10
			10%W-Zr	4	0	0
			10%W-Hf	4	0	0

Reaction conditions: 0.5 mmol substrate in 5 mL MeOH (0.1M), 25 mg of catalysts at RT.
a. GC-FID yield.

3.3.6.2 The effect of water (water toleration) and temperature

The mechanism of acetalization and ketalization has been investigated in several studies and a two-step, reversible reaction mechanism has been proposed [25,26,59]. In the first step, the adsorbed substrate is protonated and a hemiacetal is formed by the addition of one alcohol and removal of one proton. In the second step, the formed hemiacetal is protonated (rate determining step) and a water molecule is removed to form a cation[26]. The second step is slow and requires a polar environment for the stabilization of the formed cationic hemiacetal intermediate. Finally, the reaction is completed by the subtraction of one proton to form an acetal or ketal[26]. One of the major concerns of this reaction is the water content in the reaction media, which is a side product of the reaction. The formed water is accumulated on the catalyst surface and is accepted as the major reason that stops the reaction [25,27,32,35].

Therefore, water is generally *in situ* removed from the reaction media (with a Dean-Stark apparatus). The effect of water on the ketalization of cyclohexanone was investigated with the 10%W-Ti sample. **Figure 3.9A** shows the reaction yields for two different substrate concentrations (0.1 and 0.2 M) at various water amounts (0 to 10 mmol). Despite the activity slowly decreasing with increasing water amount, the catalyst still shows a decent activity even with high water containing reactions. The 10%W-Ti catalyst gives 55% yield in the presence of 10 mmol water. The amount of water added is 20 times the amount of substrate used (for 0.1 M substrate and 10 times for 0.2 M substrate concentration). For example, the reaction performed with 0.5 mmol substrate produces 0.5 mmol water for the case of 100% conversion, adding such an amount of water (0.5 mmol) at the beginning of the reaction decreased the yield by only 4% (**Figure 3.9A**).

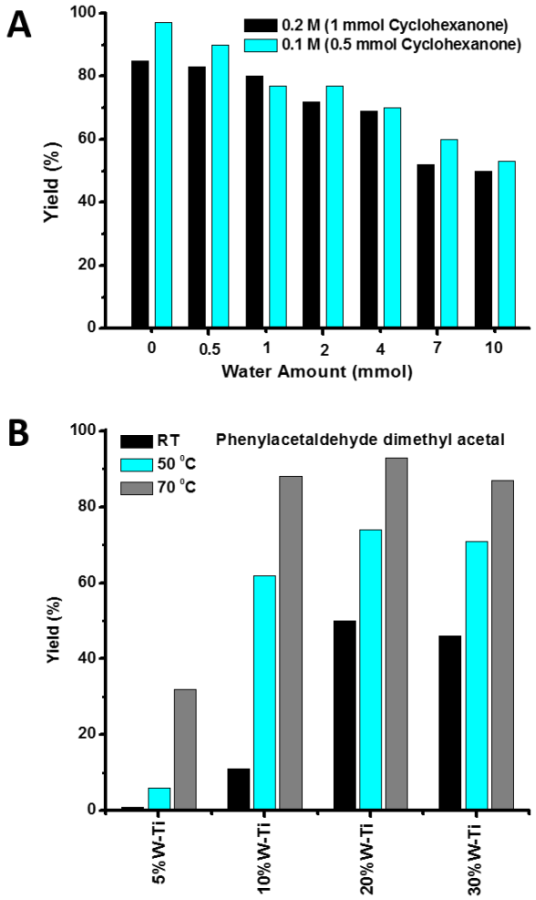

Figure 3.9 (A) Effect of water content on cyclohexanone ketalization with 10%W-Ti catalyst (0.5-1 mmol substrate in 5 mL MeOH (0.1-0.2M), 25 mg of catalysts, RT, 2h). (B) Effect of temperature on phenyl acetaldehyde acetalization with X%W-Ti catalyst, where X=5, 10, 20, 30 (0.5 mmol substrate in 5 mL MeOH (0.1M), 25 mg of catalysts, RT-70 ^{0}C, 4h).

The effect of temperature was also investigated for the acetalization of phenylacetaldehyde (**Figure 7B**). The reactions were chosen as the model reactions for the investigation of the effect of temperature, since relatively low activity for the conversion of the substrate can be enhanced with an increase of temperature (**Table 3.3**). The activity was drastically enhanced for the acetalization of phenylacetaldehyde with increased temperature. For example, the yield increased from 50% (at RT) to 93% (at 70 ^{0}C) for the 20%W-Ti

catalyst. All tungsten promoted titania samples performed better at high reaction temperatures for the acetalization reaction.

3.3.6.3 Catalyst recycle, amount and comparison with other heterogeneous acid catalysts

Cyclohexanone ketalization by the 10%W-Ti sample was used as the model reaction for catalyst recycling and optimization studies (**Figure 3.10A** and **B,** respectively). The 10%W-Ti catalyst was recycled five times with almost no performance loss (~3-4%). The used catalyst, after each reaction, was first washed with toluene several times to remove adsorbed species and then with methanol, followed by a vacuum drying, and reactivation at 250^0C for 10 min. Another recycle test was also performed by washing the used catalyst with methanol only and reactivation at 250^0C. The activity gradually decreased to 35% after the 4^{th} run (not shown). The reason for this is believed to be that washing only with methanol is not enough to remove all adsorbed species and failing to remove all the species causes a decrease in catalytic activity. **Figure 3.10C** shows the effect of the catalyst amount on conversions and yields of cyclohexanone ketalization reaction with the 10%W-Ti catalyst. The catalyst shows high conversions even at very low catalyst amounts, 81% conversion and 70% yield with 5 mg of catalyst. The conversion increases to 97% with 10 mg of 10%W-Ti catalyst. Further increasing the catalyst amount does not change the conversion (96-97%). However, the yield slowly decreases from 95% to 87% as the catalyst amount goes up from 10 to 50 mg. The decrease of the yield is attributed to the adsorption of the ketal in the mesopores.

Finally, several commercial (Degussa (P25) & amberlyst-15) and non-commercial (tungsten oxide (WO_3), sulfated titania (S-Ti) & sulfated zirconia (S-Zr)) catalysts were tested under the same reaction conditions for better performance evaluation of the tungstated mesoporous catalysts. **Figure 3.10C** shows the catalytic performances of these catalysts along

with the X%W-Ti catalysts for acetophenone ketalization with MeOH at RT. 10%W-Ti and 20%W-Ti showed the best performance for the reaction, giving yields of 28% and 33%, respectively. S-Ti, S-Zr, and amberlyst-15 have relatively lower activity. However, considering the well-known sulfate leaching problems for the sulfated catalysts and recyclability problem of amberlyst 15, tungsten promoted mesoporous titania appears to be better for these reactions.

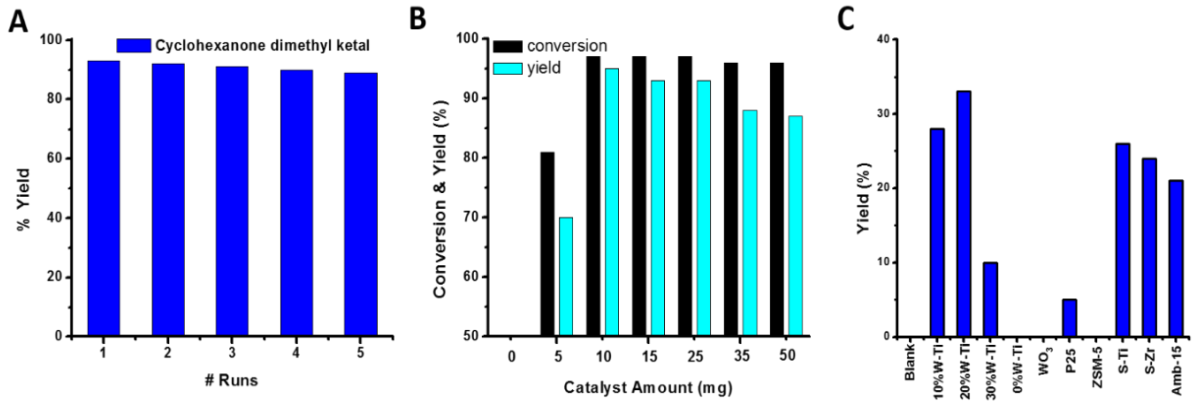

Figure 3.10 (A) Catalyst recycle studies and (B) Effect of Catalyst amount on cyclohexanone ketalization with 10%W-Ti catalyst (0.5 mmol substrate in 5 mL MeOH (0.1), 25 mg of catalysts, RT, 2h). (C) Comparison of various heterogeneous commercial and non-commercial catalysts for acetophenone ketalization (0.5 mmol substrate in 5 mL MeOH (0.1M), 25 mg of catalysts, RT, 4 h).

3.4 Discussion

3.4.1 Formation Mechanism of Tungstated Mesoporous Group 4 TMs

In this work, tungsten promoted mesoporous group 4 transition metal (TM) oxides were prepared with the recently developed approach by using ammonium metatungstate as a tungsten source. In general, the method uses inverse non-ionic surfactant micelles (P123) as a soft template and the sol-gel process is controlled in acidic media (HNO_3 + n-butanol) by NOx chemistry. Thermal decomposition of nitrate ion forms a wide range of nitric oxides generally referred to as NOx. The formed NOx is adsorbed on oxo-clusters to prevent uncontrolled condensation and the decomposition of NOx species gradually increases the pH to control the condensation of inorganic components[37]. The tungsten source is negatively charged metatungstate and is introduced in an alcoholic solution (ethanol + water). Introduction of the metatungstate solution to the acidic reaction gel (P123+ TM source, HNO_3 + n-butanol) resulted in a quick color change to opaque (white for high tungsten loadings) and freezing of the gel. The formed frozen gels were further aged in an oven at 120^{o}C for several hours. The immediate gel freezing is attributed to a rapid combination of positively charged TM sols and negatively charged metatungstate to form a rigid gel. The gel formation time depends on the tungsten amount. The gel formation can take as long as 1 h for low tungsten loadings (5%) and can be as quick as < 1 min for high tungsten loadings (30%). After aging the gels in an oven (120^{o}C), the organic components were removed by a calcination step at 600^{o}C under air.

3.4.2 Physicochemical Properties of Tungstated Mesoporous Group 4 TMs

The tungsten promoted mesoporous TM oxides demonstrate typical features of UCT mesoporous materials. One low-angle diffraction line indicates a regular mesostructure and a Type IV adsorption isotherm indicates a monomodal pore size distribution (**Figure 3.1A, B & 3.5A, C**). The mesostructure is established by the randomly packed monodispersed nano-particles. The position of the low angle diffraction line corresponds to the sizes of building blocks (nano-particles) and the BJH pore size distributions give the average size of connected intraparticle voids. The low angle diffraction line positions and mesopore sizes are summarized in **Table 3.1**. Tungsten exists as well-sintered nano-clusters (< 1 nm) on the TM supports as suggested by the spectroscopic characterization (Raman (**Figure 3.6A**) & XPS (**Figure 3.7**)) and TEM analyses (**Figure 3.8**). The supported tungsten nano-clusters promote the formation of acid sites, mostly Brønsted acid sites (**Figure 3.1D**). The titania support shows the highest amount of Brønsted acid sites compared to zirconium and hafnium oxide supports (**Figure 3.1D**). The bare titania sample (0%W-Ti) shows only Lewis acid sites.

Brønsted acid sites are formed and increase in number with increasing amount of tungsten loading (0-30%). The tungsten clusters also hinder the crystal growth and stabilize the mesostructure by preventing nano-particle sintering. Therefore, the promoted samples have smaller Schrerrer crystallite sizes (broader PXRD lines) and the low-angle PXRD diffraction line positions are increased suggesting smaller nano-particle sizes exist as compared to non-promoted TM supports. Disappearance of the low angle diffraction line is generally observed at high calcination temperatures and times due to sintering of nanoparticles to form bigger aggregates. For example, the mesostructure of the 0%W-Ti sample collapses after calcination at 600^{o}C. On the other hand tungsten promoted titania samples preserve both the

mesostructure and mesoporosity. The obtained porosity and surface area data are consistent with the PXRD results and suggest that tungsten loading does not only prevent the crystal growth of the template but also stabilizes the mesoporosity by preventing nanoparticle sintering.

3.4.3 Acetalization and Ketalization

Acetalization and ketalization of several aldehydes (benzaldehyde, cinnamonaldehyde, and phenyl acetaldeyde) and ketones (cyclohexanone and acetophenone) with MeOH were conducted with the tungsten promoted mesoporous oxides (**Table 3.3**). Among all of the 10%W promoted mesoporous group 4 TM oxides, titania is found to be the most active support. For all catalytic reactions (regardless of substrate) the titania support performed better than zirconia and hafnia supports. Strong adsorption of the substrates into mesopores and protonation of adsorbed substrates to form hemiacetals are the key steps in these reactions [25,26,59]. Therefore, the high activity of tungsten promoted titania (X%W-Ti) samples is attributed to relatively higher Brønsted acidity (**Figure 3.6B**) promoted by nano-WOx clusters and high adsorption capacity of regular mesopores. High adsorption capacity of these samples is also believed to be the reason for retaining catalytic activity in the presence of water (**Figure 3.9A**). As discussed in several studies, water in the reaction media competes with substrates and is adsorbed on the catalyst surface which decreases the catalytic activity [25,26,30]. High adsorption capacity of mesoporous materials is a well-known property of mesoporous materials. Despite the above-mentioned advantages of mesoporosity of X%W-Ti samples for these reactions, adsorbed species (reactant, intermediate, and products) can also be a limiting factor. For example, in catalyst amount studies (**Figure 3.10B**), the yield of cyclohexanone dimethyl ketal decreases from 95% to 87% with an increasing catalyst amount

from 10 to 50 mg, despite the conversion remaining same (~97%). Probably the ketal product is adsorbed in the mesopores of the catalyst. The same conclusion can also be derived from catalyst recycle studies (**Figure 3.10A**).

The catalytic performance can only be restored after a toluene washing to remove adsorbed species. Failure to remove adsorbed species (methanol only washing) decreases the catalytic performance of the recycled catalyst. In order to investigate the adsorbed species on the used catalyst of the cyclohexanone ketalization reaction was analyzed by Direct Analysis in Real Time Mass Spectroscopy (DART-MS). The results were too complicated to reach a conclusion about the adsorbed species, but the spectrum was also different than the substrate and product, possibly indicating adsorbed intermediates (like hemiacetals) along with reactants and products. The high adsorption capacity of the tungsten promoted catalyst is also believed to be the reason for both the conversion yield difference (**Table 3.3**) and the major limiting factor stopping the reaction for certain substrates.

3.5 Conclusion:

In summary, tungsten loaded mesoporous titania (UCT-55), zirconia (UCT-50), and hafnia (UCT-56) were synthesized using the novel one step University of Connecticut (UCT) approach. The materials demonstrate the typical features of UCT materials, having one low angle diffraction line which indicates the nano-particle size (10.3-12.6 nm) and Type IV sorption isotherms with pore sizes ranging from 3.8 to 6.1 nm. The nano-particles are crystalline and the Scherrer crystalline sizes depend on the tungsten loading. The crystallite size decreases gradually from 8.5 to 2.5 nm with increasing tungsten loading from 0 to 30%. Cinnamonaldehyde acetalization results suggest the order of activity among the mesoporous supports is Ti>Hf>Zr. The tungsten exists as very small (< 1 nm) clusters well dispersed on the TM support. The clusters are responsible for enhanced acidic properties by promoting the formation of Brønsted acid sites. The catalytic activities of these materials give high yields and conversions for acetalization and ketalization of several aldehydes and ketones at RT under solvent free conditions. The optimum tungsten loading is found to be 20% (w.r.t Ti) for UCT-55. The tungsten promoted samples were found to tolerate small amounts of water (0-0.1 mmol) for ketalization of cyclohexanone. The recycled tungsten promoted titania catalyst (10%W-Ti) showed a high activity with a minor performance loss (~3-4 %) after several cycles. After testing several commercial and non-commercial catalysts under the same reaction conditions, the high activity for UCT materials clearly shows the significance and novelty of the tungsten loaded group 4 metal oxides.

3.6 References

1. Jiao, F.; Frei, H. *Angew. Chem. Int. Ed.* **2009**, *48*, 1841–1844.

2. Sinha, A. K.; Suzuki, K. *Appl. Catal. B: Environ.* **2007**, *70*, 417–422.

3. Ding, Y.-S.; Shen, X.-F.; Gomez, S.; Luo, H.; Aindow, M.; Suib, S. L. *Adv. Funct. Mater.* **2006**, *16*, 549–555.

4. Corma, A.; Iborra, S.; Velty, A. *Chem. Rev.* **2007**, *107*, 2411–2502.

5. Vos, D. E. D.; Dams, M.; Sels, B. F.; Jacobs, P. A. *Chem. Rev.* **2002**, *102*, 3615–3640.

6. Taguchi, A.; Schüth, F. *Microporous Mesoporous Mater.* **2005**, *77*, 1–45.

7. Kourieh, R.; Rakic, V.; Bennici, S.; Auroux, A. *Catal. Commun.* **2013**, *30*, 5–13.

8. Dutta, S. *RSC Adv.* **2012**, *2*, 12575.

9. Pagliaro, M.; Ciriminna, R.; Kimura, H.; Rossi, M.; Della Pina, C. *Angew. Chem. Int. Ed.* **2007**, *46*, 4434–4440.

10. Alonso, D. M.; Bond, J. Q.; Dumesic, J. A. *Green Chem.* **2010**, *12*, 1493.

11. Serrano-Ruiz, J. C.; Luque, R.; Sepúlveda-Escribano, A. *Chem. Soc. Rev.* **2011**, *40*, 5266.

12. Sivasamy, A.; Cheah, K. Y.; Fornasiero, P.; Kemausuor, F.; Zinoviev, S.; Miertus, S. *ChemSusChem* **2009**, *2*, 278–300.

13. Gallezot, P. *Chem. Soc. Rev.* **2012**, 41, 1538-1558.

14. Clark, J. H. *Accounts Chem. Res.* **2002**, *35*, 791–797.

15. Chen, L. F.; Noreña, L. E.; Navarrete, J.; Wang, J. A. *Mater. Chem. Phys.* **2006**, *97*, 236–242.

16. Melero, J. A.; Grieken, R. van; Morales, G. *Chem. Rev.* **2006**, *106*, 3790–3812.

17. Karimi, B.; Ghoreishi-Nezhad, M. *J. Mol. Catal. A: Chem.* **2007**, *277*, 262–265.

18. Maksimov, G. M.; Litvak, G. S.; Budneva, A. A.; Paukshtis, E. A.; Salanov, A. N.;

Likholobov, V. A. *Kinet. Catal.* **2006**, *47*, 564–571.

19. Corma, A.; Martinez, A.; Martinez, C. *Applied Catalysis A: General*, 1996, *144*, 249–268.

20. López, D. E.; Goodwin Jr., J. G.; Bruce, D. A.; Furuta, S. *Appl. Catal. A: Gen.* **2008**, *339*, 76–83.

21. Zareyee, D.; Khalilzadeh, M. A. *Int. J. Green Nanotechnol.* **2012**, *4*, 377–384.

22. Sinhamahapatra, A.; Sutradhar, N.; Ghosh, M.; Bajaj, H. C.; Panda, A. B. *Appl. Catal. A: Gen.* **2011**, *402*, 87–93.

23. Greene, T. W.; Wuts, P. G.; Wiley, J. *Protective groups in organic synthesis*; Wiley New York, 1999; Vol. 168.

24. Bauer, K.; Garbe, D.; Surburg, H. *Common fragrance and flavor materials*; Wiley. com, 2008.

25. Climent, M. J.; Velty, A.; Corma, A. *Green Chem.* **2002**, *4*, 565–569.

26. Thomas, B.; Prathapan, S.; Sugunan, S. *Microporous Mesoporous Mater.* **2005**, *80*, 65–72.

27. Wu, S.; Dai, W.; Yin, S.; Li, W.; Au, C.-T. *Catal. Lett.* **2008**, *124*, 127–132.

28. Tao, D.-J.; Li, Z.-M.; Cheng, Z.; Hu, N.; Chen, X.-S. *Ind. & Eng. Chem. Res.* **2012**, *51*, 16263–16269.

29. Sudarsanam, P.; Mallesham, B.; Prasad, A. N.; Reddy, P. S.; Reddy, B. M. *Fuel Process. Technol.* **2013**, *106*, 539–545.

30. Mallesham, B.; Sudarsanam, P.; Raju, G.; Reddy, B. M. *Green Chem.* **2013**, *15*, 478.

31. Saha, M.; Bhar, S. *Green Chem. Lett. Rev.* **2011**, *4*, 137–142.

32. Smith, B. M.; Kubczyk, T. M.; Graham, A. E. *RSC Adv.* **2012**, *2*, 2702.

33. Duan, Z.; Gu, Y.; Deng, Y. *Catal. Commun.* **2006**, *7*, 651–656.

34. Williams, D. B. G.; Lawton, M. C. *Green Chem.* **2008**, *10*, 914.

35. Patel, S. M.; Chudasama, U. V.; Ganeshpure, P. A. *J. Mol. Catal. A: Chem.* **2003**, *194*, 267–271.

36. Zhi-Wang, Y.; Li-Na, C.; Wei, H.; Rui-Xue, K.; Jia, W.; Na, J.; Lei, Z.; Heng-Chang, M. *Acta PHYSICO-CHIMICA Sin.* **2012**, *28*, 2148–2154.

37. Poyraz, A. S.; Kuo, C.-H.; Biswas, S.; King'ondu, C. K.; Suib, S. L. *Nat. Commun.* **2013**, *4*.

38. Lopez, D.; Suwannakaran, K.; Bruce, D.; GoodwinJr, J. *J. Catal.* **2007**, *247*, 43–50.

39. Smith, W.; Wolcott, A.; Fitzmorris, R. C.; Zhang, J. Z.; Zhao, Y. *J. Mater. Chem.* **2011**, *21*, 10792.

40. Digregorio, F. *J. Catal.* **2004**, *225*, 45–55.

41. Cortés-Jácome, M. A.; Angeles-Chavez, C.; López-Salinas, E.; Navarrete, J.; Toribio, P.; Toledo, J. A. *Appl. Catal. A: Gen.* **2007**, *318*, 178–189.

42. Cortes-Jácome, M. A.; Morales, M.; Chavez, C. A.; Ramírez-Verduzco, L. F.; López-Salinas, E.; Toledo-Antonio, J. A. *Chem. Mater.* **2007**, *19*, 6605–6614.

43. Eibl, S.; Gates, B. C.; Knözinger, H. *Langmuir* **2001**, *17*, 107–115.

44. Su, D.; Wang, J.; Tang, Y.; Liu, C.; Liu, L.; Han, X. *Chem. Commun.* **2011**, *47*, 4231.

45. Selli, E.; Forni, L. *Microporous Mesoporous Mater.* **1999**, *31*, 129–140.

46. Zhou, W.; Ross-Medgaarden, E. I.; Knowles, W. V.; Wong, M. S.; Wachs, I. E.; Kiely, C. J. *Nat. Chem.* **2009**, *1*, 722–728.

47. Riboni, F.; Bettini, L. G.; Bahnemann, D. W.; Selli, E. *Catal. Today* **2013**, *209*, 28–34.

48. Jin, M.; Zhang, X.; Pu, H.; Nishimoto, S.; Murakami, T.; Fujishima, A. *J. Colloid Interface Sci.* **2011**, *362*, 188–193.

49. Yang, L.; Xiao, Y.; Liu, S.; Li, Y.; Cai, Q.; Luo, S.; Zeng, G. *Appl. Catal. B: Environ.* **2010**, *94*, 142–149.

50. Leghari, S., Ahmed,Khan; Sajjad, S.; Chen, F.; Zhang, J. **2011**, *166*.

51. Reddy, B. M.; Sreekanth, P. M.; Yamada, Y.; Xu, Q.; Kobayashi, T. *Appl. Catal. A: Gen.* **2002**, *228*, 269–278.

52. Scholz, A.; Schnyder, B.; Wokaun, A. *J. Mol. Catal. A: Chem.* **1999**, *138*, 249–261.

53. Reddy, B., M.; Reddy, G., K.; Rao, K., N.; Katta, L. **2009**, *306*.

54. Dupin, J.-C.; Gonbeau, D.; Vinatier, P.; Levasseur, A. *Phys. Chem. Chem. Phys.* **2000**, *2*, 1319–1324.

55. Surface Chemistry of H2S-sensitive tungsten oxide films. *Sensors and Actuators B,* 1996, 167–174.

56. Martinez, A.; Prieto, G.; Arribas, M.; Concepcion, P.; Sanchezroyo, J. *J. Catal.* **2007**, *248*, 288–302.

57. Liu, Z.; Zhao, Z.-G.; Miyauchi, M. *J. Phys. Chem. C* **2009**, *113*, 17132–17137.

58. Electrochromic tungsten oxide films: Review of progress 1993-1998. *solar energy materials and Solar Cells*, 2000, 201–262.

59. Tan, M. X.; Gu, L.; Li, N.; Ying, J. Y.; Zhang, Y. *Green Chem.* **2013**, *15*, 1127–1132.

Chapter 4: Crystalline Mesoporous $K_{2-x}Mn_8O_{16}$ (K-OMS-2) and ε-MnO_2 by Mild Transformations of Amorphous Mesoporous Manganese Oxide and Their Enhanced Redox Properties.

4.1 Introduction

Nanocrystalline and monomodal pore size multivalent mesoporous transition metal oxides (MTMOs) have attracted much attention in the past two decades and have been the subject of thousands of research studies. The interest in multivalent MTMOs originates from their catalytic, electronic, sorption, and magnetic properties which are superior to those of their non-porous counterparts[1–9]. However, due to synthetic limitations in sol-gel chemistry of TMs, multivalent MTMOs (i.e. Fe, Mn, and Co) can only be synthesized with a limited (usually one) number of crystal phases[2,4,7,10–14]. The lack of available precursors, filled or half-filled d orbitals, and weak surfactant TM sol interactions are the major limiting factors. These factors limit the potential use of mesoporous MTMOs for various applications, since their versatility arises from the numerous oxide structures, polymorphs, and stable oxidation states[15–22]. The situation is more complicated for manganese oxides. In addition to thermodynamically stable major Mn_2O_3 (Bixybyite, Mn=3+), Mn_3O_4 (Hausmannite, Mn=2+ & 3+), and β-MnO_2 (Mn=4+) phases, there are also many other oxide structures (i.e. Mn_5O_8 & MnO), polymorphs of MnO_2 (α-, β-, γ-, δ-, ε-, and λ-), and cation stabilized octahedral coordinated microporous manganese oxides (octahedral molecular sieves, OMS)[23–27]. Thus far, ordered mesoporous manganese oxides have only been synthesized with Mn_2O_3 (Bixybyite) or Mn_3O_4 (Hausmannite) phases by direct sol-gel methods[2,12]. Other phases such as $K_{2-x}Mn_8O_{16}$ (Cryptomelane) and γ-MnO_2 have only been obtained using a hard template (nanocasting) such as mesoporous silica (i.e. SBA-16 & KIT-6)[28,29]. In these studies, a

mesoporous silica was used as hard template, the mesopores of the template was filled up with manganese source, and then the manganese source was converted to the corresponding oxide by a thermal treatment. This approach requires subsequent template removal by NaOH following the formation of the desired oxide structure.

In this chapter of the thesis, we are reporting the transformation of mesoporous amorphous manganese oxide (Meso-Mn-A) to crystalline mesoporous Mn_2O_3 (Meso-Mn_2O_3), ε-MnO_2 (Meso-ε-MnO_2), and K_{2-x}-Mn_8O_{16} (Meso-OMS-2) materials by preserving the mesoporosity under mild (0.2-0.5 M H^+ & 40-70^{o}C) conditions. **Figure 4.1** summarizes the transformation conditions for the materials mentioned in this chapter. The as synthesized amorphous mesoporous manganese oxide (Meso-Mn) was subjected to a heating cycle of 150^{o}C (10 h) + 250^{o}C (3 h) + 350^{o}C (2 h) to form amorphous Meso-Mn-A. Meso-Mn-A was used as a substrate to form other crystalline mesoporous manganese oxides: (1) Meso-Mn_2O_3 was formed by heating Meso-Mn-A at 450^{o}C for 1 h, (2) Meso-ε-MnO_2 was synthesized by treating Meso-Mn-A in a 0.5 M aqueous sulfuric acid solution at 70^{o}C for 2 h, and (3) Meso-OMS-2 was synthesized by treating Meso-Mn-A in a 0.5 M aqueous sulfuric acid solution containing 0.5 M KCl at 70^{o}C for 2 h.

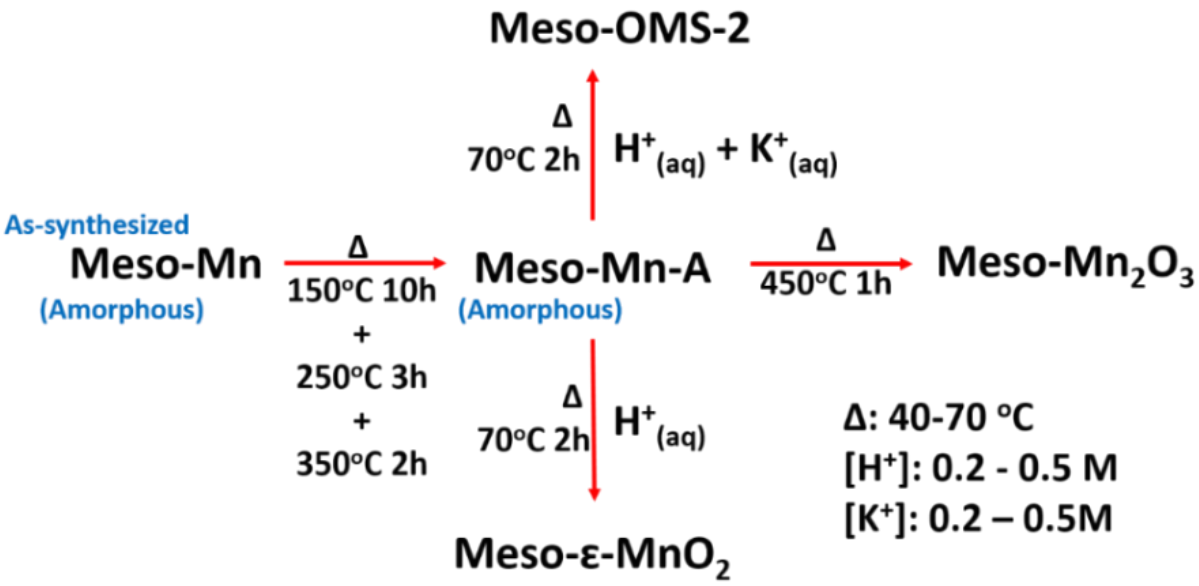

Figure 4.1: Schematic illustration of the synthetic approach to form crystalline mesoporous manganese oxides.

4.2 Experimental Section

4.2.1 Chemicals

Manganese nitrate tetrahydrate ($Mn(NO_3)_2 \cdot 4H_2O$, ≥97.0%), 1-butanol (anhydrous, 99.8%), block-poly(ethylene glycol)-block-Poly(propylene glycol)-block-Poly(ethylene glycol) $PEO_{20}–PPO_{70}–PEO_{20}$ (Pluronic P123), potassium chloride (KCl, ≥99.0%), manganese (III) oxide (Mn_2O_3, 99%), and manganese (II, III) oxide (Mn_3O_4, 97%) were purchased from Sigma-Aldrich. Concentrated sulfuric acid (H_2SO_4, 95-98%) and concentrated nitric acid (HNO_3, 68%-70%) were purchased from J. T. Baker. All chemicals were used as received without any purification.

4.2.2 Synthesis of Mesoporous Manganese Oxides:

Amorphous mesoporous manganese oxide was synthesized using the procedure of Poyraz et al[2]. and used as the precursor for the synthesis of several other mesoporous manganese oxide materials with different crystal structures. In a typical synthesis, 5.0 g (0.02 mol) of $Mn(NO_3)_2 \cdot 4H_2O$ was dissolved in a solution containing 14 g (0.188 mol) of 1-butanol, 2 g (0.032 mol) of HNO_3 and 2 g (3.44×10^{-4} mol) of P123 surfactant in a 150- ml beaker at room temperature (RT) and under magnetic stirring. The obtained clear gel is placed in an oven at 120^{o}C for 4 h. The obtained powder was washed several times with ethanol and then the powder is centrifuged. Finally, the powder is dried in a vacuum oven overnight. The dried powder was subjected to a heating cycle (150^{o}C for 10-12h + 250^{o}C (3h) + 350^{o}C (2h)). The powder was removed from the oven and naturally cooled down to RT after each heating step. All heat treatments were done under air. The sample was labelled as Meso-Mn-A, where A stands for amorphous.

4.2.3 Synthesis of Mesoporous Mn_2O_3:

Amorphous Meso-Mn-A sample was heated at 450^{o}C (1 h) to obtain crystalline mesoporous Mn_2O_3 material. The sample was labelled as Meso-Mn_2O_3. Commercial Mn_2O_3 (purchased from Sigma-Aldrich) was labeled as C-Mn_2O_3.

4.2.4 Synthesis of Mesoporous ε-MnO_2:

Amorphous Meso-Mn-A sample (0.3 g) was dispersed in 50 mL 0.5M H_2SO_4 aqueous solution (DDI water) and sonicated at RT for 10 min. The formed homogeneous suspension was transferred to a glass autoclave and the autoclave was placed in an oven running at 70^{o}C for 2 h. The obtained powder was filtered and washed several timed with DDI water and finally dried in a vacuum oven over night. The sample was labelled as Meso-ε-MnO_2.

4.2.5 Synthesis of Mesoporous $K_{2-x}Mn_8O_{16}$ (Cryptomelane) (OMS-2):

Amorphous Meso-Mn-A sample (0.3 g) was dispersed in a 50 mL aqueous solution (DDI water) containing 0.5M H_2SO_4 + 0.5M KCl and sonicated at RT for 10 min. The formed homogeneous suspension was transferred to a glass autoclave and the autoclave was placed in an oven running at 70^{o}C for 2 h. The obtained powder was filtered and washed several timed with DDI water and finally dried in a vacuum oven over night. The sample was labelled as Meso-OMS-2. A non-porous OMS-2 material was also synthesized for comparison with reflux method using procedure of DeGuzman et al[36]. OMS-2 material synthesized with reflux method was labeled as R-OMS-2.

4.2.6 Catalyst Characterization:

PXRD analyses were performed on a Rigaku Ultima IV diffractometer (Cu Kα radiation of 1.5406 A) with an operating voltage of 40 kV and a current of 44 mA. Both low-angle (2θ = 0.5 - 8) and wide-angle (2θ = 10 - 75) diffraction patterns were collected. N_2 sorption isotherms were collected on a Quantachrome Autosorb-1-1C automated adsorption system. The samples were degassed at 200 ºC for 4 h prior to the analyses. The surface areas were calculated using the Brunauer-Emmett-Teller (BET) method and the pore size distributions were obtained by Barrett-Joyner-Halenda (BJH) method from the desorption branch of the isotherms. HR-TEM images of synthesized mesoporous materials were recorded on a JEOL 2010 FasTEM microscope operating at 200 kV. Temperature programmed reduction mass spectrometry (TPR-MS) was completed using an MKS PPT Quadrupole Residual Gas Analyzer equipped with a vacuum manifold that allows for the sampling of gas streams at or near atmospheric pressure. A 100-mg powder sample was loaded into a quartz tube and placed inside a programmable tube furnace. Prior to analysis, the sample was treated at 150^{o}C in air for one hour and brought back to room temperature. A feed gas composed of 5% H_2 in He gas was flowed at 500 sscm while the temperature was ramped at a rate of 10 ^{o}C/min. from room temperature to 800 ^{o}C.

4.2.7 CO Oxidation:

The CO oxidation reactions with O_2 were performed on a continuous flow fixed bed quartz tubular reactor under atmospheric pressures. For each test, 100 mg of catalyst was packed in a quartz tube and the catalyst surfaces were cleaned at 200 ºC for 1 h under helium flow (15 cc/min). After cooling down the catalysts under ambient conditions to RT, a gas mixture containing 1% CO, 5% O_2 balanced in N_2 was passed through the catalyst bed at a

flow rate of 20 mL/min. The outlet gas streams were analyzed by an online gas chromatograph (SRI 8610C Multiple Gas Analyzer #1 GC) equipped with a thermal conductivity detector (TCD). The reaction temperature was measured using a K-type thermocouple inserted directly into the catalyst bed. The reaction conversion were calculated using CO, O_2, and CO_2 concentration; N_2 was used as an internal standard.

4.3 Results

4.3.1 Physicochemical Characterization of Mesoporous Manganese Oxides:

Figure 4.2a shows the low-angle PXRD patterns of the mesoporous samples. All samples have one low-angle diffraction line indicating the existence of a mesostructure. The positions of the diffraction lines are at around ~8 nm for all the mesoporous samples except Meso-Mn_2O_3 (10.8 nm) (see **Table 4.1**). The increase is attributed to a unit-cell expansion upon heat treatment caused by nano-particle sintering, which is also typical for UCT materials[2,30]. **Figure 4.2b** shows the wide-angle PXRD patterns of mesoporous manganese oxides. Meso-Mn-A does not show any diffraction lines (amorphous) whereas Meso-Mn_2O_3 shows bixbyite (Mn_2O_3) crystal structure with a crystallite size of 11.8 nm (**Table 4.1**). Acid treatment of Meso-Mn-A sample yielded the ε-MnO_2 (Meso-ε-MnO_2) phase with a crystallite size of 2.3 nm (**Figure 4.2b** & **Table 4.1**). The ε-MnO_2 (Akhtenskite) is a relatively less known phase of manganese oxide and is structurally (and electrochemically) very similar to γ-MnO_2 phase[24–26]. Both (ε- and γ-) consist of an intergrowth 1x1 pyrolusite (2.3 Å x 2.3 Å) phase and a 1x2 ramsdellite (4.6 Å x 2.3 Å) phase. However, the ε- phase shows more structural faults (De Wolff faults) and microtwinning than the γ- phase[24,25]. MnO_6 octahedral units are the building blocks of ε-MnO_2 as well as numerous other microporous manganese oxides known as Octahedral Molecular Sieves (OMS). The micropores of OMS materials are occupied with charge balancing cations (i.e. H^+, K^+, Ag^+, Rb^+, Mg^{2+}, Ba^{2+}) and manganese is mixed-valent with oxidation states of 2+, 3+, and 4+[16,27,31,32]. Among the OMS materials, potassium containing manganese oxide octahedral molecular sieves (K-OMS-2) have attracted much interest due to its considerable redox activity in catalytic reactions[17,20,33–35]. OMS-2 is a synthetic analogue of a naturally occurring microporous manganese oxide

mineral, cryptomelane (4.7 Å x 4.7 Å)[27]. Synthesized mesoporous K-OMS-2 (Meso-OMS-2) has the cryptomelane ($K_{2-x}Mn_8O_{16}$) phase with a crystallite size of 5.0 nm (**Figure 4.2b** & **Table 4.1**). **Figure 4.2** shows the N_2 sorption isotherms (**c**) and BJH desorption pore size distributions (**d**) of mesoporous manganese oxides. BET surface areas, pore sizes, and pore volumes of mesoporous manganese oxides are summarized in **Table 4.1**.

Regardless of applied heat or acid treatments, all the materials have a Type IV adsorption isotherm indicating the existence of mesopores followed by a Type I hysteresis loop suggesting a regular mesoporosity. Acid treated samples exhibit higher mesopore sizes than the parent Meso-Mn-A (3.4 nm) and Meso-Mn_2O_3 (3.8 nm) with Meso-ε-MnO_2 having the largest pore size (5.6 nm). In addition, all mesoporous samples exhibit high BET surface areas (>128 m^2/g) where Meso-OMS-2 is the one with the highest surface area (277 m^2/g). For comparison, commercial Mn_2O_3 (C-Mn_2O_3) and non-porous K-OMS-2 synthesized by reflux methods (R-OMS-2) were also analyzed[36]. Their physicochemical properties are summarized in **Table 4.1** and **Figure 4.3**. Both C-Mn_2O_3 and R-OMS-2 do not have any low-angle diffraction lines (**Figure 4.3a**) and have high crystallinity (**Figure 4.3b** & **Table 4.1**). They also demonstrate a Type III adsorption isotherm due to their non-porous nature (**Figure 4.3c**), and therefore they exhibit low BET surface areas (< 56 m^2/g).

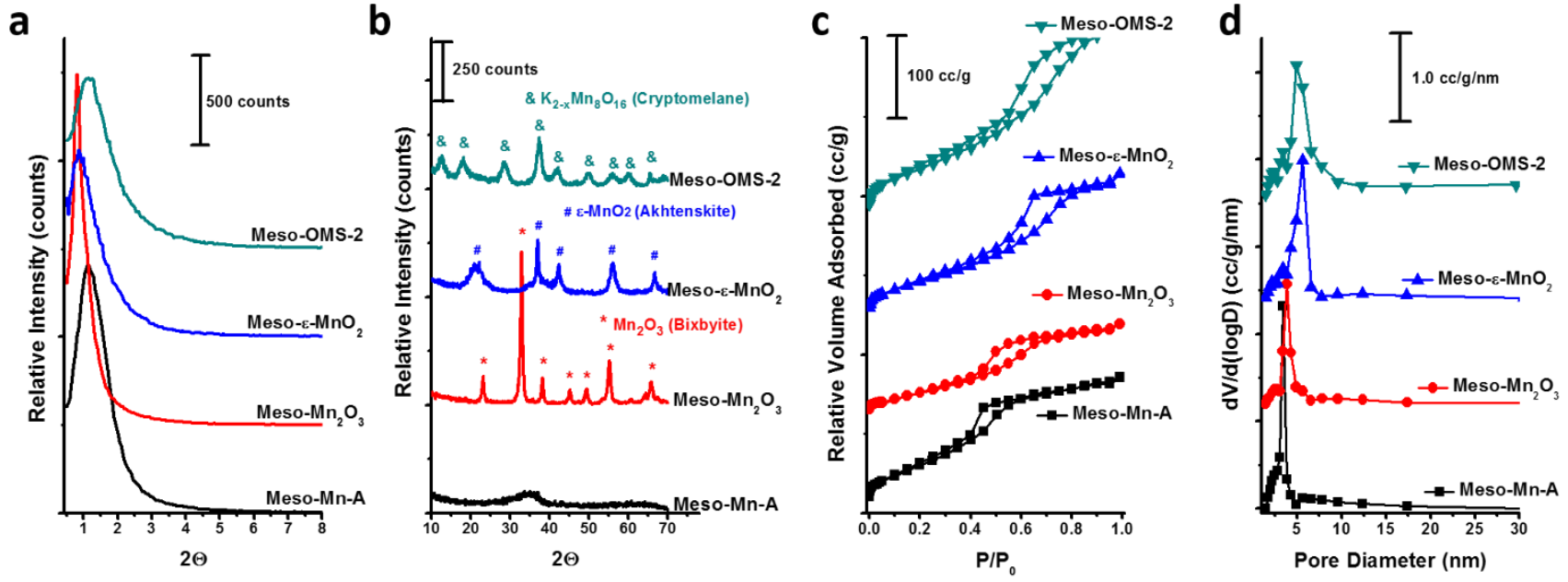

Figure 4.2 (a) Low-angle PXRD, (b) wide-angle PXRD, (c) N_2 sorption isotherms, and (d) BJH Desorption pore size distributions of mesoporous manganese oxides: Meso-Mn-A, Meso-Mn_2O_3, Meso- ε-MnO_2, and Meso-OMS-2.

Table 4.1 Surface area (S_{BET}), BJH desorption pore size distribution (P), BJH desorption pore volume (V), low-angle PXRD peak position (L), Scherrer crystallite size (D), and crystal structure of the mesoporous support.

Sample ID	**L (nm)**	**S_{BET} (m^2/g)**	**P (nm)**	**V (cc/g)**	**D (nm)**	**Crystal Structure**	**T_{100}* (°C)**
Meso-Mn-A	7.9	238	3.4	0.31	NA	NA	25
Meso-Mn_2O_3	10.8	128	3.8	0.22	11.8	Mn_2O_3 (Bixbyite)	50
Meso-ε-MnO_2	8.4	196	5.6	0.32	2.3	ε-MnO_2 (Akhtenskite)	50
Meso-OMS-2	8.2	277	4.8	0.48	5.0	$K_{2-x}Mn_8O_{16}$ (Cryptomelane)	50
C-Mn_2O_3	NA	9	NA	0.01	34.6	Mn_2O_3 (Bixbyite)	NA
R-OMS-2	NA	56	NA	0.69	8.6	$K_{2-x}Mn_8O_{16}$ (Cryptomelane)	225

* T_{100} is 100% conversion temperatures in CO oxidation experiments. The conversion is based on CO.
1%CO + 2% O_2 were diluted in N_2. The flow rate was 15 cc/min. The experiment were conducted at atmospheric pressure.

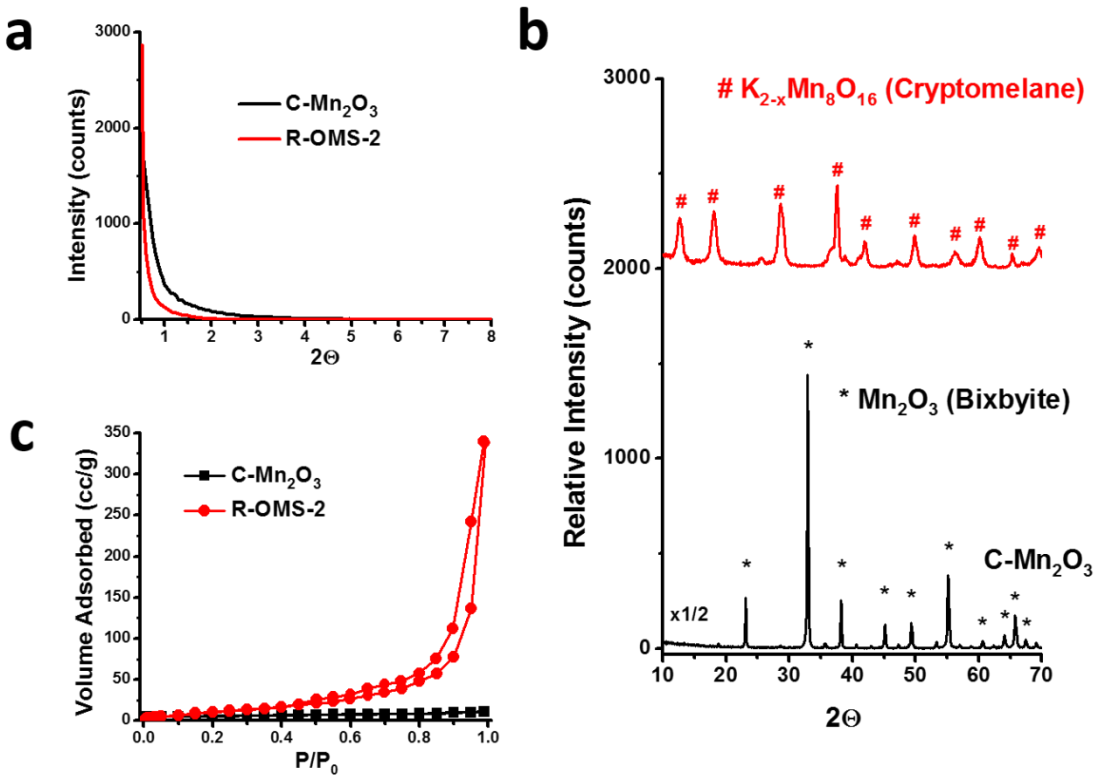

Figure 4.3 (a) Low-angle PXRD, (b) wide-angle PXRD, (c) N_2 sorption isotherms of C-Mn_2O_3 and R-OMS-2 samples.

4.3.2 Electron Microscopy Characterization of Mesoporous Manganese Oxides:

Morphology studies using SEM (**Figure 4.4**) revealed that the acid treatment caused drastic changes on the surface morphology of mesoporous manganese oxides, despite the low magnification images showing aggregated micron sized spheres for all samples. Direct heat treatment of Meso-Mn-A to form Meso-Mn_2O_3 did not cause a significant change ofthe surface morphology. The sample preserved its relatively smooth surface morphology (compare **Figure 4.4a** and **b**). However, the surface morphology of Meso-ε-MnO_2 particles show flakes growing out the particles with wide openings (**Figure 4.4c**) and Meso-OMS-2 sample has surfaces covered by needles growing out of the spherical particles (**Figure 4.4d**). HR-TEM images of mesoporous manganese oxide samples were also collected for better evaluation of the changes of surface morphologies (**Figure 5.5**). HR-TEM images of Meso-Mn-A and Meso-Mn_2O_3 samples show nano-particle aggregates with a porous nature formed by intraparticle voids (mesopores) (**Figure 4.5 a** & **b**). Unlike Meso-Mn_2O_3 samples, the origin of mesoporosity is not clear for Meso-ε-MnO_2 and Meso-OMS-2 samples due to the sample thickness. HR-TEM images of Meso-ε-MnO_2 (**Figure 4.5 c**) and Meso-OMS-2 (**Figure 4.5d**) show flakes and needles growing on the surface of particles which is consistent with the SEM analyses. More detailed HR-TEM analyses using the samples prepared by focus ion beam (FIB) is underway for Meso-ε-MnO_2 and Meso-OMS-2 samples to investigate the origins of mesoporosity.

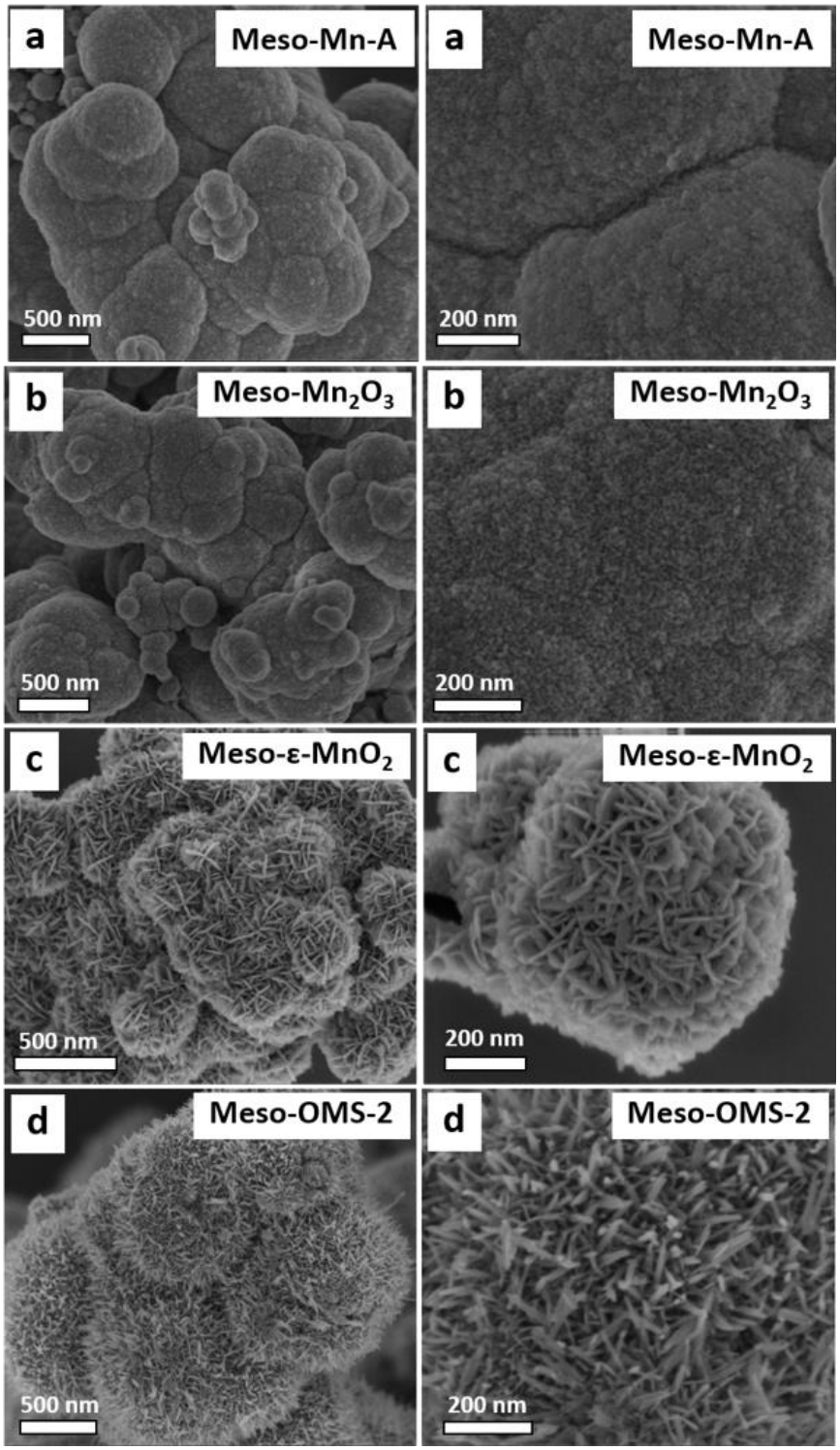

Figure 4.4. SEM images of mesoporous manganese oxides (a) Meso-Mn-A, (b) Meso-Mn_2O_3, (c)Meso-ε-MnO_2, and (d) Meso-OMS-2.

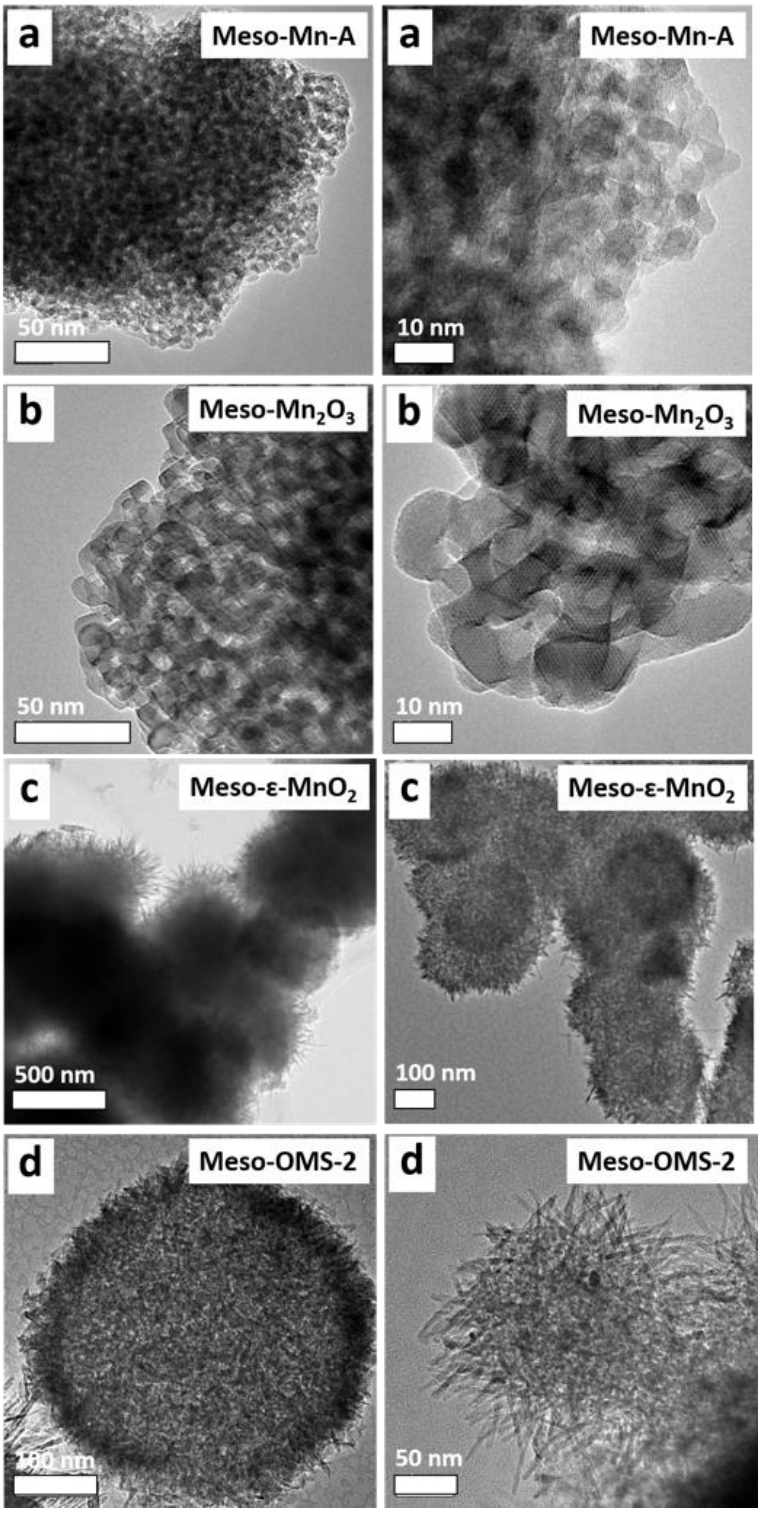

Figure 4.5 HR-TEM images of mesoporous manganese oxides. (a) Meso-Mn-A, (b) Meso-Mn_2O_3, (b) Meso- ε-MnO_2, and (c) Meso-OMS-2.

4.3.3 Redox Properties of Mesoporous Manganese Oxides:

As redox catalysts, manganese oxides are known to be very active for selective or total oxidations or oxidative transformations of various organic compounds in both liquid and gas phase reactions[15,20,33–35,39]. Nano-crystalline manganese oxides with easily interchangeable multiple oxidations states are found to be the most active in these studies. Therefore, the redox properties of mesoporous manganese oxides were examined by H_2-TPR (**Figure 4.6**). Among all the mesoporous samples, Meso-Mn-A showed the lowest reduction temperature of 318°C with a two-step reduction (the second is at 469°C). Meso-Mn_2O_3 was reduced in one step with a peak position of 502°C which was lower than the commercial analogue (C-Mn_2O_3, 534°C). The shift of the reduction temperature was attributed to the more easily reducible nature of nano-crystalline Meso-Mn_2O_3. Meso-OMS-2 showed a two-step reduction (at 347°C and 411°C) and the ratio of the lower temperature peak to the higher temperature peak was around 1. Therefore, the lower temperature reduction was attributed to the reduction of MnO_2 to Mn_2O_3 and the higher temperature peak was attributed to the reduction of Mn_2O_3 to MnO.

On the other hand, R-OMS-2 (non-porous) only showed one broad reduction peak centered at 418°C, which is typical for large and non-porous particles[40]. Meso-ε-MnO_2 also showed a two-step reduction (at 364°C and 480°C) and the ratio of the lower temperature peak to the higher temperature peak was around 2. The lower temperature reduction was attributed the reduction of MnO_2 to Mn_3O_4 and the higher temperature peak was attributed to the reduction of Mn_3O_4 to MnO. Similar reduction profiles were previously observed for γ- and β-MnO_2 which supports our assignments[15]. The reducibility of the samples is enhanced in the order of C-Mn_2O_3 < R-OMS-2 < Meso-Mn_2O_3 < Meso-OMS-2 < Meso-ε-MnO_2 < Meso-Mn-A.

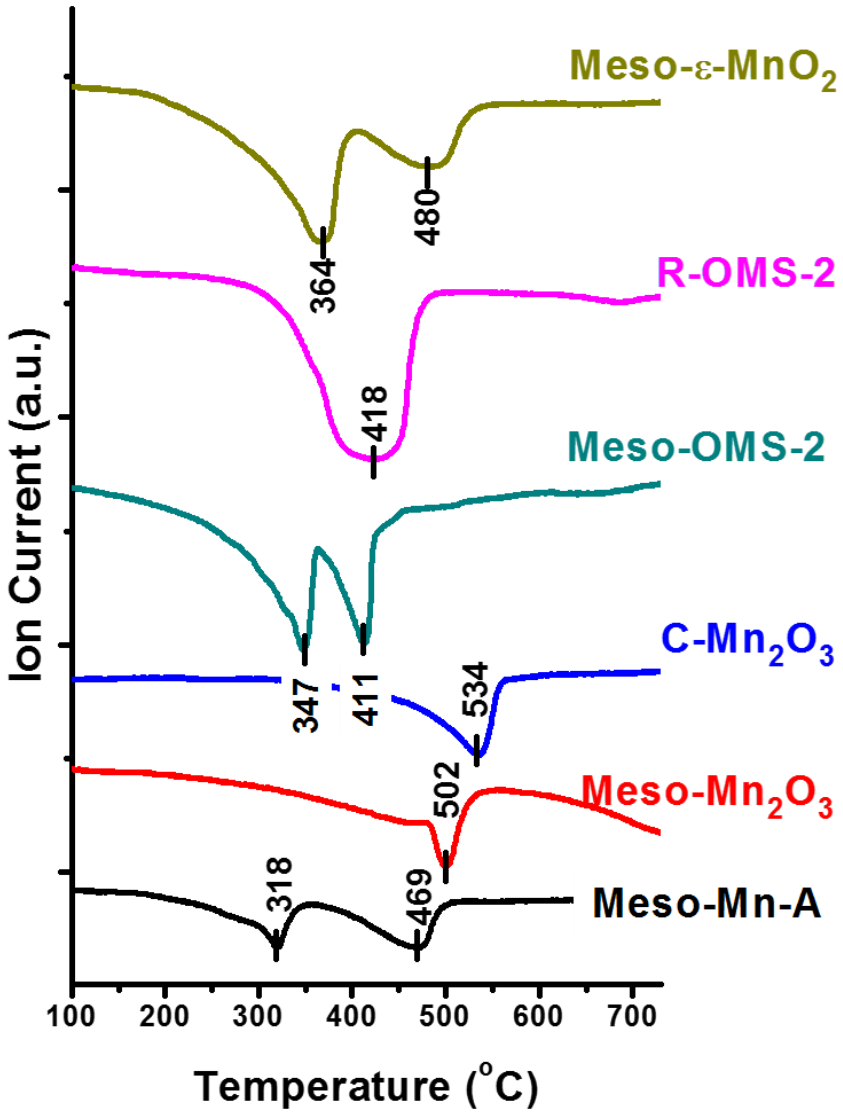

Figure 4.6 H_2-TPR (temperature-programming reduction) profiles of mesoporous manganese oxides (Meso-Mn-A, Meso-Mn_2O_3, Meso-ε-MnO_2, and Meso-OMS-2), C-Mn_2O_3, and R-OMS-2 samples.

4.3.3 Catalytic Properties of Mesoporous Manganese Oxides (CO Oxidation)

The catalytic activity of mesoporous manganese oxides was tested for CO oxidation **Figure 4.7a**. T_{100} (100% conversion) temperatures are summarized in **Table 4.1**. Meso-Mn-A showed the highest activity (100% conversion at RT). Meso-ε-MnO_2 and Meso-OMS-2 demonstrated similar activity and both reached 100% conversions at 50°C. However, Meso-ε-MnO_2 was slightly more active than Meso-OMS-2, which showed 95% (vs. 60%) conversion at RT. Meso-Mn_2O_3 showed the lowest activity among the mesoporous manganese oxides and 100% conversion was observed at 75°C. All mesoporous manganese oxides were much more active than non-porous manganese oxides (R-OMS-2 & C-Mn_2O_3). R-OMS-2 reached 100% conversion at 225°C and C-Mn_2O_3 only reached 20% conversion at the same temperature. The order of catalytic activity was found to be the same as the order of reducibility. The ε-MnO_2 phase (Meso-ε-MnO_2) was found to be the most active phase among the crystalline samples. Therefore, Meso-ε-MnO_2 was also used for the catalytic stability test (**Figure 4.7b**) and no activity loss was observed for CO oxidation after 24 h of reaction.

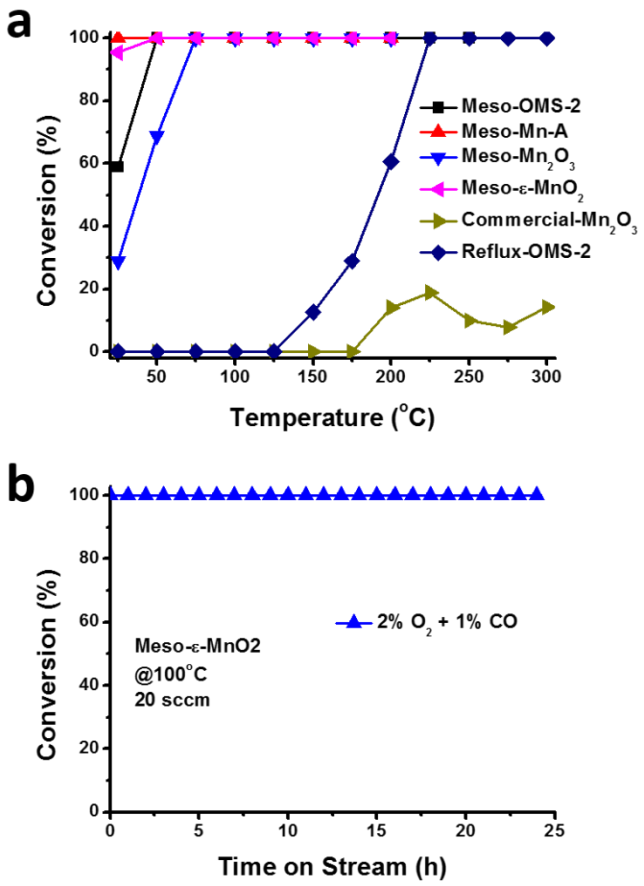

Figure 4.7 The catalytic performance of mesoporous manganese oxides, C-Mn_2O_3, and Reflux-OMS-2 samples at two different O_2 amounts (1% CO). (a) 2% O_2, (b) 1%O_2 (c) Catalytic stability test at different O_2 amounts with Meso- ε-MnO_2 sample.

4.4 Discussions

The parent mesoporous manganese oxides (Meso-Mn-A) are members of the recently discovered University of Connecticut (UCT) mesoporous materials family. The UCT materials are randomly packed monodispersed nano-particle aggregates and the mesopores are continuous intraparticle voids. The UCT materials typically have one low-angle diffraction line indicating the size of the building blocks (nano-particles) and a Type IV adsorption isotherm indicating a regular mesoporous structure[2]. All mesoporous manganese oxides reported in this chapter have these characteristic features. The amorphous manganese oxide (Meso-Mn) was synthesized using a recently developed inverse micelle templating route. Shortly, the method uses inverse non-ionic surfactant micelles (P123) as a soft template while the sol-gel process of manganese sols is controlled in acidic media (HNO_3) by NOx chemistry. NOx is formed *in situ* by thermal decomposition of nitrate ions. The formed NOx is adsorbed on oxo-clusters to prevent uncontrolled condensation and decomposition gradually increases the pH to control the condensation of inorganic sols. All mesoporous samples exhibit high BET surface areas (>128 m^2/g) where Meso-OMS-2 is the one with the highest surface area (277 m^2/g).

The transformation of Mn_2O_3 and Mn_3O_4 phases to MnO_2 in acidic aqueous solutions relies on dissolution-disproportion reactions (**Equation 1-3**)[37,38]. Mn^{3+}(s) is reduced to Mn^{2+} (aq) which leaches out from the oxide surface; meanwhile Mn^{3+}(s) is oxidized to Mn^{4+}(s) to form MnO_2 in acidic aqueous media. Sinha et al. converted mesoporous mixed phase (Mn_3O_4 and Mn_2O_3) manganese oxide to γ-MnO_2 using a 10 M sulfuric acid solution at RT (20x concentrated than the conditions used in this study)[11,39]. In another study, Walanda et al. transformed non-porous Mn_2O_3 to γ-MnO_2 (0.5 M H^+, 80^{o}C for 1 week) and OMS-2 (5.0 M

H^+, 80°C for 1 week) by sulfuric acid treatment[38]. Due to nano-particle nature of UCT materials, the transformation conditions are much milder (0.5 M H^+ at 70°C for 2 h) and resulting materials exhibit high surfaces area and mesoporosity. In addition, mesoporous ε-MnO_2 and OMS-2 have not been observed previously. In order to validate mildness of the reaction conditions, commercial Mn_2O_3 (C-Mn_2O_3) was treated with 0.5 M sulfuric acid solution at 80°C for 4 h. Despite the transformation being done at a higher temperature (70°C vs. 80°C) and longer time (2 h vs. 4 h.), the transformation was incomplete and the major crystal structure was still Mn_2O_3. Most probably, the transformation only occurred on the surface and the bulk remained the same.

Dissolution of Mn_2O_3.

$Mn_2O_3(s) + 2H^+(aq) \leftrightarrow 2MnO^+(aq) + H_2O$ (eq. 1)

Disproportionation.

$2MnO^+(aq) \leftrightarrow MnO_2(s) + Mn^{2+}(aq)$ (eq. 2)

Overall (Equation 1 + Equation 2)

$Mn_2O_3(s) + 2H^+(aq) \leftrightarrow MnO_2(s) + Mn^{2+}(aq) + H_2O$ (eq. 3)

The synthesized mesoporous manganese oxides demonstrated enhanced redox properties compared to nonporous counterparts regardless of the crystal structure investigated. The enhanced redox activity was correlated perfectly with the catalytic activity. The reducibility of the samples so as the catalytic activity for CO oxidation enhanced in the order of C-Mn_2O_3 < R-OMS-2 < Meso-Mn_2O_3 < Meso-OMS-2 < Meso-ε-MnO_2 < Meso-Mn-A.

4.5 Conclusion:

In summary, amorphous mesoporous manganese oxide was transformed into two different crystal phases (OMS-2 and ε-MnO_2) of manganese oxide under mild acidic conditions (0.5 M), at low temperatures (70^oC), and in very short times (2 h). The materials maintained high surface areas (≥ 196 m^2/g) and mesoporosity (4.8-5.6 nm) after the transformation. Nano-crystalline mesoporous manganese oxides demonstrated enhanced reducibility and high catalytic activity for CO oxidation. The catalytic activity correlated with the reducibility and followed the order of C-Mn_2O_3 < R-OMS-2 < Meso-Mn_2O_3 < Meso-OMS-2 < Meso-ε-MnO_2 < Meso-Mn-A. The extension of the work describing the synthesis of various polymorphs (α-, β-, γ-) of MnO_2 and OMS materials is underway.

4.6 References

1. Poyraz, A. S.; Biswas, S.; Genuino, H. C.; Dharmarathna, S.; Kuo, C.-H.; Suib, S. L. *ChemCatChem* **2012**.

2. Poyraz, A. S.; Kuo, C.-H.; Biswas, S.; King'ondu, C. K.; Suib, S. L. *Nat. Commun.* **2013**, *4*.

3. Debecker, D. P.; Hulea, V.; Mutin, P. H. *Appl. Catal. A: Gen.* **2013**, *451*, 192–206.

4. Vos, D. E. D.; Dams, M.; Sels, B. F.; Jacobs, P. A. *Chem. Rev.* **2002**, *102*, 3615–3640.

5. Walcarius, A. *Chem. Soc. Rev.* **2013**, *42*, 4098.

6. Taguchi, A.; Schüth, F. *Microporous Mesoporous Mater.* **2005**, *77*, 1–45.

7. Ren, Y.; Ma, Z.; Bruce, P. G. *Chem. Soc. Rev.* **2012**, *41*, 4909.

8. Bibby, A.; Mercier, L. *Green Chem.* **2003**, *5*, 15–19.

9. Wu, Z.; Zhao, D. *Chem. Commun.* **2011**, *47*, 3332–3338.

10. Brezesinski, T.; Wang, J.; Tolbert, S. H.; Dunn, B. *Nat. Mater.* **2010**, *9*, 146–151.

11. Sinha, A. K.; Suzuki, K.; Takahara, M.; Azuma, H.; Nonaka, T.; Suzuki, N.; Takahashi, N. *J. Phys. Chem. C* **2008**, *112*, 16028–16035.

12. Tian, Z.-R.; Tong, W.; Wang, J.-Y.; Duan, N.-G.; Krishnan, V. V.; Suib, S. L. *Science* **1997**, *276*, 926–930.

13. Jiao, F.; Bruce, P. G. *Angew. Chem.* **2004**, *116*, 6084–6087.

14. Sinha, A. K.; Suzuki, K. *Angew. Chem.* **2005**, *117*, 275–277.

15. Liang, S.; Teng, F.; Bulgan, G.; Zong, R.; Zhu, Y. *J. Phys. Chem. C* **2008**, *112*, 5307–5315.

16. Takeuchi, K. J.; Yau, S. Z.; Menard, M. C.; Marschilok, A. C.; Takeuchi, E. S. *ACS Appl. Mater. & Interfaces* **2012**, *4*, 5547–5554.

17. Iyer, A.; Del-Pilar, J.; King'ondu, C. K.; Kissel, E.; Garces, H. F.; Huang, H.; El-Sawy, A. M.; Dutta, P. K.; Suib, S. L. *J. Phys. Chem. C* **2012**, *116*, 6474–6483.

18. Yang, S.; Sun, Y.; Chen, L.; Hernandez, Y.; Feng, X.; Müllen, K. *Sci. Reports* **2012**, *2*.

19. Zhang, C.; Feng, C.; Zhang, P.; Guo, Z.; Chen, Z.; Li, S.; Liu, H. *RSC Adv.* **2012**, *2*, 1643.

20. Li, J.; Wang, R.; Hao, J. *J. Phys. Chem. C* **2010**, *114*, 10544–10550.

21. Xia, Y.; Dai, H.; Jiang, H.; Zhang, L. *Catal. Commun.* **2010**, *11*, 1171–1175.

22. Jiao, F.; Jumas, J.-C.; Womes, M.; Chadwick, A. V.; Harrison, A.; Bruce, P. G. *J. Am. Chem. Soc.* **2006**, *128*, 12905–12909.

23. Wang, X.; Li, Y. *Chem. - Eur. J.* **2003**, *9*, 300–306.

24. Kim, C.-H.; Akase, Z.; Zhang, L.; Heuer, A. H.; Newman, A. E.; Hughes, P. J. *J. Solid State Chem.* **2006**, *179*, 753–774.

25. Ding, Y.-S.; Shen, X.-F.; Gomez, S.; Luo, H.; Aindow, M.; Suib, S. L. *Adv. Funct. Mater.* **2006**, *16*, 549–555.

26. Liu, Y.; Wang, H.; Zhu, Y.; Wang, X.; Liu, X.; Li, H.; Qian, Y. *Solid State Commun.* **2009**, *149*, 1514–1518.

27. Suib, S. L. *Accounts Chem. Res.* **2008**, *41*, 479–487.

28. Pérez, H.; Navarro, P.; Torres, G.; Sanz, O.; Montes, M. *Catal. Today* **2013**, *212*, 149–156.

29. Du, Y.; Meng, Q.; Wang, J.; Yan, J.; Fan, H.; Liu, Y.; Dai, H. *Microporous Mesoporous Mater.* **2012**, *162*, 199–206.

30. Poyraz, A. S.; Hines, W. A.; Kuo, C.-H.; Li, N.; Perry, D. M.; Suib, S. L. *J. Appl. Phys.* **2014**, *115*, 114309.

31. Ghodbane, O.; Pascal, J.-L.; Favier, F. *ACS Appl. Mater. & Interfaces* **2009**, *1*, 1130–1139.

32. Chen, C.-H.; Suib, S. L. *J. Chin. Chem. Soc.* **2012**, *59*, 465–472.

33. Dharmarathna, S.; King'ondu, C. K.; Pedrick, W.; Pahalagedara, L.; Suib, S. L. *Chem. Mater*. **2012**, *24*, 705–712.

34. Wang, Y.; Kobayashi, H.; Yamaguchi, K.; Mizuno, N. *Chem. Commun.* **2012**, *48*, 2642.

35. Luo, J.; Zhang, Q.; Garcia-Martinez, J.; Suib, S. L. *J. Am. Chem. Soc.* **2008**, *130*, 3198–3207.

36. DeGuzman, R. N.; Shen, Y.; Neth, E. J.; Suib, S. L.; O'Young, C.; Levine, S.; Newsam, J. M. *Chemistry of Materials*, 1994, *6*, 815–821.

37. Artamonova, I. V.; Gorichev, I. G.; Godunov, E. B. *Engineering* **2013**, *05*, 714–719.

38. Walanda, D. K.; Lawrance, G. A.; Donne, S. W. *J. Power Sources* **2005**, *139*, 325–341.

39. Sinha, A. K.; Suzuki, K.; Takahara, M.; Azuma, H.; Nonaka, T.; Fukumoto, K. *Angew. Chem. Int. Ed.* **2007**, *46*, 2891–2894.

40. Luo, J.-Y.; Meng, M.; Li, X.; Li, X.-G.; Zha, Y.-Q.; Hu, T.-D.; Xie, Y.-N.; Zhang, J. *Journal of Catalysis*. 2008, pp. 310–321.

Chapter 5: Future Directions:

The developed inverse micelle templating route and the utilization of NOx chemistry for the first time to controlling the sol-gel rates are unorthodox approaches for synthesizing mesoporous materials. The developed method is not only generic, but also the materials synthesized by the method demonstrate different physicochemical properties and high thermal stabilities. As a future perspective, the developed methods can be (1) further developed and optimized, (2) used to contribute to the making of thin films, coatings, doping, and surface promotion of existing nanostructures, and (3) useful for designing unique materials for catalytic, electronic, magnetic, and optical materials for specific applications.

Current knowledge in the synthesis of amphiphilic substances (surfactants) allows one to synthesize surfactants with almost limitless possibilities. The self-assembly of these surfactants into supramolecular structures (i.e. micelles, vesicles, liquid crystals, 2D layered structures) in numerous solvent systems and external conditions (i.e. temperature, electric field) have been extensively studied. With this knowledge only, new inverse micellar solutions with different solvent systems can be designed to synthesize inverse micelle template mesoporous materials. A change in the solvent system will also alter the reaction conditions such as temperature, duration, and acidity to give more flexibility in using various metal precursors. Combined with the knowledge of NOx chemistry, potential synthesis of new mesoporous materials with tunable physicochemical properties and different crystal structures is possible. For example, a new surfactant and water free inverse micelle system can make the

use of conventional sol-gel chemistry of transition metal sols (hydrolysis and condensation) possible.

Apart from the possibilities of using inverse micelles created by different surfactants, the developed NOx (nitric oxides) regulated sol-gel chemistry brings additional possibilities to long existing conventional methods to synthesize mesoporous materials. Recall that the main limitation in conventional sol-gel chemistry for the synthesis of mesoporous materials is the water content in the reaction media. Since NOx chemistry can easily control the gelation of inorganic sols in the presence of water (water tolerant), one can use aqueous micellar solutions or liquid crystals as soft templates to make mesoporous materials with cylindrical pore structures.

APPENDIX

List of publications, book chapters, patent applications, presentations, and posters

1. **Journal Articles:**

- Wenqiao Song, **Altug S. Poyraz** , Yongtao Meng, Zheng Ren, Sheng-Yu Chen, and Steven L. Suib "Crystalline Mesoporous $K_{2-x}Mn_8O_{16}$ (K-OMS-2) and ε-MnO_2 by Mild Transformations of Amorphous Mesoporous Manganese Oxide and Their Enhanced Redox Properties" **Chemistry of Materials** 2014, *26* (15), 4629–4639.
- **Altug S. Poyraz**, Wenqiao Song, David Kriz, Chung-Hao Kuo, Mohammad S. Seraji, and Steven L. Suib "Crystalline Mesoporous $K_{2-x}Mn_8O_{16}$ (K-OMS-2) and ε-MnO_2 by Mild Transformations of Amorphous Mesoporous Manganese Oxide and Their Enhanced Redox Properties" **ACS Appl. Mater. Interfaces** 2014, 6 (14), 10986–10991.
- Chung-Hao Kuo, Weikun Li, Wenqiao Song, Zhu Luo, **Altug S. Poyraz**, Yang Guo, Steven Suib, Jie He "Facile synthesis of Co_3O_4@CNT with high catalytic activity for CO oxidation under moisture-rich conditions" **ACS Appl. Mater. Interfaces** 2014, 6 (14), pp 11311–11317.
- **Altug S. Poyraz**, Chung-Hao Kuo, Eugene Kim, Yongtao Meng, Saiful Islam, and Steven L. Suib "*Tungsten Promoted Mesoporous Group 4 (Ti, Zr, & Hf) Transition Metal Oxides for Room Temperature, Solvent Free Acetalization and Ketalization Reactions*" **Chemistry of Materials** 2014, 26 (9), 2803–2813.
- **Altug S. Poyraz**, William A. Hines, Chung-Hao Kuo, Nan Li, David M. Perry, and Steven L. Suib "*Mesoporous Co_3O_4 Nanostructured Material Synthesized by One-*

Step Soft-Templating: A Magnetic Study" **Journal of Applied Physics** 2014, 115, 114309.

- Chung-Hao Kuo, **Altug S. Poyraz**, Lei Jin, Yongtao Meng, Sheng-Yu Chen, and Steven L. Suib *"Heterogeneous Acidic TiO_2 Nanoparticles for Efficient Conversion of Biomass Derived Carbohydrates"* **Green Chemistry** 2014, 16,785-791.
- **Altug S. Poyraz**, Chung-hao Kuo, Sourav Biswas, Cecil K. King'ondu and Steven L. Suib "*A general approach to crystalline and monomodal pore size mesoporous materials*" **Nature Communications** 2013, 4, 2952, doi:10.1038/ncomms3952.
- Mahmut Özacar, **Altug S. Poyraz**, Homer C. Genuino, Chung-hao Kuo, Yongtao Meng and Steven L. Suib "*Influence of Silver on the Catalytic Properties of the Cryptomelane and Ag-Hollandite Types Manganese Oxides OMS-2 in the Low-Temperature CO Oxidation*" **Applied Catalysis A: General** 2013, 462-463, 64-74.
- **Altug S. Poyraz**, Sourav Biswas, Homer C. Genuino, Saminda Dharmarathna, Chung-hao Kuo, and Steven L. Suib *"Bimodification of Mesoporous Silicon Oxide by Coupled "In Situ Oxidation at the Interface and Ion Exchange"* and its Catalytic Activity in the Gas-Phase Toluene Oxidation" **Chemcatchem** 2013, 5, 920-930.
- **Altug S. Poyraz**, Omer Dag "*Role of organic and inorganic additives on the assembly of CTAB-P123 and the morphology of mesoporous silica particles"***Journal of Physical Chemistry C** 2009, 113, 18596-18607.
- **Altug S. Poyraz**, Cemal Albayrak, Omer Dag "*The effect of cationic surfactant and some organic/inorganic additives on the morphology of mesostructured silica templated by pluronics"* **Microporous and Mesoporous Materials** 2008, 115, 548–555.

2. Book Chapters

- **Altug S. Poyraz,** Yongtao Meng, Sourav Biswas, Eugene Kim, Steven L. Suib "*Mesoporous Multivalent Transition Metal Oxides (V, Cr, Mn, Fe, and Co) in Catalysis*" In **Comprehensive Guide for Mesoporous Materials,** Nova Science Publishers, Inc. *In Press.*
- **Altug S. Poyraz,** Yongtao Meng, Sourav Biswas, and Steven L. Suib Mesoporous TM Oxide Materials by Surfactant Assisted Soft Templating" In **Perovskite and mixed oxides,** Viley-VCH. *In Press.*

3. Patent Applications

- **Altug S. Poyraz**, Steven L. Suib " *Mesoporous Metal Oxides and Processes for Preperation Thereof* " US Provisional Application No: 61/705,372.
- **Altug S. Poyraz**, Steven L. Suib " *Mesoporous Metal Oxides and Processes for Preperation Thereof* " International Application No: PCT/US2013/061736. Publication no: WO 2014/052480 A1 & WO 2014/052482 A1.

4. PRESENTATIONS & MEETINGS

- **Altug S. Poyraz** and Steven L. Suib "Crystalline, monomodal pore size mesoporous manganese oxide materials for CO oxidation" (Oral-Talk) **247th ACS National**

Meeting & Exposition - March 16-20, 2014, Dallas, TX "Chemistry&Materials for Energy"

- **Altug S. Poyraz** and Steven L. Suib "Tungsten promoted mesoporous transition metal (Ti, Zr, & Hf) oxides for low temperature, solvent free acetalization and ketalization reactions" (poster presentation) **247th ACS National Meeting & Exposition -** March 16-20, 2014, Dallas, TX "Chemistry&Materials for Energy"